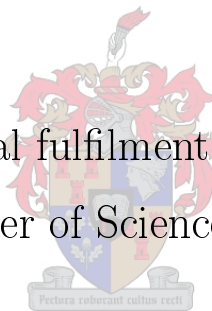


The prediction of flow through two-dimensional porous media

Luther Terblanche

Thesis presented in partial fulfilment of the requirements for the
degree of Master of Science in Engineering.



Promoter: Dr GPJ Diedericks

Co-Promoter: Dr GJF Smit

April 2006

Declaration

I, the undersigned, hereby declare that the work contained in this thesis is my own original work and I have not previously in its entirety or in part submitted it at any university for a degree.

Signature: _____

Date: _____

Abstract

When considering flow through porous media, different flow regimes may be identified. At very small Reynolds numbers the relation between the pressure gradient and the velocity of the fluid is linear. This flow regime is known as the Darcy flow regime. The proportionality coefficient of this linear relationship is termed the Darcy permeability. Many successful semi-empirical models have been developed over the past few decades to predict the Darcy permeability. For intermediate Reynolds numbers it is experimentally accepted that the relation between the pressure gradient and velocity is non-linear. This flow regime is known as the Forchheimer flow regime. Derivations of analytic expressions for this non-linear relation are still an important field of research.

In this work, attention is focussed on the onset of the inertial flow phenomena in the so-called Forchheimer regime. Numerical simulation results, obtained with the commercial CFD package, FLUENT, for laminar Newtonian flow through prismatic bundles, confirm the different flow regimes. The existence of a third laminar flow regime for fluid flow through porous media, which serves as a transition between the Darcy and Forchheimer flow regimes, is observed numerically. This corresponds with numerical results obtained for different types of media presented in literature.

Macroscopic balance equations are derived through the volume averaging theory. The closure modelling is conducted by employing a pore-scale model based on a Rectangular Representative Unit Cell (RRUC). Models based on the RRUC, for both the Darcy and Forchheimer flow regimes, are discussed. The results obtained from the numerical simulations are used to verify the assumptions used in the RRUC modelling procedure. Areas where the assumptions can be improved are suggested. An alternative modelling attempt, also based on the RRUC, for the Forchheimer flow regime is proposed.

Opsomming

Tydens vloeï deur poreuse media is dit moontlik om verskillende vloeigebiede te identifiseer. By baie klein Reynoldsgetalle is die verhouding tussen die drukgradiënt en die snelheid van die vloeistof lineêr. Hierdie vloeigebied staan bekend as die Darcy vloeigebied. Die eweredigheidskoeffisiënt in hierdie lineêre verhouding word die Darcy permeabiliteit genoem. Verskeie semi-empiriese modelle is ontwikkel oor die laaste paar dekades om die Darcy deurlaatbaarheid suksesvol te voorspel. Vir intermediêre Reynoldsgetalle word dit eksperimenteel aanvaar dat die verhouding tussen die drukgradiënt en snelheid nie-lineêr is. Hierdie heet die Forchheimer vloeigebied. Afleidings van analitiese uitdrukkings vir hierdie nie-lineêre verhouding is en bly steeds 'n belangrike navorsingsveld.

In hierdie tesis word aandag geskenk aan die aanvang van die gebied waar inersia die vloeï domineer. Numeriese simulasiereultate, wat verkry is deur die kommersiële CFD pakket, FLUENT, vir laminêre Newtoniese vloeï deur prismaatiese bundels, bevestig die verskillende vloeigebiede. Die bestaan van 'n derde laminêre vloeigebied vir vloeïstofvloeï deur poreuse media, wat dien as 'n oorgang tussen die Darcy en Forchheimer vloeigebiede, word numeries waargeneem. Bogenoemde stem ooreen met numeriese resultate wat verkry is vir verskillende tipes poreuse media in die literatuur.

Makroskopiese balansvergelykings word afgelei deur gebruik te maak van die volumetriese homogeniseringsteorie. Die sluitingsmodellering word uitgevoer deur gebruik te maak van 'n mikroskopiese model wat gebaseer is op 'n reghoekige verteenwoordigende eenheidsel (*Rectangular Representative Unit Cell* - RRUC). Modelle gebaseer op die RRUC, vir beide die Darcy en Forchheimer vloeigebiede, word bespreek. Die resultate wat verkry is vanaf die numeriese simulaties word gebruik om die aannames wat gebruik is in die RRUC modelleringsprosedure te bevestig. Voorstelle word gemaak in gebiede waar die aannames verbeter kan word. 'n Alternatiewe modelleringspoging, ook gebaseer op die RRUC, vir die Forchheimer vloeigebied word ook voorgestel.

Acknowledgements

I wish to express my gratitude to all the people who supported me in some way or another in the development of this thesis.

I would like to thank my family for all their encouragement and for giving me the opportunity to pursue my tertiary studies. I would also like to thank my special friend, Leana Oberholzer, for all her moral support.

Special thanks to my supervisor, Dr GPJ Diedericks, for his motivation, guidance, friendly attitude and availability to discuss topics related to the thesis. I would also like to thank my co-supervisor, Dr GJF Smit, for all his assistance in the technical details of the numerical simulations. Working with Dr Diedericks and Dr Smit was truly an inspirational experience.

Finally, I would like to thank the Harry Crossley Fund for providing financial assistance without which this thesis would not have been possible.

Contents

1	Introduction	1
1.1	Preface	1
1.2	Porous media modelling philosophy	2
1.3	Porous media flow regimes	2
1.4	Outline	5
1.5	Objectives	6
2	The porous medium	7
2.1	Definition of a porous medium	7
2.2	Classification of porous media	8
2.2.1	Connectivity	8
2.2.2	Homogeneity and heterogeneity	9
2.2.3	Isotropy and anisotropy	10
2.2.4	Porous environments	10
2.3	Porous media modelling parameters	11
2.3.1	Porosity	11
2.3.2	Permeability	12
2.3.3	Specific surface areas	13

2.3.4	Staggeredness	13
3	Volume averaging	15
3.1	The representative elementary volume (REV)	15
3.2	Phase averages and deviation	17
3.3	Averaging identities	17
3.4	Slattery's averaging theorem	18
3.5	Identities based on the averaging theorem	19
3.6	Averaging of time derivatives	20
3.7	Interstitial transport variables	21
3.7.1	Flow directions	21
3.7.2	Geometric variables	22
3.7.3	Velocity and pressure variables	23
3.7.4	Velocity relationships	25
3.8	Conservation of mass	28
3.9	Momentum transport	29
4	The Rectangular Representative Unit Cell	32
4.1	Properties of the RRUC	32
4.2	Construction of an RRUC	33
4.3	Two-dimensional RRUC geometry modelling	34
4.3.1	Definition of volumes	34
4.3.2	Non-staggered RRUC configuration	35
4.3.3	Staggered RRUC configuration	35
4.3.4	Tortuosity	37

4.4	Interstitial pressure modelling	40
4.4.1	Non-staggered configuration	40
4.4.2	Staggered configuration	44
4.5	Interstitial flow modelling	48
4.5.1	The Reynolds number	49
4.5.2	The Darcy regime	50
4.5.3	The Forchheimer regime	52
4.5.4	General momentum transport	56
5	Numerical investigations	59
5.1	Numerical procedures	59
5.1.1	Geometrical setup	59
5.1.2	Boundary conditions and solution method	60
5.2	Microscopic flow patterns	61
5.3	Energy dissipation	63
5.4	Flow regimes	71
5.5	The momentum equation and drag	75
6	Verification of modelling assumptions	80
6.1	Negligible skin drag	80
6.2	Distributions of wall pressures	81
6.2.1	Pressures on the upstream face	81
6.2.2	Pressures on the downstream face	83
6.2.3	Pressures on the downstream face and the inflection point pressure	84
6.3	The use of the Bernoulli equation	87

6.4	The inflection point velocity as a ratio of the interstitial stream-wise velocity	88
6.5	Asymptote matching	89
6.6	A modelling recommendation	92
7	Conclusions	98
A	Derivation of the averaging identities	100
B	Slattery's averaging theorem	104
C	Derivation of the averaging theorem identities	108

List of Figures

2.1	Samples of porous media which illustrate the different types of connectivity.	9
2.2	A two-dimensional schematic representation of the staggeredness of a porous medium.	14
3.1	A two-dimensional representation of a Representative Elementary Volume taken from a sample of a porous medium.	16
3.2	A two-dimensional representation of an REV with the different unit vectors for velocity directions.	22
3.3	A schematic representation of the different velocity relationships (Taken from Diedericks (1992)).	27
4.1	A Rectangular Representative Unit Cell for prismatic bundles.	34
4.2	Non-staggered configuration of an RRUC.	36
4.3	A staggered configuration of an RRUC.	37
4.4	Piecewise straight streamlines represented in a two-dimensional RRUC for the staggered and non-staggered cases.	38
4.5	Tortuosity of staggered and non-staggered configurations.	39
4.6	Pressure distributions in non-staggered RRUC geometry where the RRUC boundary cuts the solid constituent (The squareness of the RRUC is suppressed for clarity).	41

4.7	Pressure distributions in non-staggered RRUC geometry where the RRUC boundary cuts the fluid phase. (The squareness of the RRUC is suppressed for clarity.)	43
4.8	Pressure distributions in the staggered RRUC geometry where the RRUC boundary cuts the solid constituent.	45
4.9	Pressure distributions in the staggered RRUC geometry where the RRUC boundary cuts only the fluid phase.	47
4.10	A two-dimensional schematic representation of interstitial flow recirculation in an upper half of an RRUC.	53
5.1	The geometrical model for the staggered configuration of porosity, $\epsilon = 0.75$	60
5.2	A few streamlines at different Reynolds numbers in a staggered square array of porosity 0.6636.	62
5.3	The viscous dissipation function ϕ in the fluid domain of a staggered RRUC of porosity 0.6636 in the Darcy regime and the Forchheimer regime in units of W/m^2	69
5.3	(Continued) The viscous dissipation function ϕ in the fluid domain of a staggered RRUC of porosity 0.6636 in the Darcy regime and the Forchheimer regime in units of W/m^2	70
5.4	The verification of the energy conservation principle on a staggered RRUC.	71
5.5	Graphs of Reynolds number versus the defined friction factor times the Reynolds number for a staggered configuration with porosity 0.4224.	73
5.6	Graph of the transition zone with the Reynolds number versus the defined friction factor times the Reynolds number for a staggered configuration with porosity 0.4224.	74
5.7	Friction factor times the Reynolds number versus the Reynolds number for different porosities.	76
5.8	The contribution of the pressure and viscous dimensionless drags to the total dimensionless macroscopic drag for a two-dimensional prismatic bundle with a porosity of 0.6636.	78

6.1	The percentage of the ratio of the dimensionless friction drag to the dimensionless pressure drag plotted against the Reynolds number for a porosity of 0.6636.	81
6.2	A two-dimensional schematic representation of interstitial flow recirculation in the upper half of an RRUC.	82
6.3	The variation of the wall pressure on the upstream face, face a , of the solid obstruction in a staggered configuration with a porosity of 0.6636 at Reynolds number $Re_p = 180$	83
6.4	The variation of the wall pressure on the upstream face, face b , of the solid obstruction in a staggered configuration with a porosity of 0.6636 at Reynolds number $Re_p = 180$	84
6.5	Some of the properties of the inflection point of the dividing streamline on a staggered configuration with a porosity of 0.6636.	86
6.6	The percentage relative error between the computed pressure at the inflection point and the numerical value of the pressure at the inflection point on a staggered configuration with a porosity of 0.6636.	88
6.7	The numerically computed β coefficients for different Reynolds numbers and the velocity vectors near the inflection point for a staggered configuration with a porosity of 0.6636.	90
6.8	A graph of the numerical data and the curve obtained through asymptote matching with a shifting parameter of $s = 1$ for a porosity of 0.6636.	91
6.9	A schematic diagram of the locations of the pressures used for the modelling of intermediate Reynolds number flow in a staggered configuration.	93
6.10	A comparison between the proposed model and the models discussed in section 4.5.	96
B.1	Uniform translation of an REV along an arbitrary curve s	106

Nomenclature

Standard characters

c_d	[]	Drag coefficient
d	[m]	Linear RRUC dimension
d_p	[m]	RRUC pore width
d_s	[m]	RRUC solid constituent width
g	[m/s^2]	Gravitational acceleration
G	[]	Interstitial resistance factor
G_0	[]	Interstitial viscous resistance factor
G_∞	[]	Interstitial inertial resistance factor
k	[m^2]	Hydrodynamic permeability
K	[]	Dimensionless hydrodynamic permeability
L	[m]	Predefined straight line length
L_e	[m]	Length of tortuous flow path
$\underline{\underline{\mathcal{L}}}$	[]	Geometric lineality tensor
\mathcal{L}	[]	Stream-wise component of $\underline{\underline{\mathcal{L}}}$ for RRUC
\underline{n}	[]	Outwardly directed unit vector on fluid boundary
\hat{n}	[]	Stream-wise unit vector

\tilde{n}	[]	Unit vector tangent to streamline
p	[Pa]	Pressure
P	[Pa]	Pressure including gravitational pressure head
P_f	[Pa]	Interstitial phase average pressure, $\langle P \rangle_f$
q	[m/s]	Stream-wise superficial velocity
Q	[m ³ /s]	Volumetric flow rate
Re_p	[]	Interstitial Reynolds number
s	[]	Fitting parameter
S	[m ²]	RRUC Surface
\mathcal{S}	[m ²]	REV Surface
t	[s]	Time
u	[m/s]	Drift speed in the stream-wise direction
U	[m ³]	RRUC volume
\mathcal{U}	[m ³]	REV volume
v	[m/s]	Interstitial speed
w	[m/s]	Average speed in stream-wise pores

Greek symbols

α	[]	Generic constant
β	[]	Transverse to streamwise proportionality coefficient
ϵ	[]	Porosity
λ	[]	Friction factor
μ	[N · s/m ²]	Dynamic fluid viscosity

ρ	$[kg/m^3]$	Fluid density
$\underline{\underline{\sigma}}$	$[N/m^2]$	Stress tensor
σ	$[N/m^2]$	Scalar stress component
$\underline{\underline{\tau}}$	$[N/m^2]$	Viscous stress tensor
τ	$[N/m^2]$	Local shear stress
τ_w	$[N/m^2]$	Wall shear stress
Φ	$[W/m^2]$	Viscous dissipation function
$\underline{\underline{\chi}}$	$[\]$	Geometric tortuosity tensor
χ	$[\]$	Tortuosity component for RRUC
ψ	$[\]$	Generic variable

Special symbols

Δ	Change in stream-wise volume difference operator
δ	Change in transverse volume difference operator
∇	Gradient operator (Del)
$\langle \rangle$	Phase average operator
$\langle \rangle_f$	Intrinsic phase average operator
$\{ \}$	Deviation operator
$\underline{\quad}$	Vector (underlined)
$\underline{\underline{\quad}}$	Diadic (double underlined)

Subscripts

\parallel	Parallel to stream-wise direction
\perp	Perpendicular to stream-wise direction
f	Fluid phase
s	Solid phase
ff	Fluid-fluid interface
fs	Fluid-solid interface
g	Stagnant
t	Transfer
0	Total of solid and fluid phases

Chapter 1

Introduction

1.1 Preface

The subject of transport in porous media includes a large number of scientific disciplines. Independent of a particular application, progress in these disciplines includes theoretical modelling, specific applicatory models, numerical analysis and the requirement of improved experimental results. This study attends to the fields of numerical analysis and theoretical modelling on the specific applicatory model of intermediate Reynolds number flow through two-dimensional porous structures.

Practical applications of transport through two-dimensional porous media include timber drying kilns, heat exchangers, the study of air flow through cities as well as wind breaks. Realistic flow conditions in these practical examples include high flow rates, and it is therefore important to understand and model the physical properties of intermediate Reynolds number flow through porous media.

In the engineering industry semi-empirical models are used more frequently than conceptual models. The main disadvantage of semi-empirical models is the need for a large number of experimental measurements. Successful predictive models will aid a better physical understanding of the basic physical principles and idealistically lead to a single unified theory of transport in porous media. Although a considerable amount of attention has been paid to the development of conceptual models over the years, there is still ample room for improvement.

1.2 Porous media modelling philosophy

Due to the complexity of the intra-pore structures, it is labour intensive to solve the microscopic flow field inside the pores as a fluid traverses the porous medium. Also, most engineering applications are only concerned with the average behaviour of the fluid properties. Therefore, models have been developed to derive equations that describe the average behaviour of the flow process in terms of measurable parameters.

The Navier-Stokes and continuity equations that describe the flow phenomenon in the pore sections of the porous medium are averaged with the use of a volume averaging procedure to obtain equations that describe the transport behaviour of the fluid at a macroscopic level. The resulting equations contain some terms that are not macroscopically measurable and, therefore, these equations are referred to as open equations. The process whereby these additional variables are constitutively modelled is referred to as the closure of the macroscopic equations.

One technique of closing the macroscopic equations is by the introduction of a unit cell. In this study, focus will be placed on the Rectangular Representative Unit Cell (RRUC) introduced by Du Plessis and Masliyah (1988). In their approach the unit cell contains, on average, all the geometric information about the micro-structure in a simple enough arrangement to compute the flow properties inside the unit cell. This allows for the averaging of the microscopic quantities over the RRUC and aid the solution of surface integrals to obtain closure of the macroscopic equations.

1.3 Porous media flow regimes

When considering laminar flow through porous media, three main flow regimes may be distinguished: The Darcy flow regime, with very low flow rates and where viscous shear effects dominate; the Forchheimer flow regime, with high flow rates and where inertial effects dominate; the transitional flow regime, which acts as an transitional zone between the Darcy and Forchheimer regimes (Firdaouss et al., 1997).

One of the most profound relationships to flow through porous media is the relationship between the pressure gradient and the superficial or discharge velocity developed by Henry Darcy about 150 years ago (Tokaty, 1971). The empirical Darcy law relates the superficial

velocity in a linear relationship with the pressure gradient as follows in one dimension:

$$-\frac{dP}{dx} = \frac{\mu}{k}q \quad (1.1)$$

where q is the superficial velocity, μ is the viscosity of the fluid and P is the pressure. The coefficient of proportionality, k , is referred to as the permeability. This permeability coefficient is generally determined experimentally, but much effort have been expended on attempting to obtain analytical expressions for the permeability coefficient (Bear, 1972). A rather successful expression for the permeability in terms of measurable parameters has been presented by Du Plessis (1991) with the use of the RRUC model and corrections to this expression were presented by Lloyd et al. (2004).

A limitation to Darcy's law is the fact that it is only valid over a limited range of Reynolds numbers. It has been found experimentally that the linear relationship of Darcy's law breaks down for flow above a certain Reynolds number (Bird et al., 1960; Teng et al., 2000). Consequently, a number of efforts have been made to furnish a universal expression relating the pressure gradient to the specific discharge by adding additional empirical terms to Darcy's law. For example, in 1901 Forchheimer added an additional empirical term (Forchheimer, 1901), which is proportional to the square of the Darcy or superficial velocity, to Darcy's law and proposed

$$-\frac{dP}{dx} = \frac{\mu}{k}q + \beta\rho q^2 \quad (1.2)$$

in one dimension, where β is an inertial parameter and ρ is the density of the fluid. A more general form,

$$-\frac{dP}{dx} = Mq + Nq^2 \quad (1.3)$$

is frequently used by authors such as Hassanizadeh and Gray (1987), where the coefficients M and N is said to be empirical constants and dependent on the structural parameters of the porous medium and fluid viscosity. It is also generally excepted that at low values of the superficial velocity, the square term in the Forchheimer equation (1.3) becomes negligible and the equation reduces to Darcy's law (1.1). Conversely, for higher superficial velocities the linear term in the Forchheimer equation is negligibly small in comparison with the

square term, and discarding it a square law is obtained for the pressure gradient.

It has recently been shown that there exist a transition zone between the Darcy flow regime and the laminar Forchheimer flow regime. The inertia correction to Darcy's law for Reynolds numbers near unity is believed to be a cubic relation between the superficial velocity and the pressure gradient

$$-\frac{dP}{dx} = \frac{\mu}{k}q + \frac{\gamma\rho^2}{\mu}q^3 \quad (1.4)$$

with γ an inertial coefficient. This law was first shown numerically (Barrère, 1990) and then derived theoretically for homogeneous isotropic porous media by using double scale homogenisation (Mei and Auriault, 1991; Wodie and Levi, 1991). This law is also accepted by other authors including Skjetne (1999b), Rojas et al. (1998) and Fourar et al. (2004). Fourar et al. (2004) shed some light on the controversy of this flow regime by showing numerically that the transition regime is considerably smaller for three-dimensional porous media than for two-dimensional porous media. This effect makes the transition regime difficult to be detected by experimental procedures.

There are various opinions as to the exact reasons for momentum dissipation at the onset of the non-Darcy flow regimes. One reason for the non-linear relationship is believed to be the onset of turbulence within the flow channels (Bird et al., 1960). However, experimental evidence indicates that the non-linear dependence appears before the onset of turbulence (Seguin et al., 1998a, 1998b). Authors, including Hassanizadeh and Gray (1987), derived the Forchheimer equation by attributing the origin of the non-linearity to increased macroscopic drag on the pore walls. Barak (1987) corresponded to this comment by suggesting that as the Reynolds number changes, microscopic inertial forces contribute to the change in the microscopic streamline shape. This argument is also supported by Ma and Ruth (1993) and a detailed physical investigation was presented by these authors. Skjetne et. al. (1999c) proposed that the Forchheimer equation is due to the combination of several effects, including microscopic inertial forces and the development of strong localised dissipation zones around flow separation. Fourar et al. (2004) showed that the momentum loss is entirely due to localised viscous dissipation zones.

1.4 Outline

In Chapter 2 different characteristics of porous media are discussed in general. The concept of a porous medium is defined and different categories in which it may be clarified are discussed. Also, parameters are introduced which may be used to classify different porous environments.

Chapter 3 introduces the volume averaging theory. A clear definition of a Representative Elementary Volume (REV) is presented. Procedures for averaging a variable with the help of an REV is explained and some averaging theorems and identities are discussed. The application of the volume averaging theory is also discussed. Here the balance equations that describe the flow at a microscopic level are averaged. Microscopic and macroscopic transport variables are discussed and relationships between the different macroscopic and microscopic variables are presented.

In Chapter 4 the concept of a Rectangular Representative Unit Cell (RRUC) is introduced. Information about the terms of use as well as the construction of an RRUC are presented. This chapter also presents the reader with a closure modelling procedure, based on the RRUC theory, for the open macroscopic balance equations obtained from the averaging theory.

In Chapter 5 flow inside a two-dimensional RRUC is simulated with the use of the commercial computational fluid dynamics (CFD) code, FLUENT. The main objective of the simulation is to observe the changes in the flow characteristics as the Reynolds number increases. The relationship between the pressure gradient and the superficial velocity is presented graphically for different Reynolds numbers as well as the drag forces on the solid phase in the porous medium. Attention is also focused on the change in shape of the streamlines inside the unit cell with an increase in Reynolds numbers.

Chapter 6 focuses on the verification of the assumptions made in the modelling procedures of Chapter 4. The simulation results obtained from Chapter 5 are used to perform accurate calculations and then to compare these calculations with the expressions obtained from the RRUC modelling, in order to evaluate the accuracy of the modelling assumptions. It is also discussed whether the Forchheimer-type equation is valid in both the Darcy and the Forchheimer flow regimes. A new modelling attempt for the prediction of the pressure drop in die laminar Forchheimer regime is also presented.

1.5 Objectives

The main objective of this study is to verify the assumptions, used in the RRUC modelling approach, at intermediate Reynolds numbers. This objective includes both a theoretical literature study component as well as a numerical component.

The literature components include the following:

- To pursue a literature study of the volume averaging theory and derive macroscopic balance equations.
- Understanding the concept of closure with specific interest in the RRUC closure model.

The numerical component of the study includes:

- Investigating the onset of the different flow regimes numerically in a prismatic bundle.
- Investigating the changes in the microscopic flow field numerically for a prismatic bundle.
- Compare the numerical results to those in literature for other types of porous media.

These results are then used to:

- Verify the assumptions in the RRUC model directly by comparison to the interstitial flow obtained numerically.
- To suggest improvements to the RRUC modelling approach.

It is expected that the numerical results will not only aid the RRUC modelling but will also be applicable to a wider audience, as it enhances the understanding of intermediate Reynolds number flow.

Chapter 2

The porous medium

Transport phenomena in porous media are encountered in many different engineering disciplines. Civil engineering deals, for example, with the movement of moisture through and under engineering structures, as well as the propagation of stresses under foundations of structures. The movement of water and solutes in soil find many applications in agricultural engineering. The chemical engineer is typically interested in heat and mass transport in packed-bed reactor columns, as well as drying processes. The reservoir engineer deals with flow of oil, water and gas in petroleum reservoirs. Therefore, to solve problems concerning transport in porous media, a solid understanding of the structure, characteristics and equations governing various transport processes in porous media is necessary.

2.1 Definition of a porous medium

It would be adequate to firstly give a few examples of porous materials before providing a formal definition. A few examples of natural porous media include soil, sand, rock, forests, lungs and kidneys. Ceramics, metallic foams, bread, drying kilns and sweaters are all examples of artificial porous materials.

Dullien (1979) states that a material needs to pass at least one of the following criteria to be classified as a porous material:

1. It must contain pores or voids, free of solids. These voids must be embedded in the solid or solid matrix. The pores usually contain some fluid, or a mixture of immiscible

fluids.

2. Fluids should be able to penetrate through one face of any sample of the medium and emerge on the other side, i.e., the medium should be permeable to fluids.

Bear and Bachmat (1991) describe a porous medium as a set of solid phases and void spaces which are regularly or irregularly distributed. A phase may be considered as a chemically homogeneous portion of a system which is separated from other such portions by a definite physical boundary. There can only be one gaseous phase in a system, since gaseous phases are miscible and thus do not maintain a distinct boundary between them. On the other hand, we may have more than one fluid phase present in a system. Such liquid phases are referred to as immiscible fluids. This study however, deals with systems where only one liquid phase is present in the porous medium.

Bear and Bachmat (1991) further state that the solid phase (and the void space) should be distributed throughout the medium. Thus, if a sufficiently large sample is taken at different locations of the porous medium, solid phases and void spaces should be present within the sample. At the same time the sample should be small enough as to represent a sufficiently close neighbourhood around the point of sampling. Such a sample will be discussed in more detail in Chapter 3.

2.2 Classification of porous media

A large number of substances may be classified as porous media. It is thus desirable to arrange porous media into several classes to distinguish between different groups one might encounter. Different systems of classification are discussed in the next few paragraphs as well as parameters that may be used to describe porous media.

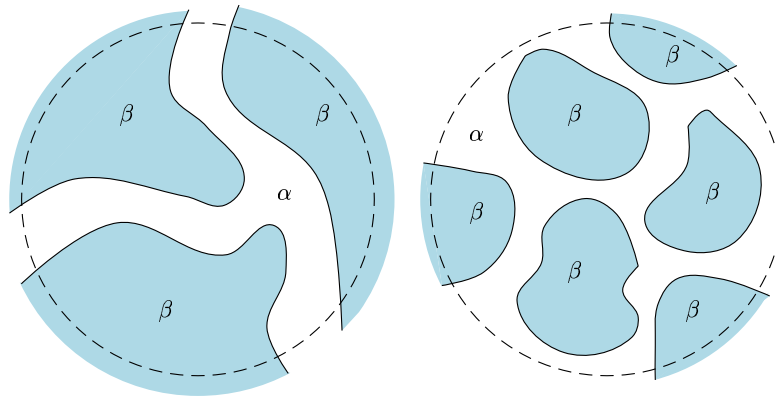
2.2.1 Connectivity

According to Bear and Bachmat (1991) a domain is connected, or interconnected, if any two points contained within the domain can be connected by a curve that lies completely within the domain. The α -domain in Figure 2.1 is connected.

A connected domain can be either simply- or multiply-connected. The domain is said to be simply-connected if any closed surface can be placed within the domain, to cover the

whole of the domain, and then be shrunk to a single point without leaving the domain. The α -domain of Figure 2.1 (a) is an example of a simply connected domain. A multiply-connected domain is a connected domain which is also bounded from the inside by one or more disjoint closed surfaces, as illustrated by the α -domain in Figure 2.1 (b).

A spatial domain is called non-connected if it is composed of a union of disjoint domains, with disjoint boundaries. The β -domain in Figure 2.1 (b) is non-connected.



(a) The α -phase is simply-connected.

(b) The α -phase is multiply-connected, while the β -phase is non-connected.

Figure 2.1: Samples of porous media which illustrate the different types of connectivity.

2.2.2 Homogeneity and heterogeneity

Bear and Bachmat (1991) states that a domain of a porous medium is homogeneous with respect to a particular macroscopic parameter (say γ) characterising a specific phase of the domain, if that parameter has the same value for all the points in the domain. In other words,

$$\nabla\gamma = \underline{0}. \quad (2.1)$$

A domain within a porous medium may be said to be heterogeneous if the particular parameter change from one point to another within the domain.

2.2.3 Isotropy and anisotropy

A porous medium is isotropic with respect to a given property at a certain point in the domain of the medium, if that property is invariant under rotation at that point. On the other hand, if a property varies under rotation at a certain point, the porous medium is referred to as anisotropic with respect to that property. The permeability of a porous medium to fluid is an example of an anisotropic property.

2.2.4 Porous environments

For the purpose of this study, porous media may be categorised in mainly three different porous environments, namely foam-like materials, granular materials and prismatic bundles. It is considered that any porous material may be related to one of these environments. This work will mainly focus on the latter.

Foam-like materials

Foam-like materials have the distinct feature that the solid phase is simply connected. This property holds for all values of the porosity. Foam-like materials may therefore be referred to as consolidated materials. A pore-scale model for foam-like materials were developed by Du Plessis and Masliyah (1988).

Granular materials

In the case of granular materials, the solid phase is viewed as non-connected. Granular materials are therefore considered to be the inverse of foam-like materials. Granular materials usually consist of separate granules, but in the case of sandstone, where the granules may be stuck to each other, a granular structure may still be identified although the granules form a consolidated matrix. A pore-scale model for granular porous media was developed by Du Plessis and Masliyah (1991) and quantified against the Ergun equation by Du Plessis (1994).

Prismatic bundles

The solid material consists of bundles of unidirectional fibres or tubes. The prismatic bundle is therefore merely a two-dimensional representation of the granular model when cross-flow is considered. The direction of discharge is either normal to the fibres or in the same direction of the fibres. In this study only cross-flow is considered. An appropriate pore-scale model for prismatic bundles was developed by Du Plessis (1991).

2.3 Porous media modelling parameters

Macroscopic measurable parameters need to be chosen to fully classify the porous media under consideration. These parameters are essential for the development of pore-scale models and accurate flow analysis. A number of geometric properties, which are used to characterise porous media, will also be discussed in this section. Some of these parameters may be well known in literature, but interpreted differently by different authors. It is therefore important to present clear definitions of the parameters to cohere this study with other literature.

2.3.1 Porosity

The porosity, ϵ , of a material is the ratio between the void volume \mathcal{U}_f and the total volume \mathcal{U}_0 of a two-phase porous medium representative sample. Some literature refers to the porosity as the void fraction. By definition the porosity is given by

$$\epsilon = \frac{\mathcal{U}_f}{\mathcal{U}_0} = 1 - \frac{\mathcal{U}_s}{\mathcal{U}_0}, \quad (2.2)$$

where \mathcal{U}_s is the solid volume of the representative sample.

A porosity of zero implicates a solid material, while a porosity of one implies a void space. In general it is quite possible for the porosity to vary throughout the porous medium (i.e. $\nabla\epsilon \neq 0$). It is also possible for the porosity to change over a time interval under consideration (i.e. $\frac{\partial\epsilon}{\partial t} \neq 0$). The latter scenario is an example of mass transfer in chemical reactors.

There exist different techniques to measure the porosity of a porous medium sample. Brief descriptions of a few of these methods are presented by Dullien (1979).

2.3.2 Permeability

According to Dullien (1979), permeability is the term used for the conductivity of the porous medium with respect to permeation by a Newtonian fluid. In this general sense, the value of the permeability is subject to variation with the properties of the permeating fluid as well as flow mechanisms within the porous media. In addition, the specific permeability k is also often used because it is independent of both fluid properties and flow mechanisms.

The permeability k is defined by Darcy's Law. In 1856 a French Engineer, Henry Darcy, investigated the flow of water in vertical homogeneous sand filters in connection with the fountains of the city of Dijon, France (Bear, 1972). He performed a series of experiments which led to the following expression

$$q = -\frac{k}{\mu} \frac{dp}{dx}, \quad (2.3)$$

if it is assumed that the mean discharge through the porous medium is in the x -direction. The superficial velocity is denoted by q , the viscosity of the traversing fluid by μ and the pressure gradient in the x -direction by dp/dx . Equation (2.3) is known as Darcy's Law for creep flow through a porous medium.

A practical unit of permeability is the *Darcy* and may be defined as follows (Dullien, 1979): A porous material has a permeability equal to 1 *Darcy* if a pressure drop of 1 *atm* will produce a flow rate of 1 cm^3/sec of a fluid with 1 *cP* viscosity through a cube having sides 1 *cm* in length.

The permeability may be obtained experimentally by performing a series of measurements at very low Reynolds numbers. By plotting the Reynolds numbers versus the pressure drop, the linear relationship between the two entities can be obtained by fitting the data with a straight line. The permeability can then be obtained from the slope. Details and more advance methods of measuring permeability are discussed by Dullien (1979).

2.3.3 Specific surface areas

The static or geometric specific area is defined as the ratio of the total interstitial surface area of the pore-space to the volume of the solid particles. Symbolically this geometric parameter may be written as

$$\mathcal{A}_{vs} = \frac{\mathcal{S}_{fs}}{\mathcal{U}_s}. \quad (2.4)$$

Parameters that affect the specific area of a porous material are pointed out by Bear (1972) and include the porosity, mode of packing and also the grain size and shape. This area plays a vital role in processes where absorption, mass transfer and electric interactions take place. Dullien (1979) briefly describes a few methods to measure specific areas of porous materials.

It is possible for particles to overlap and also for stagnant regions to occur. The dynamic specific area, \mathcal{A}_{vd} , is therefore defined to be the ratio of the surface area presented by particles to the flow to the volume of the solid particles (Comiti and Renaud, 1989). In general, the dynamic specific area is smaller than the static specific area.

2.3.4 Staggeredness

Another property of a porous medium, besides connectivity, that should be taken into consideration when analysing the amount of pore-space traversed by fluid, is the staggeredness of the porous medium. The amount of staggeredness of a porous medium describes the degree to which the solid phase is irregularly distributed throughout the domain.

The two extreme degrees of staggeredness are illustrated in Figure 2.2. In the case of minimum staggering some of the channels may contain stagnant fluid, while other channels contain all of the moving fluid. In the case of maximum staggering, the fluid is forced to traverse all of the available channels at all times. Figure 2.2 (a) shows zones of fluid between the consecutive cylinders that will not contribute to flow in the overall flow direction. These zones may contain stagnant fluid. Figure 2.2 (b) shows that the fluid is also forced to move locally through the void channels in a direction normal to the mean flow direction, thereby traversing all of the void channels.

The stagnant zones that are formed as a consequence of the degree of staggeredness and connectivity may cause the porosity of the porous medium to appear different than it is. The fluid zones that do not contribute to the flow through the porous medium should be considered during the analysis of the flow field.

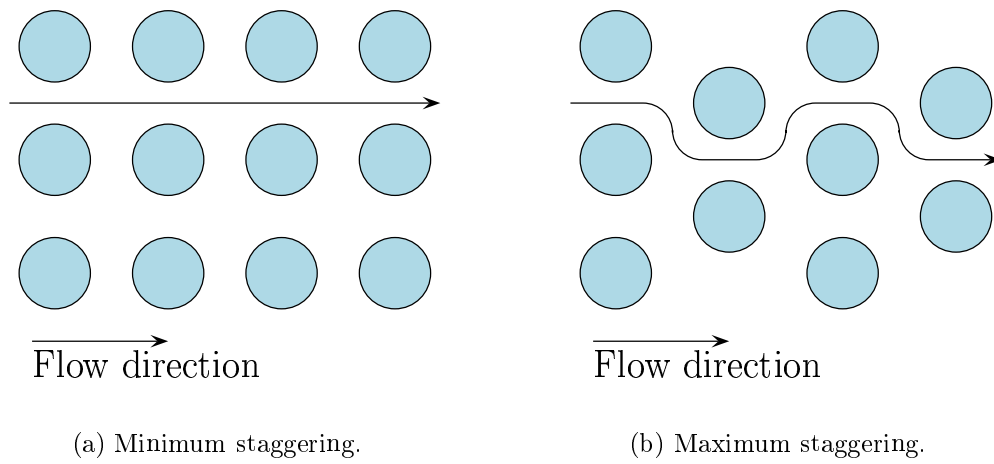


Figure 2.2: A two-dimensional schematic representation of the staggeredness of a porous medium.

Chapter 3

Volume averaging

The porous media investigated in this work are two phase systems, consisting of a solid phase and a fluid phase. In general, the phases are separated by highly irregular surfaces. The variables and balance laws that describe the behaviour of the two phases are defined at the microscopic level. Due to the complexity of the interconnecting channels within a relative large domain of the porous system, it is impractical to solve the balance laws on the microscopic level. Different methods exist to transform the microscopic quantities and equations to the macroscopic level. This transformation enables one to view the porous medium as a continuum. This work only considers the volume averaging procedure.

3.1 The representative elementary volume (REV)

The domain used for the averaging procedures is termed the Representative Elementary Volume (REV). A clear description of an REV is given by Bear and Buchlin (1991). An REV may be defined as a volume \mathcal{U}_0 which contains both solid parts, denoted by \mathcal{U}_s , as well as fluid or void parts, denoted by \mathcal{U}_f . This should be true no matter where in the porous domain the REV is visualised. Moreover, the REV should be statistically representative of the geometric properties of the porous medium. The REV may be visualised in any shape, but a circular two-dimensional representation of an REV is given in Figure 3.1.

Within the REV the interface between the solid and the fluid phases is denoted by \mathcal{S}_{fs} . The boundary of an REV consists of two types of interfaces. The fluid-fluid interfaces will be denoted by \mathcal{S}_{ff} while the solid-solid interfaces will be denoted by \mathcal{S}_{ss} . A centroid is

associated with each REV and denoted by the vector \underline{x}_0 from a specified reference frame, as shown in Figure 3.1. The vector \underline{x} may be used to reference any other point within the REV, may it be in the fluid phase or in the solid phase.

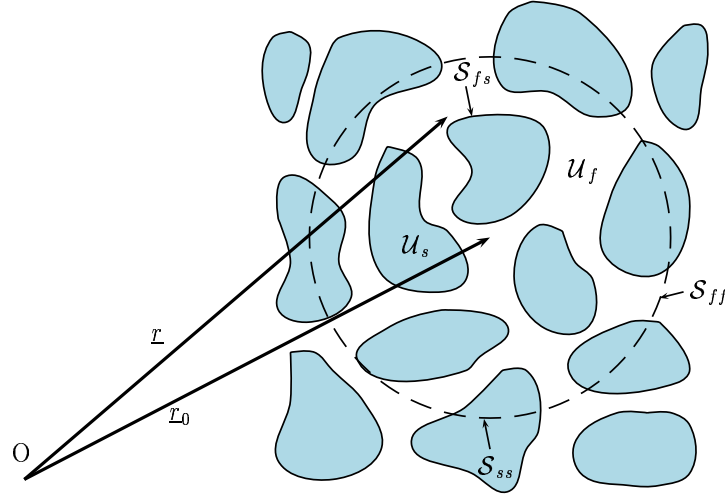


Figure 3.1: A two-dimensional representation of a Representative Elementary Volume taken from a sample of a porous medium.

Selecting the appropriate size for an REV is a topic that is of major discussion in literature. Bear and Buchlin (1991) give an in depth analysis of the situation at hand. A very important concept concerning the matter is that the REV needs to be statistically representative of the average geometric properties of the porous medium, as previously mentioned. Therefore the size of the REV needs to be far greater than some characteristic length of the micro-structure of the porous medium l , as to contain enough solids and fluids or voids. The size of the REV also needs to be far less than the macroscopic characteristic length or boundary of the porous medium L as to be small enough to be considered an elementary unit. In short, the following bounds are imposed on \mathcal{U}_0

$$l^3 \ll \mathcal{U}_0 \ll L^3. \quad (3.1)$$

Overlapping REV's may now be used to traverse the whole of the porous domain by filling in the domain with REV centroids. Averages of the concerned microscopic or interstitial variables may be taken over an REV and the values assigned to the REV centroid. It does not matter if the centroid lies outside the phase where the interstitial variables were taken from. In this manner the porous domain becomes a continuum of macroscopic variable

quantities.

3.2 Phase averages and deviation

The intrinsic phase average, $\langle \psi \rangle_f$, of any tensorial quantity, ψ , defined within the fluid phase, \mathcal{U}_f , is defined by

$$\langle \psi \rangle_f \equiv \frac{1}{\mathcal{U}_f} \iiint_{\mathcal{U}_f} \psi \, d\mathcal{U} \quad (3.2)$$

at the REV centroid, \underline{x}_0 .

In a similar manner the phase average of a tensorial quantity, ψ , defined within the fluid phase, \mathcal{U}_f , is defined by

$$\langle \psi \rangle \equiv \frac{1}{\mathcal{U}_0} \iiint_{\mathcal{U}_f} \psi \, d\mathcal{U} \quad (3.3)$$

at the REV centroid, \underline{x}_0 . The integration may also be performed over the entire volume, \mathcal{U}_0 , as long as the contribution of ψ within the solid phase, \mathcal{U}_s , is equal to zero.

The deviation of any fluid quantity at some point in the fluid phase is related to the intrinsic phase average of a specific REV in the following manner

$$\{\psi\} \equiv \psi - \langle \psi \rangle_f, \quad (3.4)$$

and coincides with the REV centroid, \underline{x}_0

3.3 Averaging identities

The following identities may be proven with little effort using the definitions of the volume averaging and the deviation given by (3.2), (3.3) and (3.4) respectively. Here α represents

a constant while ψ and λ represent tensorial quantities of equal order. The derivations concerning these identities are given in Appendix A for the sake of completeness.

$$\langle \psi + \lambda \rangle = \langle \psi \rangle + \langle \lambda \rangle \quad (3.5)$$

$$\langle \alpha \psi \rangle = \alpha \langle \psi \rangle \quad (3.6)$$

$$\langle \{\psi\} \rangle = 0 = \{\langle \psi \rangle\} \quad (3.7)$$

$$\{\{\psi\}\} = \{\psi\} \quad (3.8)$$

$$\langle \langle \psi \rangle \rangle = \epsilon \langle \psi \rangle \quad (3.9)$$

$$\langle \{\psi\} \langle \lambda \rangle \rangle = 0 = \langle \langle \psi \rangle \{\lambda\} \rangle \quad (3.10)$$

$$\langle \{\psi\} \{\lambda\} \rangle = \langle \psi \{\lambda\} \rangle = \langle \{\psi\} \lambda \rangle \quad (3.11)$$

$$\langle \psi \lambda \rangle = \langle \psi \rangle \langle \lambda \rangle / \epsilon + \langle \{\psi\} \{\lambda\} \rangle \quad (3.12)$$

$$\{\psi \lambda\} = \{\psi\} \langle \lambda \rangle_f + \langle \psi \rangle_f \{\lambda\} + \{\psi\} \{\lambda\} - \langle \{\psi\} \{\lambda\} \rangle_f \quad (3.13)$$

3.4 Slattery's averaging theorem

When averaging an equation, for example the momentum transport equation, the need arises to express the average of a gradient in terms of the gradient of the average. This can be done by use of Slattery's averaging theorem (Slattery, 1967), which states

$$\nabla \iiint_{\mathcal{U}_f} \psi \, d\mathcal{U} = \iint_{\mathcal{S}_{ff}} \underline{n} \psi \, d\mathcal{S}, \quad (3.14)$$

where \underline{n} denotes the unit normal pointing out of the fluid phase. A derivation of Slattery's averaging theorem may be found in Appendix B.

Although (3.14) cannot be used directly in the averaging of a gradient, it forms the basis of the spatial averaging theorem

$$\langle \nabla \psi \rangle = \nabla \langle \psi \rangle + \frac{1}{\mathcal{U}_0} \iint_{\mathcal{S}_{fs}} \underline{n} \psi \, d\mathcal{S}, \quad (3.15)$$

which is more useful in averaging procedures.

3.5 Identities based on the averaging theorem

The following identities are based on Slattery's averaging theorem. The derivations of these identities may be found in Appendix C.

$$\langle \nabla \psi \rangle = \nabla \langle \psi \rangle + \frac{1}{\mathcal{U}_0} \iint_{\mathcal{S}_{fs}} \underline{n} \psi \, d\mathcal{S} \quad (3.16)$$

$$\langle \nabla \cdot \psi \rangle = \nabla \cdot \langle \psi \rangle + \frac{1}{\mathcal{U}_0} \iint_{\mathcal{S}_{fs}} \underline{n} \cdot \psi \, d\mathcal{S} \quad (3.17)$$

$$\langle \nabla \psi \rangle = \epsilon \nabla \langle \psi \rangle_f + \frac{1}{\mathcal{U}_0} \iint_{\mathcal{S}_{fs}} \underline{n} \{ \psi \} \, d\mathcal{S} \quad (3.18)$$

$$\langle \nabla \cdot \psi \rangle = \epsilon \nabla \cdot \langle \psi \rangle_f + \frac{1}{\mathcal{U}_0} \iint_{\mathcal{S}_{fs}} \underline{n} \cdot \{ \psi \} \, d\mathcal{S} \quad (3.19)$$

$$\langle \nabla^2 \psi \rangle = \nabla^2 \langle \psi \rangle + \frac{1}{\mathcal{U}_0} \iint_{\mathcal{S}_{fs}} \underline{n} \cdot \nabla \psi \, d\mathcal{S} + \frac{1}{\mathcal{U}_0} \nabla \cdot \left(\iint_{\mathcal{S}_{fs}} \underline{n} \psi \, d\mathcal{S} \right) \quad (3.20)$$

$$\nabla \epsilon = -\frac{1}{\mathcal{U}_0} \iint_{\mathcal{S}_{fs}} \underline{n} \, d\mathcal{S} \quad (3.21)$$

$$\nabla \epsilon = \frac{1}{\mathcal{U}_0} \iint_{\mathcal{S}_{ff}} \underline{n} \, d\mathcal{S} \quad (3.22)$$

$$\nabla \cdot \langle \psi \rangle = \frac{1}{\mathcal{U}_0} \iint_{\mathcal{S}_{ff}} \underline{n} \cdot \psi \, d\mathcal{S} \quad (3.23)$$

In the above equations ψ may be used for any order tensorial quantity and the normal \underline{n} points out of the fluid phase and into the solid phase.

3.6 Averaging of time derivatives

It will prove to be useful to obtain the change of some tensorial function ψ with respect to time within the void volume \mathcal{U}_f . While considering a stationary REV volume \mathcal{U}_0 , the void volume \mathcal{U}_f may still change magnitude and shape within the REV volume. Application of the well known Leibniz theorem to ψ within \mathcal{U}_f yields

$$\frac{d}{dt} \iiint_{\mathcal{U}_f(t)} \psi d\mathcal{U} = \iiint_{\mathcal{U}_f(t)} \frac{\partial \psi}{\partial t} d\mathcal{U} + \iint_{\partial \mathcal{U}_f(t)} \underline{n} \cdot \underline{w} \psi d\mathcal{S}. \quad (3.24)$$

Here \underline{n} denotes the outwardly normal of the fluid phase and \underline{w} the velocity of the points on the boundary $\partial \mathcal{U}_f(t)$.

Since the selected REV is stationary in space, the total time derivative may be changed to a partial time derivative, although \mathcal{U}_f is subject to change within \mathcal{U}_0 . Equation (3.24) may now be written as

$$\frac{1}{\mathcal{U}_0} \iiint_{\mathcal{U}_f(t)} \frac{\partial \psi}{\partial t} d\mathcal{U} = \frac{\partial}{\partial t} \left(\frac{1}{\mathcal{U}_0} \iiint_{\mathcal{U}_f(t)} \psi d\mathcal{U} \right) - \frac{1}{\mathcal{U}_0} \iint_{\partial \mathcal{U}_f(t)} \underline{n} \cdot \underline{w} d\mathcal{S}. \quad (3.25)$$

The fluid boundary $\partial \mathcal{U}_f(t)$ may be decomposed into \mathcal{S}_{fs} and \mathcal{S}_{ff} to yield, along with the application of the phase averaging rules, the following form of (3.25)

$$\left\langle \frac{\partial \psi}{\partial t} \right\rangle = \frac{\partial \langle \psi \rangle}{\partial t} - \frac{1}{\mathcal{U}_0} \iint_{\mathcal{S}_{fs}} \underline{n} \cdot \underline{w} \psi d\mathcal{S} - \frac{1}{\mathcal{U}_0} \iint_{\mathcal{S}_{ff}} \underline{n} \cdot \underline{w} d\mathcal{S}. \quad (3.26)$$

The integral over the fluid-fluid interface is zero since it coincides with the stationary \mathcal{U}_0 , implying that $\underline{w} = \underline{0}$. In the case of viscous fluids the velocity of the fluid-solid interface is the same as the velocity of the fluid directly adjacent to it. This leaves us with the

following expression for the average of a time derivative

$$\left\langle \frac{\partial \psi}{\partial t} \right\rangle = \frac{\partial \langle \psi \rangle}{\partial t} - \frac{1}{\mathcal{U}_0} \iint_{\mathcal{S}_{fs}} \underline{n} \cdot \underline{v} \, d\mathcal{S}, \quad (3.27)$$

where \underline{v} is the velocity of the fluid.

3.7 Interstitial transport variables

The balance equations governing the interstitial flow phenomena may be averaged according to the volumetric averaging approach to produce macroscopic balance equations. This procedure simplifies the flow problem in the highly irregular interpenetrating continua as it describes the average behaviour of the system.

Before averaging the balance equations governing the flow within the pore structure, definitions of some geometric variables as well as averaged velocity and pressure variables are necessary.

3.7.1 Flow directions

At each point within \mathcal{U}_f , the unit vector $\tilde{\underline{n}}$ represents the direction of the local or microscopic transport velocity \underline{v} . The magnitude and direction of the local transport velocity are dependent on position. A few local transport velocity unit vectors are illustrated in Figure 3.2. The unit vector for the direction of the average velocity within an REV is denoted by $\hat{\underline{n}}$ and is referred to as the stream-wise or average direction. This unit vector is present at any point within the porous domain and is situated at the centroid of the REV. For clarity, the stream-wise unit vector is illustrated outside of the REV in Figure 3.2.

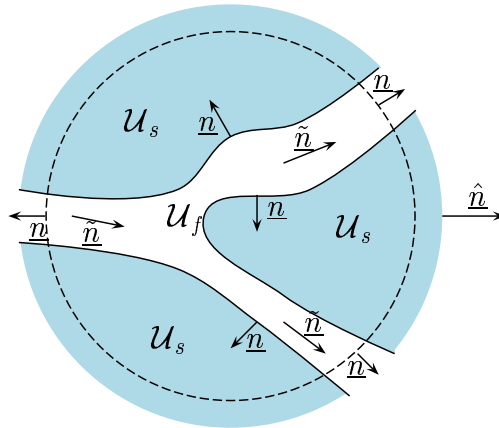


Figure 3.2: A two-dimensional representation of an REV with the different unit vectors for velocity directions.

3.7.2 Geometric variables

Tortuosity and lineality

There exists many different definitions and interpretations for tortuosity (Clennell, 1997). The most basic definition of tortuosity is the path length tortuosity, which may be defined as the ratio of the average length of the tortuous flow path L_e to the straight line length L in the stream-wise direction

$$\chi = \frac{L_e}{L}. \quad (3.28)$$

Tortuosity is a property of a porous medium that is dependent on the porosity as well as the type of porous medium. It affects both the driving force and the velocity of the fluid (Bear, 1972). Lineality is a measure of the straightness of the tortuous flow path (Du Plessis and Diedericks, 1997). It may be defined as the inverse of tortuosity, in other words the ratio of the straight line length L in the stream-wise direction to the average length of the tortuous flow path L_e ,

$$\mathcal{L} = \frac{L}{L_e}. \quad (3.29)$$

Thus far only the scalar components of the tortuosity and the lineality in the stream-wise direction have been discussed. In a general three-dimensional environment the lineality and tortuosity need to be described by tensorial quantities. Diedericks (1999) showed that the lineality may be described in terms of volumes as follows

$$\underline{\underline{\mathcal{L}}} = \frac{1}{\mathcal{U}_f} \iiint_{\mathcal{U}_f} \hat{n} \tilde{n} d\mathcal{U}. \quad (3.30)$$

Tortuosity and lineality are, as mentioned above, the inverse of one another

$$\underline{\underline{\mathcal{L}}} \cdot \underline{\underline{\chi}} = \underline{\underline{1}}, \quad (3.31)$$

where $\underline{\underline{1}}$ is the unity dyadic.

Effective streamwise volume

The effective stream-wise volume may be defined as that part of the fluid volume of the REV that directly contributes to the transport of the fluid in the stream-wise direction. Mathematically the effective stream-wise volume may be defined as

$$\mathcal{U}_{||} = \iiint_{\mathcal{U}_f} \hat{n} \cdot \tilde{n} d\mathcal{U}. \quad (3.32)$$

3.7.3 Velocity and pressure variables

An advantage of the volume averaging approach is that it provides useful physical insight into the relationship between macroscopic and microscopic variables. For example, it produces mathematical parameters which correlate with certain parameters that may be directly measurable.

The intrinsic phase average of the microscopic velocity \underline{v} within the fluid phase is denoted

by

$$\underline{u} = \langle \underline{v} \rangle_f = \frac{1}{\mathcal{U}_f} \iiint_{\mathcal{U}_f} \underline{v} d\mathcal{U}. \quad (3.33)$$

This represents the average velocity of all fluid particles in the stream-wise direction. This macroscopic variable is an example of a physical quantity that is not directly measurable.

A very important macroscopic quantity is the superficial or Darcy velocity \underline{q} and it is defined by the phase average of the interstitial fluid velocity \underline{v}

$$\underline{q} = \langle \underline{v} \rangle = \frac{1}{\mathcal{U}_0} \iiint_{\mathcal{U}_f} \underline{v} d\mathcal{U}. \quad (3.34)$$

The superficial velocity represents the average velocity of the fluid, should there be a section within the macroscopic boundaries where no porous medium is present. This macroscopic variable is thus directly measurable and it is more appropriate to express the macroscopic balance equations in terms of the superficial velocity. The only disadvantage of the superficial velocity is that it is less representative of the interstitial flow velocities. Note that the unit vector in the stream-wise direction may be mathematically defined as

$$\hat{\underline{n}} = \underline{q}/q, \quad (3.35)$$

where q represents the magnitude of \underline{q} .

Another velocity which gives more accurate description of the intra-pore flow phenomena is the effective interstitial velocity, $\tilde{\underline{w}}$, which is defined as the hypothetical velocity field, collinear with \underline{v} at each point within \mathcal{U}_f and of constant magnitude \tilde{w} within the REV, which yields the same stream-wise discharge through \mathcal{U}_f as the actual interstitial velocity field \underline{v} (Du Plessis and Diedericks, 1997).

The stream-wise average pore velocity $\hat{\underline{w}}$ may now be defined as

$$\hat{\underline{w}} = \tilde{w} \hat{\underline{n}} = \frac{1}{\mathcal{U}_{\parallel}} \iiint_{\mathcal{U}_f} \underline{v} d\mathcal{U}. \quad (3.36)$$

The stream-wise pore velocity may therefore be viewed as the volume integral of the actual microscopic flux weighed over the effective stream-wise volume $\mathcal{U}_{||}$.

The intrinsic phase average of the pressure variable is determined by

$$\langle p \rangle_f = \frac{1}{\mathcal{U}_f} \iiint_{\mathcal{U}_f} p d\mathcal{U}. \quad (3.37)$$

When applying pressure taps along a packed column during flow through the column, the interstitial pressure $\langle p \rangle_f$ is the physical quantity being measured. It is therefore physically more realistic to use the intrinsic phase average of the pressure in the macroscopic balance equations.

3.7.4 Velocity relationships

The superficial velocity is related to the intrinsic phase average velocity in the following manner

$$\underline{q} = \epsilon \underline{u}. \quad (3.38)$$

This relation follows from the volumetric averages defined in (3.34) and (3.33) respectively, along with the definition of porosity.

Projection of directional volumes need to be incorporated in the definitions to obtain a relation between the superficial velocity and the effective interstitial velocity. The effective interstitial velocity is used as a good approximation for the actual microscopic velocity, because it produces the same discharge and it is more representative of the actual velocity than the intrinsic phase average velocity.

The integral

$$\iiint_{\mathcal{U}_f} v \underline{\tilde{n}} d\mathcal{U} \quad (3.39)$$

yields a stream-wise resultant vector. Here the magnitude v of \underline{v} and the directional unit

vector $\tilde{\underline{n}}$ are both position dependent. If v is replaced by \tilde{w} then, according to Du Plessis and Diedericks (1997), to ensure a resultant stream-wise vector, the following projection of the $\tilde{\underline{n}}$ -field need to be made

$$\iiint_{\mathcal{U}_f} v \tilde{\underline{n}} d\mathcal{U} = \tilde{w} \hat{\underline{n}} \hat{\underline{n}} \cdot \iiint_{\mathcal{U}_f} \tilde{\underline{n}} d\mathcal{U}. \quad (3.40)$$

This equation, where the variable velocity value is replaced by the constant average velocity value, is used to obtain a better estimate of the average interstitial velocity to be used in pore-scale modelling calculations.

Equation (3.33) may be used to write (3.40) as

$$\langle \underline{v} \rangle_f = \tilde{w} \hat{\underline{n}} \cdot \frac{1}{\mathcal{U}_f} \iiint_{\mathcal{U}_f} \tilde{\underline{n}} \hat{\underline{n}} d\mathcal{U}, \quad (3.41)$$

where the constant stream-wise unit vector was taken into the integral on the left hand side of (3.40). Equation (3.38) may now be used along with the lineality tensor (3.30) to obtain the following relation between the superficial velocity and the effective interstitial velocity

$$\underline{q} = \epsilon \hat{\underline{w}} \cdot \underline{\underline{\mathcal{L}}} \quad (3.42)$$

with the use of (3.41). Scalar multiplication of (3.42) with the tortuosity tensor yields

$$\underline{q} \cdot \underline{\underline{\chi}} = \epsilon \hat{\underline{w}}. \quad (3.43)$$

The differences in magnitudes of the different velocity types are illustrated in Figure 3.3. A mathematical quantification of the intuitively understood magnitude relations of the velocity types is given by

$$q = \epsilon u = \epsilon w \mathcal{L}, \quad (3.44)$$

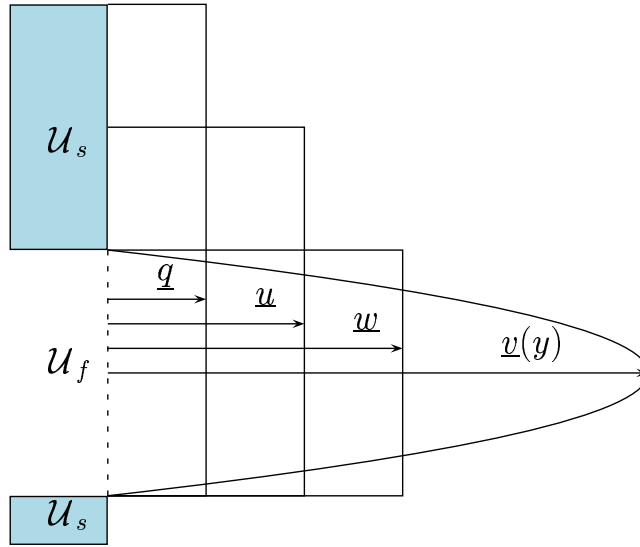


Figure 3.3: A schematic representation of the different velocity relationships (Taken from Diedericks (1992)).

in the stream-wise direction. It should be noted that both ϵ and \mathcal{L} are smaller or equal to unity, where the scalar \mathcal{L} is the stream-wise lineality defined by

$$\mathcal{L} = \hat{n} \cdot \underline{\underline{\mathcal{L}}} \cdot \hat{n}. \quad (3.45)$$

In the same manner a stream-wise tortuosity scalar may be defined as

$$\chi = \hat{n} \cdot \underline{\underline{\chi}} \cdot \hat{n} \quad (3.46)$$

to yield the following relation in the stream-wise direction

$$w = \frac{q\chi}{\epsilon}. \quad (3.47)$$

Equation (3.47) is used frequently throughout the literature and is in agreement with the equation obtained by Carman (1937) for a capillary model.

3.8 Conservation of mass

The conservation of mass for any fluid phase is governed by the continuity equation

$$\frac{\partial \rho}{\partial t} + \nabla \cdot (\rho \underline{v}) = 0. \quad (3.48)$$

The phase average of (3.48) after applying (3.5) and (3.6) yields

$$\left\langle \frac{\partial \rho}{\partial t} \right\rangle + \langle \nabla \cdot (\rho \underline{v}) \rangle = 0. \quad (3.49)$$

The identity for averaging of a time derivative (3.27) is used in conjunction with identities concerning the average of a gradient and the average of a product, (3.17) and (3.12) respectively, to obtain

$$\frac{\partial \langle \rho \rangle}{\partial t} - \frac{1}{\mathcal{U}_0} \iint_{\mathcal{S}_{fs}} \underline{n} \cdot \underline{v} d\mathcal{S} + \nabla \cdot (\langle \rho \rangle \langle \underline{v} \rangle / \epsilon) \quad (3.50)$$

$$+ \nabla \cdot \langle \{\rho\} \langle \underline{v} \rangle \rangle + \frac{1}{\mathcal{U}_0} \iint_{\mathcal{S}_{fs}} \underline{n} \cdot \underline{v} \rho d\mathcal{S} = 0. \quad (3.51)$$

Both the surface integrals contain the scalar product $(\underline{n} \cdot \underline{v})$. In case of a no-slip boundary condition, this product will be zero everywhere on the surface \mathcal{S}_{fs} . If a slip condition is pursued, with flow parallel to the surface, this scalar product also reduce to zero on the entire surface \mathcal{S}_{fs} . In the case of incompressible fluids, the density ρ may be assumed spatially as well as temporally constant, which reduces the time derivative to zero as well as the deviation of the density $\{\rho\}$. In such cases, the phase averaged continuity equation simplifies to

$$\nabla \cdot (\langle \rho \rangle \langle \underline{v} \rangle / \epsilon) = 0 \quad (3.52)$$

and

$$\rho \nabla \cdot (\langle 1 \rangle \langle \underline{v} \rangle / \epsilon) = 0 \quad (3.53)$$

and thus

$$\nabla \cdot \underline{q} = 0. \quad (3.54)$$

3.9 Momentum transport

Interstitial momentum transport of an incompressible Newtonian fluid is governed by

$$\rho \frac{\partial \underline{v}}{\partial t} + \nabla \cdot (\rho \underline{v} \underline{v}) - \rho \underline{g} + \nabla p - \nabla \cdot \underline{\underline{\tau}} = \underline{0}. \quad (3.55)$$

The gravitational force per unit mass is denoted by \underline{g} and $\underline{\underline{\tau}}$ is associated with the shear stress tensor. In the case of a Newtonian fluid the stress tensor is related to the gradient of the velocity as follows

$$\underline{\underline{\tau}} = \frac{\mu}{2} (\nabla \underline{v} + \widetilde{\nabla \underline{v}}), \quad (3.56)$$

with the proportionality constant μ , known as the constant viscosity of the fluid (Whitaker, 1968). The divergence of the shear stress tensor results in

$$\nabla \cdot \underline{\underline{\tau}} = \mu \nabla^2 \underline{v}, \quad (3.57)$$

which may be inserted in the momentum equation to yield the Navier-Stokes equation

$$\rho \frac{\partial \underline{v}}{\partial t} + \nabla \cdot (\rho \underline{v} \underline{v}) - \rho \underline{g} + \nabla p - \mu \nabla^2 \underline{v} = \underline{0}. \quad (3.58)$$

According to identity (3.5), volume averaging of the Navier-Stokes equations may be done term by term.

The temporal term in (3.58) may be averaged with the use of (3.27) to yield

$$\left\langle \rho \frac{\partial \underline{v}}{\partial t} \right\rangle = \rho \frac{\partial \underline{q}}{\partial t}, \quad (3.59)$$

where the surface integral is omitted for the same reasons as in section 3.8.

The convective term in (3.58) may be averaged by using (3.6), (3.17) and (3.12) to yield

$$\begin{aligned} \langle \nabla \cdot (\rho \underline{v} \underline{v}) \rangle &= \rho \nabla \cdot \langle \underline{v} \underline{v} \rangle + \frac{\rho}{\mathcal{U}_0} \iint_{\mathcal{S}_{fs}} \underline{n} \cdot (\underline{v} \underline{v}) d\mathcal{S} \\ &= \rho \nabla \cdot (\underline{q} \underline{q} / \epsilon) + \rho \nabla \cdot \langle \{v\} \{v\} \rangle \end{aligned} \quad (3.60)$$

where the surface integral reduces to zero for the same reasons as in section 3.8.

The body force of equation (3.58) is averaged as

$$\begin{aligned} \langle \rho \underline{g} \rangle &= \rho \underline{g} \langle 1 \rangle \\ &= \epsilon \rho \underline{g}. \end{aligned} \quad (3.61)$$

By applying (3.18) the pressure term may be averaged to yield

$$\langle \nabla p \rangle = \epsilon \nabla \langle p \rangle_f + \frac{1}{\mathcal{U}_0} \iint_{\mathcal{S}_{fs}} \underline{n} \{p\} d\mathcal{S}. \quad (3.62)$$

Finally, the diffusion term is averaged by applying (3.20) to obtain

$$\begin{aligned} \langle \mu \nabla^2 \underline{v} \rangle &= \mu \nabla^2 \langle \underline{v} \rangle + \frac{\mu}{\mathcal{U}_0} \iint_{\mathcal{S}_{fs}} \underline{n} \cdot \nabla \underline{v} d\mathcal{S} + \frac{\mu}{\mathcal{U}_0} \nabla \cdot \left(\iint_{\mathcal{S}_{fs}} \underline{n} \underline{v} d\mathcal{S} \right) \\ &= \mu \nabla^2 \underline{q} + \frac{\mu}{\mathcal{U}_0} \iint_{\mathcal{S}_{fs}} \underline{n} \cdot \nabla \underline{v} d\mathcal{S}. \end{aligned} \quad (3.63)$$

Equations (3.59) to (3.63) may be combined to yield the macroscopic Navier-Stokes equation

$$\begin{aligned} \rho \frac{\partial \underline{q}}{\partial t} + \rho \nabla \cdot (\underline{q} \underline{q} / \epsilon) + \rho \nabla \cdot \langle \{\underline{v}\} \{\underline{v}\} \rangle + \epsilon \nabla \langle p \rangle_f - \epsilon \rho \underline{g} \\ - \mu \nabla^2 \underline{q} + \frac{1}{\mathcal{U}_0} \iint_{\mathcal{S}_{fs}} (\underline{n} \{p\} - \mu \underline{n} \cdot \nabla \underline{v}) d\mathcal{S} = 0. \end{aligned} \quad (3.64)$$

If \underline{q} is assumed to be constant with respect to time and uniform in space, (3.64) reduces to the volumetrically averaged time independent form of the momentum equation and may be written as

$$-\epsilon \nabla P_f = \frac{1}{\mathcal{U}_0} \iint_{\mathcal{S}_{fs}} (\underline{n} \{p\} - \mu \underline{n} \cdot \nabla \underline{v}) d\mathcal{S}, \quad (3.65)$$

where $\nabla P_f = \nabla \langle p \rangle_f - \rho \underline{g}$ is the macroscopic pressure head, which includes the gravity term.

The surface integral in (3.65) is dependent on the microscopic geometry and internal flow configuration of the porous medium. An adequate pore-scale modelling procedure is needed to approximate values of the surface integral in terms of measurable parameters. This procedure is known as closure and will be discussed further in Chapter 5.

Chapter 4

The Rectangular Representative Unit Cell

The actual interstitial pore-space is seldom amenable to rigorous analysis due to the vast amount of structural data required. This chapter provides a pore-scale model to approximate the surface integral in (3.65). This model was first proposed by Du Plessis and Masliyah (1988). This work is mainly concerned with Newtonian fluids in homogeneous isotropic porous media and the pore-scale model is introduced accordingly.

4.1 Properties of the RRUC

The modelling procedure of Du Plessis and Masliyah (1988) aims to approximate the porous material by embedding the average characteristic properties of the porous material within the smallest hypothetical unit cell of rectangular geometry. The built-in properties of the Rectangular Representative Unit Cell (RRUC) should be consistent with that of the REV with volumetric centroid collocated at the same point as that of the unit cell. The difference between the RRUC and the REV is that the latter is large enough to give representative averages, whereas the former is of minimal size and contains the average geometry. Suitable arrangements of rectangular solid blocks may be used to obtain these average geometric characteristics within the RRUC. An arrangement of rectangular blocks was initially used to simplify computation in the pore-space.

The RRUC should be orientated in such a manner that the normal vector to one of its

faces points in the stream-wise direction \hat{n} as defined by the fluid motion within the REV. It is assumed that a stream tube may be associated with the particular RRUC face which faces downstream. In other words, all fluid enters the RRUC through the upstream face of the RRUC and exits through the downstream face, with no lateral fluid exchange over the flanks of the RRUC.

It should be noted that the RRUC is not a repetitive building block, as in the case of network models, since it is impossible to construct an isotropic structure with identical building blocks. Unwanted swirl effects may be induced by the particular arrangement of channels within a single RRUC. It is therefore necessary to consider the average behaviour of several RRUC's, each with different directional changes. Conceptually, this implies that it may be necessary to consider results from two complimentary RRUC's in the case of a two-dimensional porous medium and four in the case of a three-dimensional porous medium.

4.2 Construction of an RRUC

When constructing an RRUC, one of the primary features to consider is the connectivity and geometric character of the porous material, as described in sections 2.2.1 and 2.2.4 respectively. In this regard, distinctions have been made between foam-like materials, granular materials and prismatic bundles for construction of RRUC's and are summarised by Du Plessis and Diedericks (1997).

The volume of the solid material inside an RRUC should be chosen in such a manner that the porosity of the RRUC is consistent with the porosity of the porous medium. The solid material inside the RRUC should reflect the basic geometric features of the original porous matrix. Another important feature of the porous medium that should be included in the RRUC is the correct fluid-solid surface areas for the various flow directions.

Figure 4.1 illustrates a schematic representation of an appropriate RRUC for a prismatic bundle that was introduced by du Plessis (1991). Due to the isotropy requirements, both the volume of the RRUC U_0 and the solid constituent U_s are square prisms. The position of the solid constituent in the RRUC is not restricted to the center of the RRUC and may be varied to be representative of the porous medium. Here d represents the characteristic length of the original porous medium and the dimension of the RRUC. The length of the prismatic bundle is denoted by L and may be extended into infinity to reduce the analysis

of the porous medium to two dimensions when considering cross-flow through the bundle.

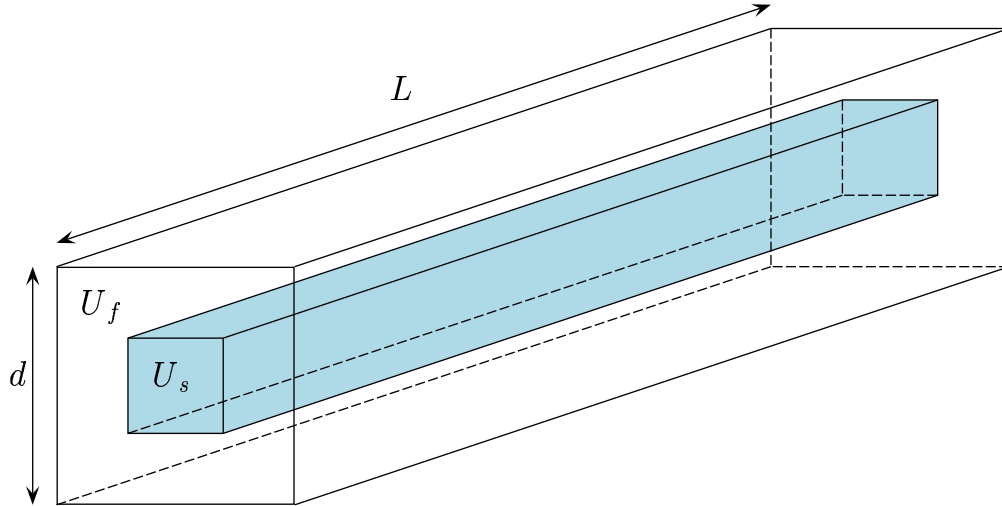


Figure 4.1: A Rectangular Representative Unit Cell for prismatic bundles.

4.3 Two-dimensional RRUC geometry modelling

A distinction is made between mainly two types of staggered configurations, namely non-staggered and staggered, as previously discussed in section 2.3.4. This section will cover the geometric part of the pore-scale modelling procedure for both staggered and non-staggered configurations of the two-dimensional representation of the RRUC for a prismatic bundle. The configurations of the RRUC's in this text corresponds to those of Firdaouss and Du Plessis (2004).

4.3.1 Definition of volumes

The RRUC model rely on the distinction of different volumes used for fluid transport. The different volumes may formally be defined as follows: U_0 is the total volume of the RRUC including all fluid U_f and solid U_s volumes, such that

$$U_0 = U_f + U_s. \quad (4.1)$$

CHAPTER 4. THE RECTANGULAR REPRESENTATIVE UNIT CELL

The fluid volume U_f is divided into four parts: The stream-wise volume, $U_{||}$, which contributes to the flow in the stream-wise direction and experience wall shear stress effects; the perpendicular volume, U_{\perp} , which contributes to the flow in the perpendicular direction and experience wall shear stress effects; the transfer volume, U_t , where the moving fluid experiences no wall shear stress effects and the stagnant volume, U_g , where the fluid is stagnant. The following relationship holds for the fluid volume

$$\mathcal{U}_f = U_{||} + U_{\perp} + U_t + U_g. \quad (4.2)$$

The above relationships and definitions hold for both the staggered and the non-staggered configurations.

4.3.2 Non-staggered RRUC configuration

Figure 4.2 shows a two-dimensional non-staggered configuration of an RRUC. In this case it may be assumed that the fluid moves only in the stream-wise direction. This means that there are no perpendicular stream-wise volumes U_{\perp} , but there do exist stagnant volumes between the solids. A transfer volume where no wall shear stresses occur may also be noted to exist as depicted in the figure. Table 4.1 lists the volumes for the non-staggered configuration in terms of the lengths shown in Figure 4.2.

U_0	d^2
U_s	d_s^2
U_f	$d^2 - d_s^2$
$U_{ }$	$d_s(d - d_s)$
U_t	$(d - d_s)^2$
U_g	$d_s(d - d_s)$

Table 4.1: Expressions for volumes in a non-staggered configuration.

4.3.3 Staggered RRUC configuration

Figure 4.3 shows a two-dimensional staggered configuration of an RRUC. If piecewise straight streamlines are assumed, the configuration of the different volumes may be taken

CHAPTER 4. THE RECTANGULAR REPRESENTATIVE UNIT CELL

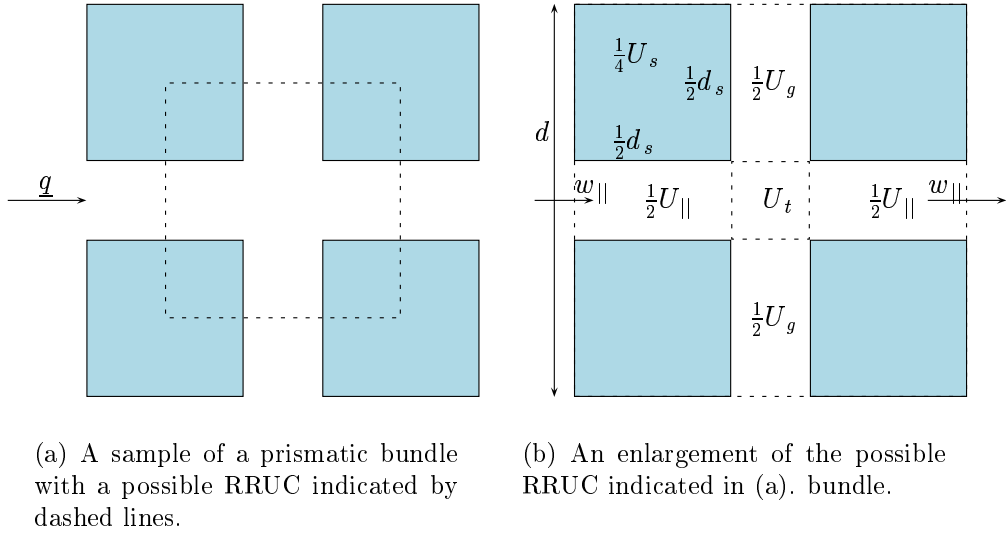


Figure 4.2: Non-staggered configuration of an RRUC.

as illustrated in Figure 4.3. Note that in the staggered configuration the fluid does move in a direction perpendicular to the stream-wise direction and the perpendicular volumes U_{\perp} exist. Although not as obvious as in the staggered case, the fluid volume also includes volumes where there are no shear stresses acting on the fluid, U_t . The fluid traverses all available volumes and there are no regions where the fluid is stagnant.

U_0	d^2
U_s	d_s^2
U_f	$d^2 - d_s^2$
U_{\parallel}	$d_s(d - d_s)$
U_t	$(d - d_s)^2$
U_{\perp}	$d_s(d - d_s)$

Table 4.2: Expressions for volumes in a staggered configuration.

The different volumes may be expressed in terms of the lengths given in Figure 4.3 and are listed in Table 4.2. It should be noted that for the RRUC configurations represented in Figure 4.2 and Figure 4.3, there is no need to consider complimentary RRUC's to avoid swirl effects, as discussed in section 4.1, because of the symmetry of the RRUC in the vertical direction.

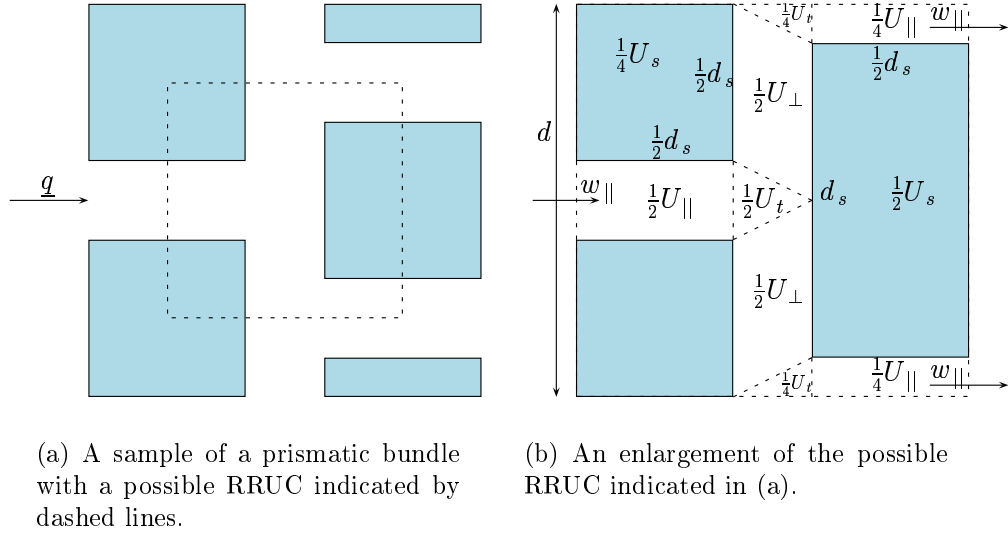


Figure 4.3: A staggered configuration of an RRUC.

4.3.4 Tortuosity

In this section the concept of tortuosity, which was discussed in general in section 3.7.2, is applied to the RRUC geometry. Figure 4.4 illustrates the assumption of piecewise straight streamlines between, and parallel to, the rectangular solid blocks.

We use the basic definition of tortuosity as discussed in section 3.7.2, which is based on the path lengths of the fluid particles and defined as the ratio of the average length of the tortuous flow path L_e to the straight displacement length L in the stream-wise direction, as shown in (3.28) to be

$$\chi = \frac{L_e}{L}. \quad (4.3)$$

According to the rectangular geometry and associated assumptions the streamlines inside the RRUC is of equal length L_e . The length of the tortuous path of the staggered configuration may be expressed as $L_e = d + \frac{d_s}{2}$, while for the non-staggered configurations the tortuous length is simply $L_e = d$. The straight displacement length in both configurations is $L = d$.

CHAPTER 4. THE RECTANGULAR REPRESENTATIVE UNIT CELL

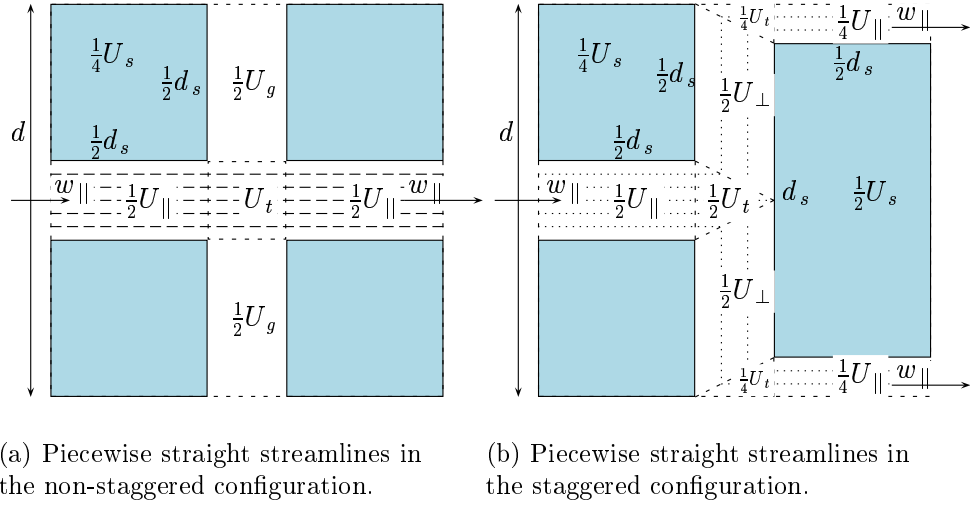


Figure 4.4: Piecewise straight streamlines represented in a two-dimensional RRUC for the staggered and non-staggered cases.

In terms of the defined volumes, the tortuosity for the staggered configuration may be given as

$$\chi = \frac{\frac{1}{2}U_{\parallel} + \frac{1}{4}U_{\perp} + \frac{1}{2}U_t}{\frac{1}{2}U_{\parallel} + \frac{1}{2}U_t} = \frac{U_{\parallel} + U_t + \frac{1}{2}U_{\perp}}{U_{\parallel} + U_t}, \quad (4.4)$$

and in the case of the non-staggered configuration

$$\chi = 1. \quad (4.5)$$

Equation (4.4) is obtained through considering only one of the symmetry planes inside the staggered configuration shown in Figure 4.4 (b). It should be noted that only half of the U_{\perp} volume should be taken into account because the fluid is travelling at half the speed in this section.

These two cases may be combined into a single equation in the following way

$$\chi = 1 + \frac{\beta U_{\perp}}{U_{\parallel} + U_t}, \quad (4.6)$$

CHAPTER 4. THE RECTANGULAR REPRESENTATIVE UNIT CELL

where β is the fluid velocity ratio of the average velocity in the transverse channels to the average velocity in the stream-wise channels, defined as $w_{\perp} = \beta w_{\parallel}$. Thus, in the staggered case $\beta = 1/2$ and in the non-staggered case $\beta = 0$ (Lloyd et al., 2004).

The solid side length d_s may be written in terms of the microscopic characteristic length d and the porosity ϵ as follows

$$d_s = d\sqrt{1 - \epsilon}. \quad (4.7)$$

With the use of Table 4.2 and Table 4.1, the following expression for the tortuosity may be obtained in terms of the porosity

$$\chi = 1 + \beta\sqrt{1 - \epsilon}. \quad (4.8)$$

Figure 4.5 illustrates how the tortuosity varies with a change in porosity for both the staggered and non-staggered cases.

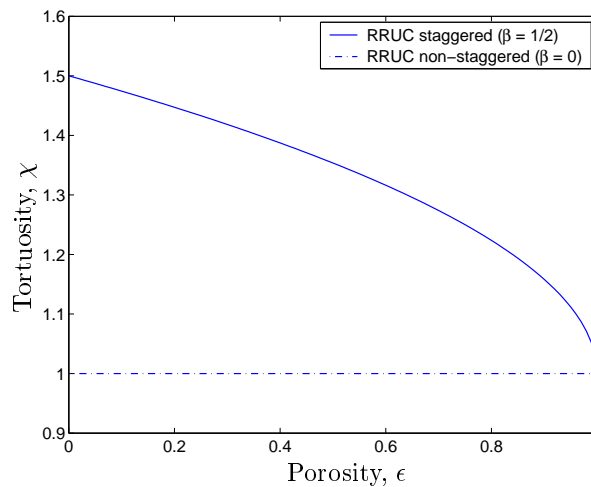


Figure 4.5: Tortuosity of staggered and non-staggered configurations.

4.4 Interstitial pressure modelling

This section is concerned with the modelling of the pressure surface integral of the macroscopic momentum equation for uniform discharge through a homogeneous isotropic porous medium as found in (3.65). The aim of this section is to present a short summary of the latest modelling procedure presented by Lloyd. For details on the calculations the reader is referred to Lloyd (2003) and Lloyd et al. (2004).

The phase average of the pressure gradient may be written as follows

$$\langle \nabla p \rangle = \nabla \langle p \rangle + \frac{1}{U_0} \iint_{S_{fs}} \underline{n} p dS. \quad (4.9)$$

This equation is analysed to aid finding an expression for the surface pressure integral in terms of measurable parameters.

4.4.1 Non-staggered configuration

Each term in (4.9) will be investigated separately, in order to find possible relationships between the various terms. Therefore an expression for each term is calculated in terms of the symbolic parameters shown in Figure 4.6. Note that although the position of the solid phase in Figure 4.6 differs from that of Figure 4.4 (b), it is still conceptually the same in terms of representation of the porous medium and flow paths. Although the chosen RRUC is of minimal size and have the same geometric characteristics as the porous medium, it is not representative of the porous medium, as will be discussed in the next subsection. Therefore, two separate cases need to be considered.

RRUC's that cut through the solid

Figure 4.6 graphically shows two neighbouring unit cells for the non-staggered configuration where the boundaries in the perpendicular direction of the unit cell runs through the solid region. It is assumed that the pressure in the stagnant regions U_g is constant and that there is no pressure loss across the transfer volumes U_t . In addition, a constant pressure gradient is assumed over $U_{||}$. The pressure at the different sections of the RRUC is indicated at

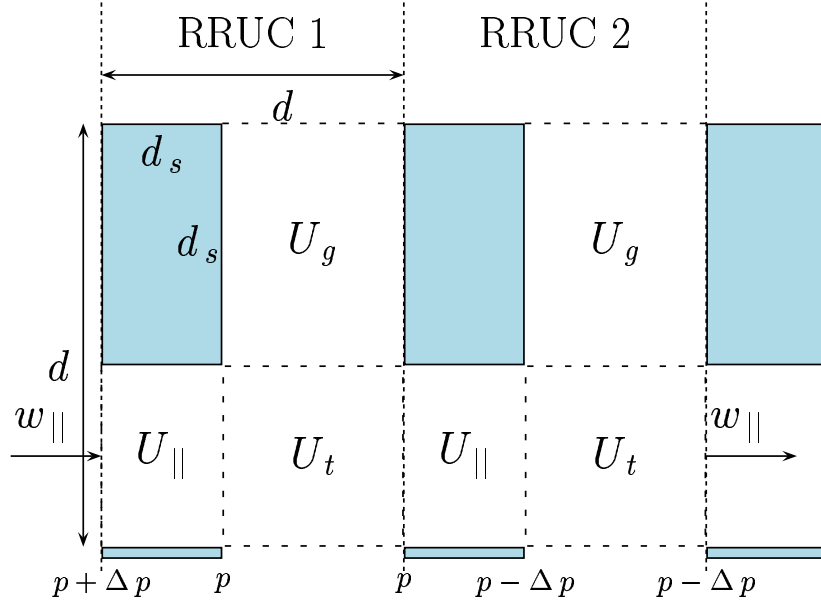


Figure 4.6: Pressure distributions in non-staggered RRUC geometry where the RRUC boundary cuts the solid constituent (The squareness of the RRUC is suppressed for clarity).

the bottom of the figure. With the mentioned assumptions in mind the first term in (4.9) yields

$$\langle \nabla p \rangle = \frac{1}{U_0} \iiint_{U_{||}} \nabla p dU = -\frac{U_{||} \Delta p}{U_0 d_s}.$$

The gradient of the average pressure gradient between two adjacent RRUC's is taken to calculate the second term in (4.9), and yields

$$\begin{aligned} \nabla \langle p \rangle &= \frac{1}{U_0} \left(\iiint_{U_f(RRUC2)} p dU - \iiint_{U_f(RRUC1)} p dU \right) / d \\ &= \frac{1}{U_0} \left(\left[(p - \frac{\Delta p}{2}) U_{||} + (p - \Delta p) U_t + (p - \Delta p) U_g \right] \right. \\ &\quad \left. - \left[(p + \frac{\Delta p}{2}) U_{||} + p U_t + p U_g \right] \right) \frac{1}{d} \\ &= -\frac{U_f \Delta p}{U_0 d}. \end{aligned} \tag{4.10}$$

CHAPTER 4. THE RECTANGULAR REPRESENTATIVE UNIT CELL

The third term in (4.9) is zero since the pressure in U_g is assumed uniform and the pressure on the walls will therefore cancel, giving

$$\frac{1}{U_0} \iint_{S_{fs}} \underline{n} p dS = 0. \quad (4.11)$$

RRUC's that do not cut through the solid

If the RRUC is shifted downstream in such a manner that the perpendicular boundaries do not pass through the solid regions, as shown in Figure 4.7, the surface integral term of (4.9) will not be zero.

As in the case where the RRUC boundaries cut through the solid parts, the first term of (4.9) will be exactly the same as (4.10), that is

$$\langle \nabla p \rangle = -\frac{U_{\parallel}}{U_0} \frac{\Delta p}{d_s}, \quad (4.12)$$

since the pressure is assumed to be constant in both the transfer and stagnant volumes.

We consider an adjacent RRUC, similar to the one shown in Figure 4.7, and take the gradient of their two pressure averages to compute the second term of (4.9) in the following way

$$\nabla \langle p \rangle = -\frac{U_f}{U_0} \frac{\Delta p}{d_s}. \quad (4.13)$$

This can be shown by considering that each component of the fluid volume pressure averages, of the neighbouring RRUC's that cut the fluid phases, differ by Δp .

For this RRUC arrangement, the third term in (4.9) may be given by

$$\begin{aligned} \frac{1}{U_0} \iint_{S_{fs}} \underline{n} p dS &= \frac{1}{U_0} (p d_s - (p - \Delta p) d_s) \\ &= \frac{d_s}{U_0} (\Delta p). \end{aligned} \quad (4.14)$$

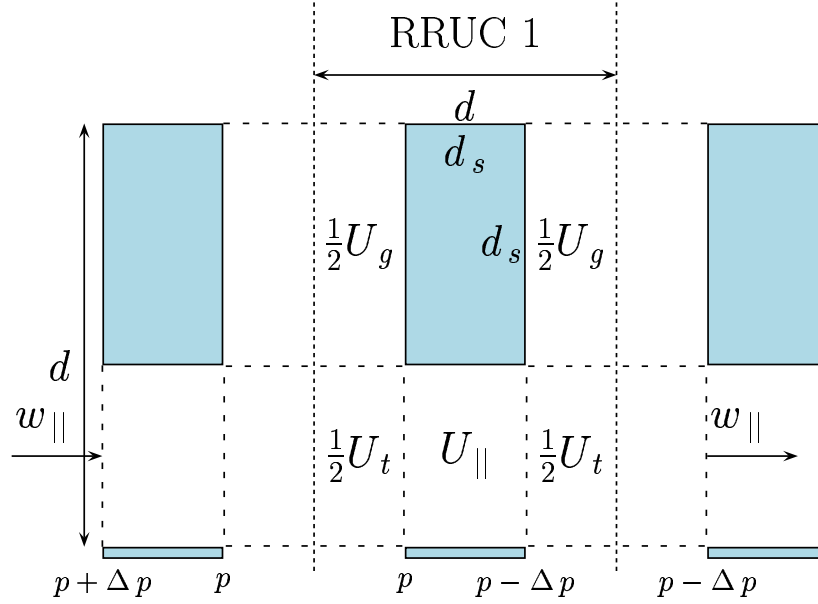


Figure 4.7: Pressure distributions in non-staggered RRUC geometry where the RRUC boundary cuts the fluid phase. (The squareness of the RRUC is suppressed for clarity.)

The combined expression for the pressure surface integral

The two scenarios mentioned above should be added, but weighed according to their relative frequency of occurrence, to obtain an expression based on RRUC modelling that is representative of the porous medium. The relative frequency of occurrence of the RRUC that cuts through the solid is given by $\frac{d_s}{d}$, while the relative frequency of occurrence of the RRUC that cuts through the fluid may be given by $\frac{d-d_s}{d}$. Equations (4.10) to (4.11) may be combined with equations (4.12) to (4.14) with their relative frequency of occurrence to yield an expression for (4.9) that is valid in general for the non-staggered configuration:

$$\langle \nabla p \rangle = -\frac{U_{||}}{U_0} \frac{\Delta p}{d_s}, \quad (4.15)$$

$$\nabla \langle p \rangle = -\frac{U_f}{U_0} \frac{\Delta p}{d}, \quad (4.16)$$

$$\frac{1}{U_0} \iint_{S_{fs}} \underline{n} p dS = \frac{(d-d_s)}{d} \frac{d_s}{U_0} (\Delta p). \quad (4.17)$$

A few algebraic steps may be used to verify that

$$-\frac{U_{\parallel}}{U_0} \frac{\Delta p}{d_s} = -\frac{U_f}{U_0} \frac{\Delta p}{d} + \frac{(d - d_s)}{d} \frac{d_s}{U_0} (\Delta p). \quad (4.18)$$

Some more algebra may be used to rewrite (4.15) as

$$\langle \nabla p \rangle = - \left(\frac{U_{\parallel} + U_t}{U_0} \right) \frac{\Delta p}{d}, \quad (4.19)$$

since $U_g = U_{\parallel}$ for the non-staggered arrangement. Equations (4.19) and (4.16) may now be combined to form the relationship

$$\langle \nabla p \rangle = \left(\frac{U_{\parallel} + U_t}{U_f} \right) \nabla \langle p \rangle. \quad (4.20)$$

By substituting (4.20) into (4.9) the following expression for the pressure surface integral is obtained in terms of the gradient of the phase average of the pressure

$$\frac{1}{U_0} \iint_{S_{fs}} \underline{n} p dS = \left(\frac{U_{\parallel} + U_t}{U_f} - 1 \right) \nabla \langle p \rangle. \quad (4.21)$$

4.4.2 Staggered configuration

As in the previous section, each term in (4.9) will be investigated separately, in order to find possible relationships between the various terms. To do so, an expression for each term is calculated in terms of the symbolic parameters shown in Figure 4.8. Although the chosen RRUC is of minimal size and have the geometric characteristics, it is not representative of the porous medium. Therefore, two separate cases need to be considered. It may be assumed that the pressure is uniform and constant in the transfer regions and a linear pressure drop prevails in the flow channels in the stream-wise direction.

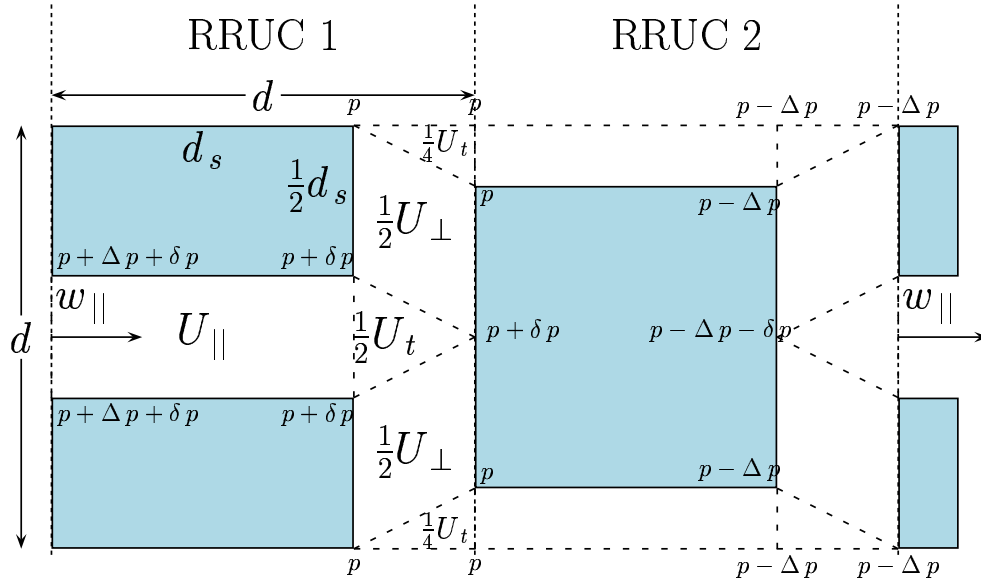


Figure 4.8: Pressure distributions in the staggered RRUC geometry where the RRUC boundary cuts the solid constituent.

RRUC's that cut through the solid

Consider a unit cell where the boundaries in the perpendicular direction of the unit cell cuts through the solid region, as illustrated in Figure 4.8. Here Δp denotes the total pressure drop in the stream-wise direction and δp the pressure drop in the transverse channels. In terms of the symbols defined, the first term in (4.9) may be written as

$$\begin{aligned}
 \langle \nabla p \rangle &= \frac{1}{U_0} \left(\iiint_{U_{\parallel}} \nabla p dU + \iiint_{U_{\perp}} \nabla p dU \right) \\
 &= \frac{1}{U_0} \left(-\frac{\Delta p}{d_s} U_{\parallel} + \frac{-(d - d_s)/d_s \delta p}{d - d_s} U_{\perp} \right) \\
 &= -\frac{U_{\parallel}}{U_0} \left(\frac{\Delta p + \delta p}{d_s} \right). \tag{4.22}
 \end{aligned}$$

This expression was obtained by assuming no pressure gradient in the transfer volumes, and linear pressure gradients in the channels. The second term on the right hand side denotes the pressure gradient in the stream-wise direction of the transverse volumes.

 CHAPTER 4. THE RECTANGULAR REPRESENTATIVE UNIT CELL

In analogy to the previous section, the second integral in (4.9) may be written as

$$\begin{aligned}
 \nabla \langle p \rangle &= \frac{1}{U_0} \nabla \iiint_{U_f} p dU \\
 &= \frac{1}{U_0} \left(\left[(p - \frac{\Delta p}{2}) U_{\parallel} + (p - \Delta p - \frac{\delta p}{2}) U_t + (p - \Delta p - \frac{\delta p}{2}) U_{\perp} \right] \right. \\
 &\quad \left. - \left[(p + \delta p + \frac{\Delta p}{2}) U_{\parallel} + (p + \frac{\delta p}{2}) U_t + (p + \frac{\delta p}{2}) U_{\perp} \right] \right) / d \\
 &= -\frac{U_f}{U_0} \left(\frac{\Delta p + \delta p}{d} \right). \tag{4.23}
 \end{aligned}$$

In this case the surface integral is zero

$$\frac{1}{U_0} \iint_{S_{fs}} \underline{n} p dS = 0, \tag{4.24}$$

since the pressures at the walls are assumed equal and therefore cancel.

RRUC's that do not cut through the solid

The unit cell may be shifted in the stream-wise direction so that the boundaries do not pass through the solid region, as illustrated in Figure 4.9. In this case the surface integral of (4.9) will not be zero.

The pressure is assumed to be constant in the transfer volumes so that the pressure gradient will be zero in these volumes. There is a pressure gradient in the transverse volumes in the stream-wise direction and if it is assumed that the gradient is linear, the first term in (4.9) may be written as

$$\begin{aligned}
 \langle \nabla p \rangle &= \frac{1}{U_0} \left(\frac{-\Delta p}{d_s} U_{\parallel} + \frac{p - [p + \frac{d-d_s}{2d_s} \delta p]}{(d-d_s)/2} \frac{U_{\perp}}{2} + \frac{[p - \Delta p - \frac{d-d_s}{2d_s} \delta p] - [p - \Delta p]}{(d-d_s)/2} \frac{U_{\perp}}{2} \right) \\
 &= -\frac{U_{\parallel}}{U_0} \left(\frac{\Delta p + \delta p}{d_s} \right). \tag{4.25}
 \end{aligned}$$

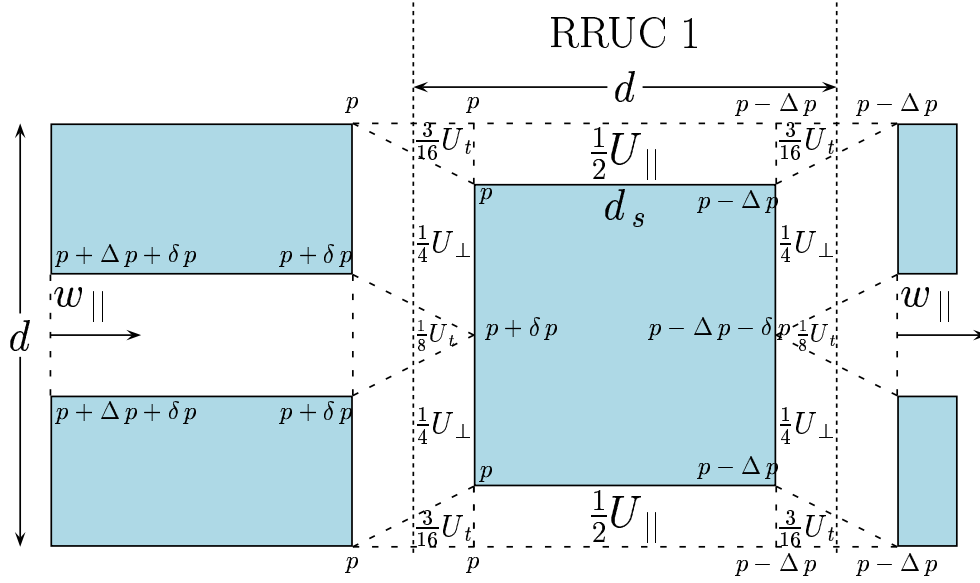


Figure 4.9: Pressure distributions in the staggered RRUC geometry where the RRUC boundary cuts only the fluid phase.

The second term in (4.9) may be written as

$$\begin{aligned}
 \nabla \langle p \rangle &= \frac{1}{U_0} \nabla \iiint_{U_f} p dU \\
 &= -\frac{1}{U_0} \left(\frac{((\Delta p + \delta p)U_{||} + (\Delta p + \delta p)U_t + (\Delta p + \delta p)U_{\perp})}{d_s} \right) \\
 &= -\frac{U_f}{U_0} \left(\frac{\Delta p + \delta p}{d} \right). \tag{4.26}
 \end{aligned}$$

This expression was obtained by considering two similar neighbouring unit cells and realising that each of the volume components differ by $(\Delta p + \delta p)$.

The surface integral is given by

$$\begin{aligned}
 \frac{1}{U_0} \iint_{S_{fs}} \underline{n} p dS &= \frac{1}{U_0} \left(\frac{p + (p + \delta p)}{2} d_s - \frac{(p - \Delta p) + (p - \Delta p - \delta p)}{2} d_s \right) \\
 &= \frac{d_s}{U_0} (\Delta p + \delta p). \tag{4.27}
 \end{aligned}$$

The combined expression for the pressure surface integral

The two scenarios mentioned above should be weighed according to their relative frequency of occurrence, to obtain an expression based on RRUC modelling that is representative of the porous medium. In the same manner as with the previous section, equations (4.22) to (4.24) may be combined with equations (4.25) to (4.27) with their relative frequency of occurrence to yield

$$\langle \nabla p \rangle = -\frac{U_{\parallel}}{U_0} \left(\frac{\Delta p + \delta p}{d_s} \right) \quad (4.28)$$

$$\nabla \langle p \rangle = -\frac{U_f}{U_0} \left(\frac{\Delta p + \delta p}{d} \right) \quad (4.29)$$

$$\frac{1}{U_0} \iiint_{S_{fs}} \underline{n} p \, dS = \frac{(d - d_s)}{d} \frac{d_s}{U_0} (\Delta p + \delta p). \quad (4.30)$$

The same procedure followed in the non-staggered configuration may be applied to the staggered configuration to yield the following expression for the surface integral

$$\frac{1}{U_0} \iint_{S_{fs}} \underline{n} p \, dS = \left(\frac{U_{\parallel} + U_t}{U_f} - 1 \right) \nabla \langle p \rangle. \quad (4.31)$$

This equation is the same as (4.21) and is therefore appropriate for staggered and non-staggered configurations of the RRUC's.

4.5 Interstitial flow modelling

In this section a general closure procedure for the momentum transport equation

$$-\epsilon \nabla P_f = \frac{1}{U_0} \iint_{S_{fs}} (\underline{n} \{p\} - \underline{n} \cdot \underline{\tau}) \, dS, \quad (4.32)$$

in both the Darcy and the Forchheimer flow regimes, is presented.

4.5.1 The Reynolds number

The Reynolds number, Re , was first formulated by Osborne Reynolds in 1883 (Tokaty, 1971). He conducted experiments in pipe flows and revealed two modes of fluid flow, namely laminar and turbulent. The Reynolds number may be used as an indication of various flow regimes. Reynolds numbers are of great value in various fields of fluid mechanics, because they are comparable when they refer to geometrically similar flows.

The Reynolds number is a dimensionless parameter described by the magnitude of the ratio between the inertia and net viscous forces. The basic expression for the Reynolds number may be written as

$$Re = \frac{\rho l u}{\mu}, \quad (4.33)$$

where ρ is the fluid density, μ the dynamic viscosity of the fluid, u the particular representative velocity and l a characteristic length.

There are many different types of Reynolds numbers. They differ mostly on the particular choice of the characteristic length scale and fluid velocity. In channel flow, the hydraulic diameter is a popular choice for the characteristic length. In the case of flow between parallel plates the hydraulic diameter is defined as $d_h = 2d_p$, where d_p is the distance between the plates. An effective interstitial Reynolds number for the stream-wise flow between parallel plate sections may henceforth be defined as

$$Re_p = \frac{2 d_p \rho w}{\mu} = \frac{2 d \rho q}{\mu}. \quad (4.34)$$

This definition of the Reynolds number is used throughout this work in the RRUC modelling procedures.

4.5.2 The Darcy regime

The Darcy flow regime exists in the low Reynolds number limit ($\text{Re}_p \ll 1$), where the viscous forces dominate the inertial forces. A uniform discharge of a Newtonian fluid through a homogeneous isotropic porous medium is assumed for the RRUC modelling.

The wall shear stresses in the transverse pores have no stream-wise components when considering the staggered configuration. According to Lloyd (2003), the randomness of the medium causes the transverse shear stresses to cancel vectorially, but they effectively create transverse pressure drops. These pressure drops contribute to the macroscopic pressure loss through the pressure part of the surface integral in (4.32), when evaluated in the stream-wise direction.

The pressure term in (4.32) may be written in terms of (4.31). According to Lloyd the pressure term in (4.32) does not include the pressure drop in the transverse direction created by the transverse shear stresses and the surface integral of the shear stresses should be taken over the transverse pore sections as well. In the transverse regions the flow splits in two and therefore only half of the transverse part of S_\perp needs to be taken into account. Equation (4.32) may now be written as

$$-\epsilon \nabla P_f = \left(\frac{U_{\parallel} + U_t}{U_f} - 1 \right) \epsilon \nabla P_f - \frac{1}{U_0} \iint_{S_{\parallel}} (\underline{n} \cdot \underline{\tau}) dS + \frac{\hat{n}}{2U_0} \iint_{S_{\perp}} |\underline{n} \cdot \underline{\tau}| dS.$$

If the wall shear stress is assumed to be uniform and equal to a constant, τ_w , over S_{fs} in all channel sections for the low Reynolds number limit, the above equation may be reduced to

$$-\frac{\epsilon}{(1 + \sqrt{1 - \epsilon})} \nabla P_f = \frac{\hat{n}}{U_0} \iint_{S_{\parallel}} \tau_w dS + \frac{\hat{n}}{2U_0} \iint_{S_{\perp}} \tau_w dS, \quad (4.35)$$

by substitution of the values for the different volumes in Table 4.2. For Newtonian flow between two parallel plates a distance $(d - d_s)$ apart, $\tau_w = \frac{6\mu w_{\parallel}}{d - d_s}$. The average transverse pore velocity is given by βw_{\parallel} , where β is the velocity ratio. This allows the following

 CHAPTER 4. THE RECTANGULAR REPRESENTATIVE UNIT CELL

simplification

$$-\frac{\epsilon}{(1 + \sqrt{1 - \epsilon})} \nabla P_f = \left(\frac{S_{\parallel} + \frac{\beta}{2} S_{\perp}}{U_0} \right) \left(\frac{6\mu w_{\parallel}}{(d - d_s)} \right) \hat{n}. \quad (4.36)$$

The continuity equation may be used to express w_{\parallel} in terms of the superficial velocity q as follows

$$w_{\parallel} = \frac{U_0}{U_{\parallel} + U_t} q = \frac{1}{1 - \sqrt{1 - \epsilon}} q \quad (4.37)$$

in the stream-wise direction. In the case of the unidirectional fibre bed, the solid surfaces and lengths may be given by $S_{\parallel} = S_{\perp} = 2d\sqrt{1 - \epsilon}$ and $d_s = d\sqrt{1 - \epsilon}$, respectively. By substituting these expressions in (4.36), the following general expression for the pressure drop across a unidirectional fibre bed may be obtained for the low Reynolds number limit

$$-\epsilon \nabla P_f = G_0 \mu \underline{q}, \quad (4.38)$$

where

$$G_0 = \frac{12(1 + \frac{\beta}{2}) \epsilon \sqrt{1 - \epsilon}}{d^2 (1 - \sqrt{1 - \epsilon})^3}. \quad (4.39)$$

This expression is valid for both the staggered ($\beta = \frac{1}{2}$) and non-staggered configurations ($\beta = 0$) in the low Reynolds number limit. The dimensionless hydrodynamic permeability may be expressed as

$$\begin{aligned} K &= \frac{\epsilon}{G_0 d^2} \\ &= \frac{(1 - \sqrt{1 - \epsilon})^3}{12(1 + \frac{\beta}{2}) \sqrt{1 - \epsilon}}. \end{aligned} \quad (4.40)$$

4.5.3 The Forchheimer regime

In practical applications of flow through porous media the flow is not restricted to the Darcy regime. It is considered that for intermediate Reynolds number flow, the interstitial drag forces predominate the viscous forces and microscopic recirculation zones occur without the presence of turbulence (Ruth and Ma, 1992). A consequence of the above scenario is a non-linear relationship between the macroscopic pressure gradient and the superficial velocity.

The interstitial modelling of the inertial flow regime with an RRUC assumes the following:

- viscous effects may be neglected, therefore
$$\iint_{S_{fs}} \underline{n} \cdot \underline{\tau} = \underline{0},$$
- the dominant inertial effects cause a recirculation zone downstream of the solid material,
- and the flow recirculates symmetrically around the solid.

Equation (4.32) may therefore be written as

$$\begin{aligned} -\epsilon U_0 \nabla P_f &= \iint_{S_{fs}} (\underline{n}p - \underline{n} \cdot \underline{\tau}) dS \\ &= \iint_{S_{\perp}^{(d)}} \underline{n}p dS + \iint_{S_{\perp}^{(u)}} \underline{n}p dS, \end{aligned} \quad (4.41)$$

where $S_{\perp}^{(u)}$ and $S_{\perp}^{(d)}$ represents the upstream and downstream parts of S_{\perp} respectively and the pressure on S_{\parallel} cancels due to symmetry. Therefore, only the pressure difference on the opposing solid surfaces perpendicular to the stream-wise direction is required for prediction of the macroscopic pressure drop over a porous medium subject to intermediate Reynolds number flow. In this section two existing RRUC models to obtain the pressure difference are discussed.

Figure 4.10 gives a schematic representation of the interstitial recirculation in the upper half of an RRUC. The dividing streamline which separates the recirculation zone from the bulk flow has a stagnation point on the upstream part of S_{\perp} as indicated by point *a*. This

CHAPTER 4. THE RECTANGULAR REPRESENTATIVE UNIT CELL

streamline also has an inflection point downstream of the solid at point c in Figure 4.10. Following the Kirchoff free streamline model, as used by Smith (1997), the free streamline divides a region of vanishing velocity and constant pressure from a region of non-rotational flow. The pressure in the recirculation zone is then assumed to be constant and equal to the pressure at the inflection point c and therefore also the pressure on $S_{\perp}^{(d)}$, indicated by point b in Figure 4.10.

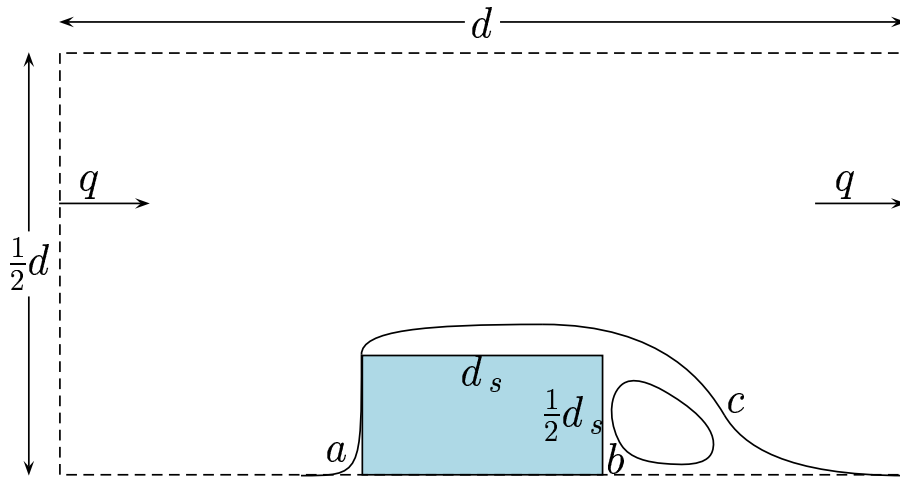


Figure 4.10: A two-dimensional schematic representation of interstitial flow recirculation in an upper half of an RRUC.

Model 1

It is assumed that the pressure on the upstream side of the solid is uniform across the surface and equal to the value, p_a , at the stagnation point, therefore

$$\iint_{S_{\perp}^{(u)}} \underline{n} p dS = p_a S_{\perp}^{(u)} \underline{n}. \quad (4.42)$$

According to Du Plessis (1994), the pressure on the downstream surface of the solid may be obtained by applying the Bernoulli equation along the dividing streamline from the

CHAPTER 4. THE RECTANGULAR REPRESENTATIVE UNIT CELL

stagnation point at a to the inflection point of the streamline at c . This yields

$$\frac{\rho}{2} v_a^2 + \Omega_a + p_a = \frac{\rho}{2} v_c^2 + \Omega_c + p_c, \quad (4.43)$$

where v_a and v_c are the respective fluid velocities on the streamline at points a and c , p_a and p_c are the local pressures at points a and c , respectively and Ω_a and Ω_b are potential functions related to the body forces acting on the fluid at a and c , respectively. For horizontal flow the body forces are uniform at all points on the streamline and the fluid is stationary at the stagnation point. Equation (4.43) may now be written as

$$p_a = \frac{\rho}{2} v_c^2 + p_c. \quad (4.44)$$

If it is assumed that the pressure is uniformly distributed over the downstream face of the solid then

$$\begin{aligned} \iint_{S_{\perp}^{(d)}} \underline{n} p dS &= -p_c S_{\perp}^{(d)} \underline{n} \\ &= \left(\frac{\rho}{2} v_c^2 - p_a \right) S_{\perp}^{(d)} \underline{n}. \end{aligned} \quad (4.45)$$

Equation (4.42) and (4.45) may now be substituted into (4.41) to yield

$$-\epsilon U_0 \nabla P_f = \frac{\rho}{2} v_c^2 S_{\perp}^{(d)} \underline{n}. \quad (4.46)$$

The velocity at the inflection point is still unknown, and a modelling choice is to be made to approximate v_c . Since the inflection point is not directly in the stream-wise channel, the magnitude of v_c may be nearly equal to w_{\perp} . An appropriate asymptotic value for the magnitude of v_c may be given by

$$v_c \approx w_{\perp} = \beta w_{\parallel}. \quad (4.47)$$

By substituting (4.37) and (4.47) into (4.46), an expression for the macroscopic pressure

CHAPTER 4. THE RECTANGULAR REPRESENTATIVE UNIT CELL

drop in the intermediate Reynolds number regime may be obtained as

$$-\epsilon \nabla P_f = G_\infty \mu \underline{q}, \quad (4.48)$$

with

$$G_\infty = \frac{\rho \sqrt{1-\epsilon} \beta^2 q}{2 d \mu (1 - \sqrt{1-\epsilon})^2}. \quad (4.49)$$

Model 2

An alternative, less complicated approximation of the pressure integral may be accomplished by applying the definition of pressure drag. This could be done by noting that the recirculation and corresponding momentum loss are effectively pressure drag processes. In general, the pressure drag is related to the square of a free stream velocity v_∞ , from which it then follows that

$$\begin{aligned} -\epsilon U_0 \nabla P_f &= \iint_{S_{fs}} \underline{n} p dS \\ &= \frac{\rho}{2} c_d v_\infty^2 S_\perp^{(u)} \underline{n}. \end{aligned} \quad (4.50)$$

Here $\frac{\rho}{2} v_\infty^2$ is a kinetic energy term appearing in the definition of pressure drag, while c_d is the drag coefficient or friction factor (Munson et al., 1999). Different values may be selected for c_d , depending on the shape of the solid material within the RRUC. Experimental evidence shows that the drag coefficient for flow past a square bar is approximately 2.2 (Munson et al., 1999). However, Du Plessis and Van Der Westhuizen (1993) proposed a value between 0.5 and 1 for cross-flow in a fibre bed.

The stream-wise channel average velocity may be selected as the free stream velocity, that is $v_\infty \approx w_{||}$. Substitution of this expression into (4.50) yields the following expression for the macroscopic pressure drop for intermediate Reynolds number flow in a prismatic bundle

$$-\epsilon \nabla P_f = G_\infty \mu \underline{q}, \quad (4.51)$$

with

$$G_{\infty} = \frac{\rho \sqrt{1 - \epsilon} c_d q}{2 d \mu (1 - \sqrt{1 - \epsilon})^2}. \quad (4.52)$$

These models differ by the appearance of c_d and β in the final expressions. Equations (4.49) and (4.52) may be considered equivalent if c_d and β^2 both serve as approximation coefficients for the velocity around the solid structure. The first model has the benefit that β could be computed directly from the geometry of the porous medium, while the second model has the advantage that the drag coefficient could be adapted for constituents that differs substantially from a square bar.

4.5.4 General momentum transport

An asymptote matching technique (Churchill and Usagi, 1972) is applied to obtain a general expression for the pressure drop over a fibre bed that is valid for the entire range of Reynolds numbers in the laminar flow regime. The total frictional effect of the solid matrix on the traversing fluid may be modelled by

$$G = [G_0^s + G_{\infty}^s]^{1/s} \quad (4.53)$$

where s is a fitting parameter. This parameter determines the extent of overlap between the two physical conditions expressed by G_0 and G_{∞} . A value of unity was proposed by Du Plessis (1994), as it correlated well with the Ergun equation as well as with experimental results.

A general expression for predicting the pressure drop across a unidirectional fibre bed may finally be given as

$$-\epsilon \nabla P_f = G \mu \underline{q} \quad (4.54)$$

CHAPTER 4. THE RECTANGULAR REPRESENTATIVE UNIT CELL

with $G = G_0 + G_\infty$ and

$$G_0 = \frac{12(1 + \frac{\beta}{2}) \epsilon \sqrt{1 - \epsilon}}{d^2 (1 - \sqrt{1 - \epsilon})^3} \quad (4.55)$$

and

$$G_\infty = \frac{\rho \sqrt{1 - \epsilon} c_d q}{2 d \mu (1 - \sqrt{1 - \epsilon})^2}. \quad (4.56)$$

According to Bird et al. (1960), steadily driven flow of a fluid of constant density may be considered as flow in a straight conduit of uniform cross section, or fluid flow around a submerged object that has an axis of symmetry. For both these types of systems they state that the magnitude of the force on the solid due to the kinetic behaviour of the fluid, F_k , is proportional to a characteristic area, A_c , and a characteristic kinetic energy, E_k , in the following manner

$$F_k = A_c E_k \lambda, \quad (4.57)$$

where the proportionality constant λ is called the friction factor. The friction factor λ is not defined until A_c and E_k are specified. Generally, the measured quantity for the driving force is the pressure difference. For flow in conduits, A_c is usually taken to be the wetted surface and E_k is taken to be $\frac{1}{2} \rho q^2$. A parallel plate configuration is used in the RRUC modelling procedure and an applicable friction factor to simplify analysis of the transport equation may therefore be defined as

$$\lambda = \frac{dP_f}{dx} \frac{d}{2 \rho q^2} = \frac{dP_f}{dx} \frac{2 d^2 \rho}{\mu^2 \text{Re}_p^2}, \quad (4.58)$$

where $\frac{dP_f}{dx}$ is the pressure gradient in the stream-wise direction, ρ the fluid density and q the superficial velocity in the stream-wise direction. Equation (4.54) may be written in dimensionless form in terms of the defined friction factor λ and particle Reynolds number

CHAPTER 4. THE RECTANGULAR REPRESENTATIVE UNIT CELL

Re_p

$$-\lambda Re_p = \frac{G' - 1}{\epsilon Re_p}, \quad (4.59)$$

where $G' = G'_0 + G'_\infty$ with

$$G'_0 = \frac{12(1 + \frac{\beta}{2})\epsilon\sqrt{1-\epsilon}}{(1 - \sqrt{1-\epsilon})^3} \quad (4.60)$$

and

$$G'_\infty = \frac{\sqrt{1-\epsilon} c_d}{4(1 - \sqrt{1-\epsilon})^2} Re_p. \quad (4.61)$$

In this chapter the RRUC has been presented. Expressions for the pressure gradient in the Darcy and Forchheimer regimes have been discussed. These expressions will be referred to in the next chapters when the various modelling assumptions are analysed.

Chapter 5

Numerical investigations

This chapter is concerned with numerical investigations of the reasons for and the existence of a transition in the flow from the Darcy regime to the Forchheimer regime. The validity of the assumptions made in the previous chapter through the RRUC modelling procedure are also tested using the commercial CFD code FLUENT.

5.1 Numerical procedures

The commercial computational fluid dynamics code FLUENT was used to perform the numerical simulations presented in this work. The geometrical setup and solution methods will be discussed briefly in this chapter.

5.1.1 Geometrical setup

The geometrical meshes were constructed in GAMBIT. GAMBIT is a software package designed to help analysts and designers build and mesh models for computational fluid dynamics (CFD) and other scientific applications. GAMBIT receives user input by means of its graphical user interface (GUI). The GAMBIT GUI makes the basic steps of building, meshing and assigning zone types to a model simple and intuitive.

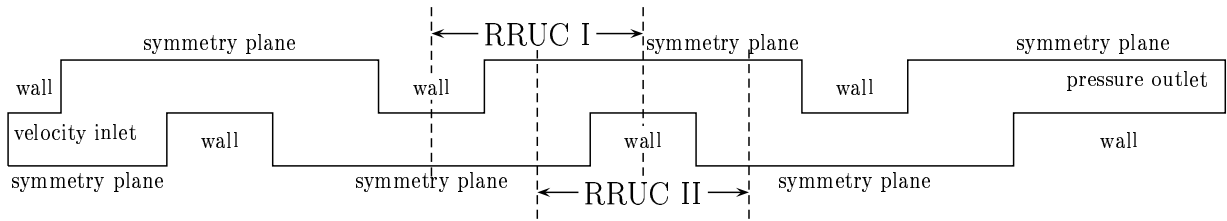


Figure 5.1: The geometrical model for the staggered configuration of porosity, $\epsilon = 0.75$.

The staggered geometrical model

Figure 5.1 shows a graphical representation of the geometrical model constructed in GAMBIT for the staggered configuration of the two-dimensional porous medium with porosity, $\epsilon = 0.75$. The model consists of only the fluid domain with the appropriate boundaries as shown in the figure. The model consists of five RRUC's, with $d = 0.01m$, placed next to each other. An extra solid section is placed after the fifth RRUC to prevent the outlet boundary to cut through a possible recirculation zone. The length of the extra solid section varies depending on the porosities. Computations for analysis are performed on the two RRUC's marked as RRUC I and RRUC II. The remaining RRUC's before and after these RRUC's serve as calming sections, to ensure fully developed flow. The dimension of the RRUC is kept fixed as $d = 0.01m$ and the length of the solid constituent, d_s , is varied to obtain different porosities.

Although not shown in Figure 5.1, a regular square grid is used. The cell width of the square grid elements are taken to be $0.0001m$ in the case of porosities 0.91, through to 0.6636. The cell widths were adapted to $0.00005m$ for porosities lower than 0.6636 to ensure that there are always more than 20 cells in the cross sectional flow area shown in the figure.

5.1.2 Boundary conditions and solution method

The grid geometry constructed in GAMBIT was imported to FLUENT Solver 6.1.22. The two-dimensional double precision mode were selected for the computation purposes. FLUENT Solver is a powerful finite-volume-based program package for modelling general fluid flow in complex geometries.

The boundary conditions, fluid type and solution methods are specified in the FLUENT

Solver before iterating the solver. Symmetry plane boundary condition were used at the top and bottom of the configuration at the fluid boundaries. A no-slip boundary condition applies to all the fluid solid interfaces, marked as wall in Figure 5.1. On the left hand side of the configuration a velocity inlet boundary condition was used to regulate flow at the different Reynolds numbers. The fluid traverses the model and exits on the right through a pressure outlet, where the pressure is kept constant at atmospheric pressure.

For the simulation process a steady solver was used for incompressible viscid laminar Newtonian flow. Water was used as the traversing fluid with a viscosity of $\mu = 0.001003 \text{ N.s.m}^{-2}$ and density $\rho = 998.2 \text{ kg.m}^{-3}$. The SIMPLE algorithm was selected for solving the matrix equations.

The calculation of residuals is used to determine whether a solution has converged. A convergence criterion of 1×10^{-6} was used in this study. The continuity, x -velocity and y -velocity residuals have to meet the specified convergence criterion in order for the solution to be classified as converged. The conservation equation for a general variable ϕ at a cell P can be written after discretization as

$$a_P \phi_P = \sum_{\text{nb}} a_{\text{nb}} \phi_{\text{nb}} + b \quad (5.1)$$

(Patankar, 1980). Here a_P is the center coefficient, a_{nb} are the influence coefficients for the neighbouring cells, and b is the contribution of the constant part of the source term S_c in $S = S_c + S_P \phi$ and of the boundary conditions. The residual computed by FLUENT, R^ϕ , is the imbalance of (5.1) summed over all computed cells P . This quantity may be scaled to yield a more appropriate indicator of convergence as follows

$$R^\phi = \frac{\sum_{\text{cells } P} |\sum_{\text{nb}} a_{\text{nb}} \phi_{\text{nb}} + b - a_P \phi_P|}{\sum_{\text{cells } P} |a_P \phi_P|}. \quad (5.2)$$

5.2 Microscopic flow patterns

In this section the flow patterns in the various flow regimes are discussed and analysed. The pressure and velocity fields are described on a microscopic scale to attempt a better understanding of flow and pressure loss mechanisms.

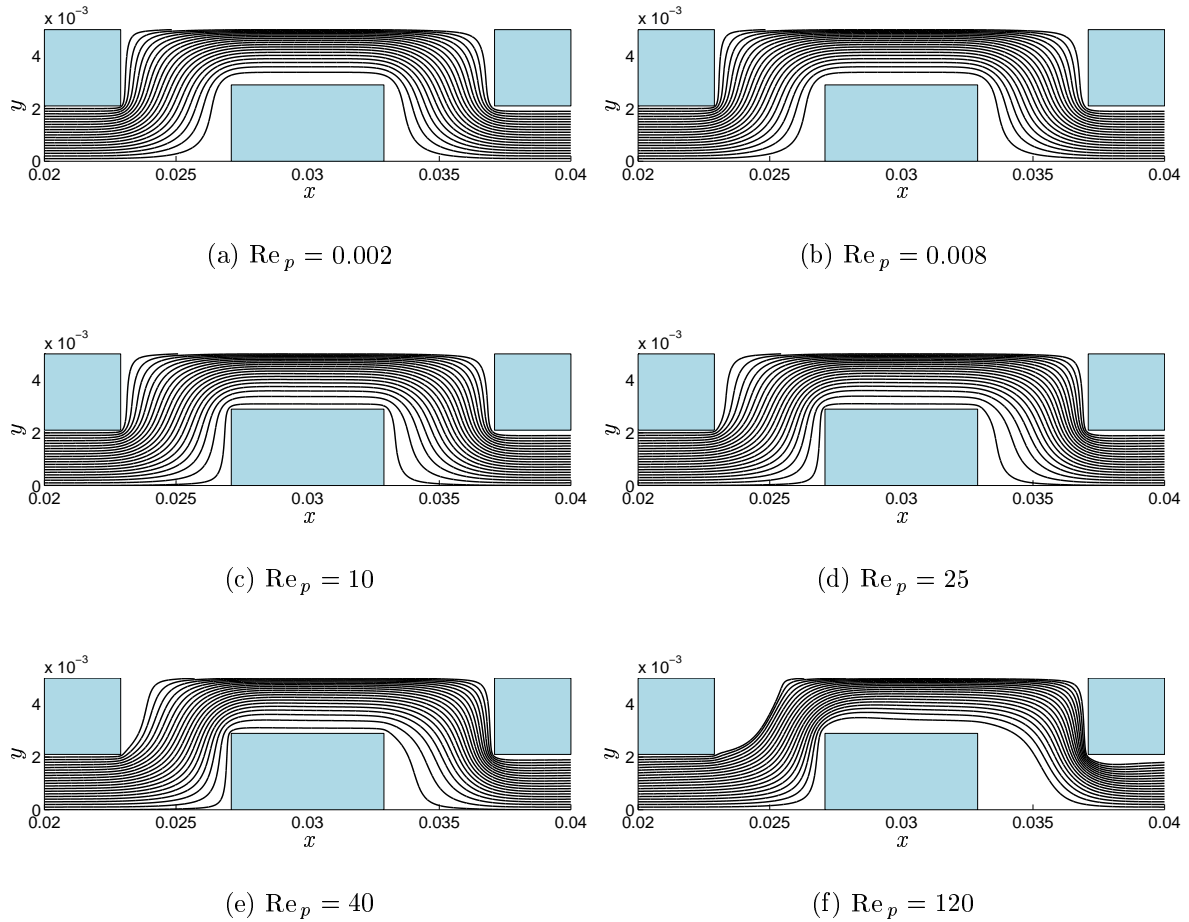


Figure 5.2: A few streamlines at different Reynolds numbers in a staggered square array of porosity 0.6636.

In Figure 5.2 some streamlines at different Reynolds numbers in the staggered configuration of squares are presented. Two adjacent RRUC's of which the boundaries cut the solid are presented, with symmetry planes at the top and bottom of the unit cells.

Figures 5.2 (a) and (b) show streamlines of Reynolds numbers $Re_p = 0.002$ and 0.008 , respectively. Both these Reynolds number are well inside the vanishing inertia or Darcy flow regime ($Re_p \ll 1$). It should be noted that there is no difference between the shape of the streamlines in these two cases. This is an indication that inertial effects have a negligible contribution.

Figures 5.2 (c) to (f) show a few streamlines of cases where Re_p increases. It may be observed from the figures that the shape of the streamlines no longer remains constant but

change with an increase in the Reynolds number. This is an indication that inertial effects increase and tend to predominate the viscous effects.

At larger Reynolds numbers flow separation occurs. This phenomenon can clearly be seen in Figure 5.2 (e). Here the streamline in the figure that is closest to the dividing streamline breaks away at the downstream face of the center square. At this moment, although not shown, a recirculation zone also appears at the downstream face where the streamline separated from the center square. As the Reynolds number is increased even more, as in the case of Figure 5.2 (f), flow separation also occurs at the sides of the squares that are perpendicular to the stream-wise direction. It is expected that both these recirculation zones that develop may have a rather large impact on the macroscopic pressure loss.

A consequence of the flow separation and developing recirculation zones is that the effective pore area for fluid transport narrows. This is apparent in Figure 5.2 (f) where the streamlines are close together in the transverse pore sections. This results in a faster increase of the velocity in the flow tubes than the interstitial velocity.

At intermediate Reynolds number flow (Figure 5.2 (f)) the streamlines tend to straighten in certain pore sections. This results in an impinging effect on the obstructions in the flow path where the essentially straight streamlines bend sharply near the obstruction walls. Due to the straightening of the streamlines, the effective tortuosity decreases as the Reynolds number increases. The straightening streamlines as well as tube narrowing are effects of the predominance of the convection term in the Navier-Stokes equation over the diffusion term. This analysis of the interstitial flow patterns correlates with the analysis and numerical results of Skjetne et al. (1999a).

5.3 Energy dissipation

In this section the viscous dissipation inside an RRUC is computed and analysed to further understanding of the global pressure losses over an RRUC.

The mechanical energy equation may be written as

$$\frac{\rho}{2} \frac{Dv^2}{Dt} = \rho \underline{v} \cdot \underline{f}_b + \nabla \cdot \underline{\underline{\sigma}} \cdot \underline{v} - \underline{\underline{\sigma}} : \nabla \underline{v}, \quad (5.3)$$

where ρ is the density of the fluid, \underline{v} is the fluid velocity, \underline{f}_b is the body force and $\underline{\underline{\sigma}} = \underline{\underline{\tau}} - p\underline{1}$

is the stress tensor, with $\underline{\underline{\tau}}$ the viscous stress tensor (Munson et. al., 1999).

Substituting this expression for the stress tensor into (5.3) results in

$$\frac{\rho}{2} \frac{Dv^2}{Dt} = \rho \underline{v} \cdot \underline{f}_b + \nabla \cdot \underline{\underline{\tau}} \cdot \underline{v} - \nabla \cdot p \underline{1} \cdot \underline{v} - \underline{\underline{\tau}} : \nabla \underline{v} + p \underline{1} : \nabla \underline{v}. \quad (5.4)$$

The viscous dissipation function Φ is normally defined as $\Phi = \underline{\underline{\tau}} : \nabla \underline{v}$. By using some basic tensor identities, the above equation becomes

$$\frac{\rho}{2} \frac{Dv^2}{Dt} = \rho \underline{v} \cdot \underline{f}_b + \nabla \cdot \underline{\underline{\tau}} \cdot \underline{v} - \nabla p \cdot \underline{v} - \Phi + p \nabla \cdot \underline{v}. \quad (5.5)$$

If it is assumed that the fluid is incompressible with a constant density, then $\nabla \cdot \underline{v} = 0$ from the continuity equation. If it assumed that the body-force consists of gravity alone, the terms with the body-force and the pressure gradient may be grouped together as follows

$$\begin{aligned} \rho \underline{g} \cdot \underline{v} - \nabla p \cdot \underline{v} &= -(\nabla p - \rho \underline{g}) \cdot \underline{v} \\ &= -\nabla P \cdot \underline{v}. \end{aligned} \quad (5.6)$$

Equation (5.6) may now be substituted into (5.5) to yield

$$\frac{\rho}{2} \frac{Dv^2}{Dt} = -\nabla P \cdot \underline{v} + \nabla \cdot \underline{\underline{\tau}} \cdot \underline{v} - \Phi. \quad (5.7)$$

The stress tensor of a Newtonian fluid is considered to be $\underline{\underline{\tau}} = \mu (\nabla \underline{v} + \widetilde{\nabla \underline{v}})$. By considering this relation for the stress tensor and by expanding the material derivative, (5.7) becomes

$$\frac{\rho}{2} \frac{\partial v^2}{\partial t} + \frac{\rho}{2} \underline{v} \cdot \nabla v^2 = -\nabla P \cdot \underline{v} + \nabla \cdot \mu \nabla \underline{v} \cdot \underline{v} + \nabla \cdot \mu \widetilde{\nabla \underline{v}} \cdot \underline{v} - \Phi. \quad (5.8)$$

The term containing the transpose velocity gradient dyadic may shown to be zero as follows

$$\begin{aligned} \nabla \cdot \mu \widetilde{\nabla \underline{v}} \cdot \underline{v} &= \mu \nabla (\nabla \cdot \underline{v}) \cdot \underline{v} \\ &= 0, \end{aligned} \quad (5.9)$$

where $\nabla \cdot \underline{v} = 0$ and the viscosity is assumed to be constant. The term in (5.8) which contains the velocity gradient dyadic may also be shown to reduce to zero in the following manner

$$\begin{aligned} \mu \nabla \cdot \nabla \underline{v} \cdot \underline{v} &= \mu \nabla (\nabla \cdot \underline{v}) \cdot \underline{v} - \mu \nabla \times (\nabla \times \underline{v}) \cdot \underline{v} \\ &= 0, \end{aligned} \quad (5.10)$$

where $\nabla \cdot \underline{v} = 0$ and also $(\nabla \times \underline{v}) \cdot \underline{v} = 0$, because $\nabla \times \underline{v}$ produces a vector perpendicular to \underline{v} .

Substitution of (5.9) and (5.10) into (5.8) reveals the mechanical energy equation to be

$$\frac{\rho}{2} \frac{\partial v^2}{\partial t} + \frac{\rho}{2} \underline{v} \cdot \nabla v^2 = -\nabla P \cdot \underline{v} - \Phi. \quad (5.11)$$

Basic vector identities may be used to write the above equation as

$$\begin{aligned} \frac{\rho}{2} \frac{\partial v^2}{\partial t} + \frac{\rho}{2} \nabla \cdot (v^2 \underline{v}) - \frac{\rho}{2} v^2 \nabla \cdot \underline{v} &= -\nabla \cdot (P \underline{v}) + P \nabla \cdot \underline{v} - \Phi \\ \frac{\rho}{2} \frac{\partial v^2}{\partial t} + \frac{\rho}{2} \nabla \cdot (v^2 \underline{v}) &= -\nabla \cdot (P \underline{v}) - \Phi. \end{aligned} \quad (5.12)$$

Equation (5.12) may now be averaged over an REV as follows

$$\frac{\rho}{2} \frac{\partial}{\partial t} \langle v^2 \rangle - \frac{1}{\mathcal{U}_0} \iint_{\mathcal{S}_{fs}} \underline{n} \cdot \underline{v} v^2 d\mathcal{S} + \frac{\rho}{2} \langle \nabla \cdot (v^2 \underline{v}) \rangle = -\langle \nabla \cdot (P \underline{v}) \rangle - \langle \Phi \rangle. \quad (5.13)$$

The surface integral in the above equation reduces to zero if a no-slip boundary condition is applied to all fluid-solid surface interfaces. The time derivative may also be neglected if the interest only lies in the steady solution of the problem. Equation (5.13) therefore reduces to

$$\frac{\rho}{2} \iiint_{\mathcal{U}_f} \nabla \cdot (v^2 \underline{v}) d\mathcal{U} = - \iiint_{\mathcal{U}_f} \nabla \cdot (P \underline{v}) d\mathcal{U} - \iiint_{\mathcal{U}_f} \Phi d\mathcal{U}. \quad (5.14)$$

Application of the divergence theorem (Bear and Bachmat, 1991) to the first two terms of (5.14) yields

$$\begin{aligned} \frac{\rho}{2} \iint_{\partial\mathcal{U}_f} \underline{n} \cdot (v^2 \underline{v}) d\mathcal{S} &= - \iint_{\partial\mathcal{U}_f} \underline{n} \cdot (P \underline{v}) d\mathcal{S} - \mathcal{U}_0 \langle \Phi \rangle \\ \frac{\rho}{2} \iint_{\mathcal{S}_{fs}} \underline{n} \cdot (v^2 \underline{v}) d\mathcal{S} + \frac{\rho}{2} \iint_{\mathcal{S}_{ff}} \underline{n} \cdot (v^2 \underline{v}) d\mathcal{S} &= - \iint_{\mathcal{S}_{fs}} \underline{n} \cdot (P \underline{v}) d\mathcal{S} \\ &\quad - \iint_{\mathcal{S}_{ff}} \underline{n} \cdot (P \underline{v}) d\mathcal{S} - \mathcal{U}_0 \langle \Phi \rangle, \end{aligned} \quad (5.15)$$

since the boundary of \mathcal{U}_f consists of \mathcal{S}_{ff} and \mathcal{S}_{fs} . Both the fluid-solid surface integrals in (5.15) reduce to zero if a no-slip boundary condition is assumed in these surfaces. Thus

$$\frac{\rho}{2} \iint_{\mathcal{S}_{ff}} \underline{n} \cdot (v^2 \underline{v}) d\mathcal{S} = - \iint_{\mathcal{S}_{ff}} \underline{n} \cdot (P \underline{v}) d\mathcal{S} - \mathcal{U}_0 \langle \Phi \rangle. \quad (5.16)$$

When only periodic homogeneous porous media are considered, the surface integral over the fluid-fluid interfaces on the left hand side of (5.16) reduces to zero, since similar flow properties exist in both the entrance and the exit faces of the REV. Therefore

$$- \iint_{\mathcal{S}_{ff}} \underline{n} \cdot (P \underline{v}) d\mathcal{S} = \mathcal{U}_0 \langle \Phi \rangle. \quad (5.17)$$

Consider an RRUC for a prismatic bundle. Let P^{in} be the average pressure on the fluid-fluid interface \mathcal{S}_{ff} at the entrance of the RRUC and let P^{out} be the average pressure on the fluid-fluid interface \mathcal{S}_{ff} at the exit of the RRUC. In an RRUC \mathcal{S}_{ff} is of the same magnitude at the entrance and exit and the flow properties are similar in both the entrance and exit fluid-fluid surface interfaces, and therefore the left hand side of (5.17) may be written as

$$\begin{aligned}
- \iint_{S_{ff}} P \underline{n} \cdot \underline{v} dS &= -P^{\text{in}} \iint_{S_{ff}^{\text{in}}} \underline{n} \cdot \underline{v} dS - P^{\text{out}} \iint_{S_{ff}^{\text{out}}} \underline{n} \cdot \underline{v} dS \\
&= (P^{\text{in}} - P^{\text{out}}) w_{\parallel} \frac{1}{2} S_{ff} \\
&= Q \Delta P,
\end{aligned} \tag{5.18}$$

where w_{\parallel} is the average stream-wise pore velocity and Q is the volumetric flow rate and ΔP is the pressure drop across the RRUC. Thus, (5.17) may be written as

$$Q \Delta P = \iiint_{\mathcal{U}_f} \Phi d\mathcal{U}. \tag{5.19}$$

Equation (5.19) is a macroscopic equation which describes the total energy dissipation over the whole fluid domain (Fourar et al., 2004 and Skjetne et al., 1999c). Equation (5.19) may therefore also be considered as an energy conservation law.

The viscous dissipation function should be computed on every point in the domain to identify the flow domains where energy dissipation is a maximum. The viscous dissipation function may be written as

$$\Phi = 2\mu \left[\left(\frac{\partial v_x}{\partial x} \right)^2 + \left(\frac{\partial v_y}{\partial y} \right)^2 + \frac{1}{2} \left(\frac{\partial v_x}{\partial y} + \frac{\partial v_y}{\partial x} \right)^2 \right]. \tag{5.20}$$

The integral on the right hand side of (5.19) was computed by extracting the derivatives needed for computation of Φ from FLUENT at all the grid points. The viscous dissipation function Φ was then computed at all the grid points with the use of (5.20). These discrete values for Φ were multiplied with the cell volumes corresponding to the different node points and then added to perform the volume integral as a summation over the whole domain.

Figure 5.3 shows the microscopic viscous dissipation function for a staggered configuration of a square array in both the Darcy and Forchheimer regimes. The darker colours resemble

a higher value for the viscous dissipation function. Figures 5.3 (a) and (b) illustrate the relatively even distribution of viscous dissipation throughout the fluid domain of the RRUC in the Darcy regime. The most dissipation occurs on the corners of the RRUC. Although the dissipation is very small, the viscous shear effects of the no-slip condition at the fluid-solid boundaries extend well into the interior of the fluid domain.

Figures 5.3 (c) and (d) show that in the case of the Forchheimer regime, the viscous dissipation is concentrated on the upstream face and the upstream corner of the solid. This is an illustration of the effect of the impinging flow of the flow tube on the obstacle. The flow tube straightens and impinges on the upstream face of the obstacle and then turns sharply in the transverse direction. Observe that the viscous dissipation due to the recirculation zone is negligible. In Figures 5.3 (c) and (d) it also becomes clear in which areas of the fluid domain the fluid may be treated as ideal.

Fourar et al. (2004) numerically computed the viscous dissipation function on a staggered array of cylinders. In their case of an array of cylinders there are regions where the passages for fluid transport are narrower than other regions in the fluid domain, which is not the case with a square array. Fourar et al. (2004) found that in the case of the staggered array of cylinders the viscous dissipation function is a maximum in the narrow passages due to the friction of the fluid at the walls.

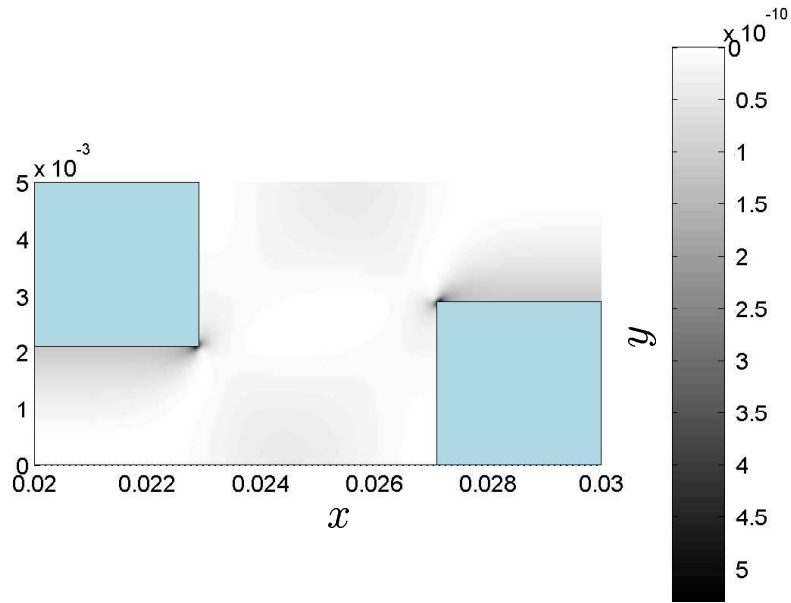
The left hand side of the macroscopic energy conservation equation (5.19) may be plotted against the right hand side. Figure 5.4 (a) shows that the energy conservation principle is satisfied as all the data points lie sufficiently close to the straight line that intersects the origin with a slope of unity. This figure is also an indication that the total macroscopic pressure drop over the porous medium is due to the energy dissipation alone.

Figure 5.4 (b) shows the percentage relative mean error between the total energy dissipation and the integral of the dissipation function over the fluid domain. The mean error was computed as follows

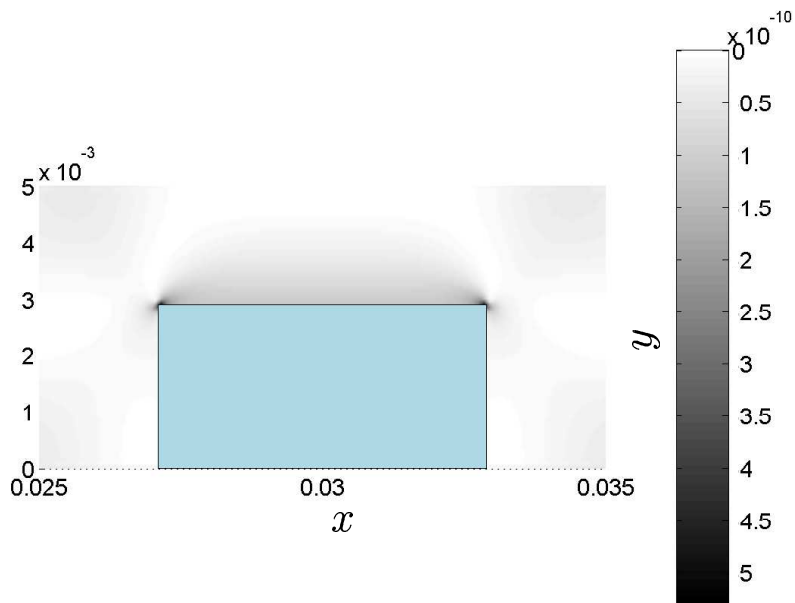
$$E = \left| Q\Delta P - \iiint_{U_f} \Phi dU \right| / |Q\Delta P| \times 100. \quad (5.21)$$

The error is below 2.1 %, which shows that the numerical errors made in the simulation may be taken as minor for the purpose of this study.

CHAPTER 5. NUMERICAL INVESTIGATIONS



(a) Viscous dissipation in an RRUC of type I at $Re_p = 0.002$



(b) Viscous dissipation in an RRUC of type II at $Re_p = 0.002$

Figure 5.3: The viscous dissipation function ϕ in the fluid domain of a staggered RRUC of porosity 0.6636 in the Darcy regime and the Forchheimer regime in units of W/m^2 .

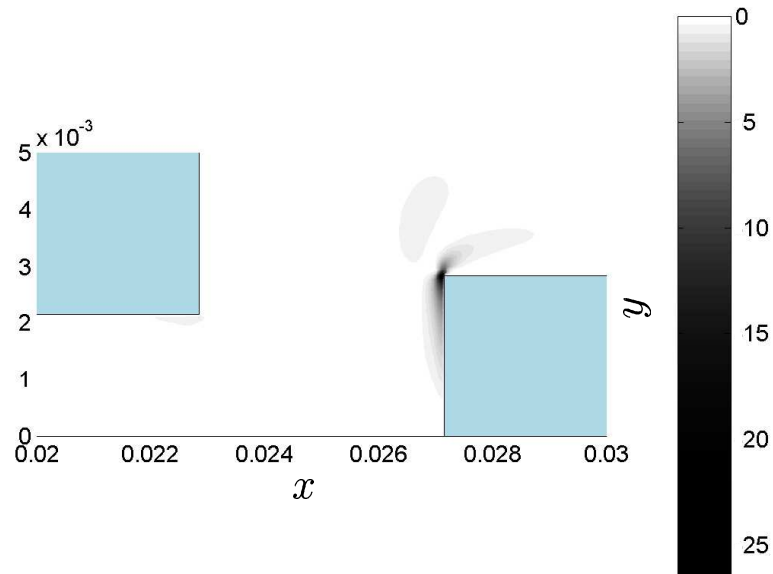
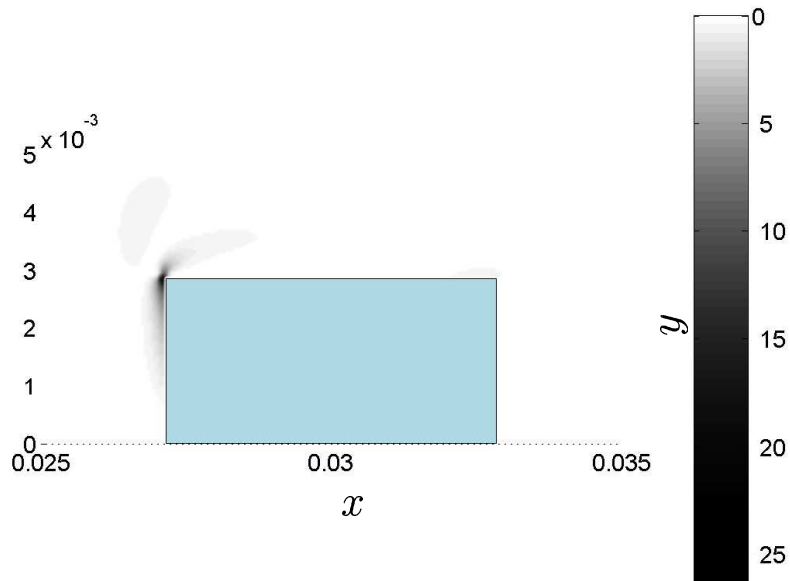
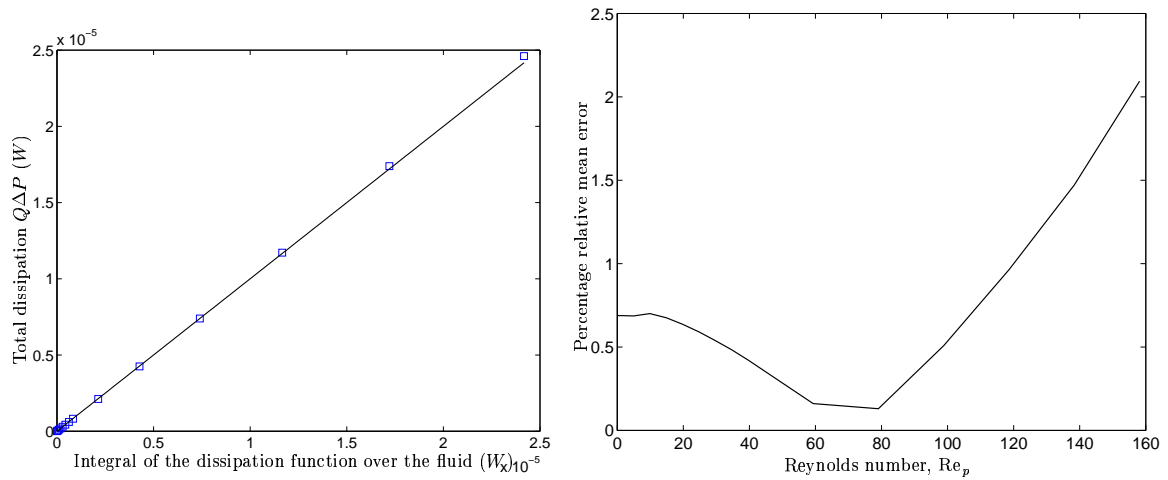
(c) Viscous dissipation in an RRUC of type I at $Re_p = 120$ (d) Viscous dissipation in an RRUC of type II at $Re_p = 120$

Figure 5.3: (Continued) The viscous dissipation function ϕ in the fluid domain of a staggered RRUC of porosity 0.6636 in the Darcy regime and the Forchheimer regime in units of W/m^2 .



(a) Total energy dissipation versus the integral of the viscous dissipation function over the whole fluid domain.

(b) Relative mean error between the total energy dissipation and the integral of the dissipation function.

Figure 5.4: The verification of the energy conservation principle on a staggered RRUC.

5.4 Flow regimes

At sufficiently small Reynolds numbers ($Re_p \ll 1$) the fluid discharge through porous media is governed by Darcy's law,

$$-\frac{dP_f}{dx} = \mu k^{-1} q, \quad (5.22)$$

where $-\frac{dP_f}{dx}$ is the pressure gradient in the stream-wise direction, μ is the viscosity, q is the superficial velocity in the stream-wise direction and k is the Darcy permeability. This empirical law is well understood and can be theoretically verified by the volume averaging procedure (Whitaker, 1986) among other methods. Various experimental findings also verify this linear relationship between the macroscopic pressure gradient and the superficial velocity in the weak inertia regime.

At finite Reynolds numbers near unity ($Re_p = O(1)$), there exists a transition zone between the weak and strong inertia regimes. This transition zone has a cubic relationship between

the macroscopic pressure drop and the superficial velocity,

$$-\frac{dP_f}{dx} = \mu k^{-1} q + \gamma \rho q^3, \quad (5.23)$$

where γ is a dimensionless parameter. This result has been verified numerically by Rojas and Koplik (1998) and Skjetne et al. (1999a) among others, and theoretically derived for homogeneous isotropic porous media by the use of double scale homogenisation (Wodie and Levy, 1991).

For larger Reynolds numbers ($\text{Re}_p \gg 1$), before the onset of turbulence, the macroscopic pressure gradient is said to be in a quadratic relation with the superficial velocity

$$-\frac{dP_f}{dx} = \mu k_{fh}^{-1} q + \alpha \rho q^2, \quad (5.24)$$

where k_{fh} is the Forchheimer permeability and α is a dimensionless parameter. Equation (5.24) is known as the Forchheimer law for high-velocity flow through porous media. The Forchheimer equation resembles an imperial law that, despite of the fact that it exists for over a hundred years, still lacks a complete understanding of the physical motivations for the good correlation with experimental results.

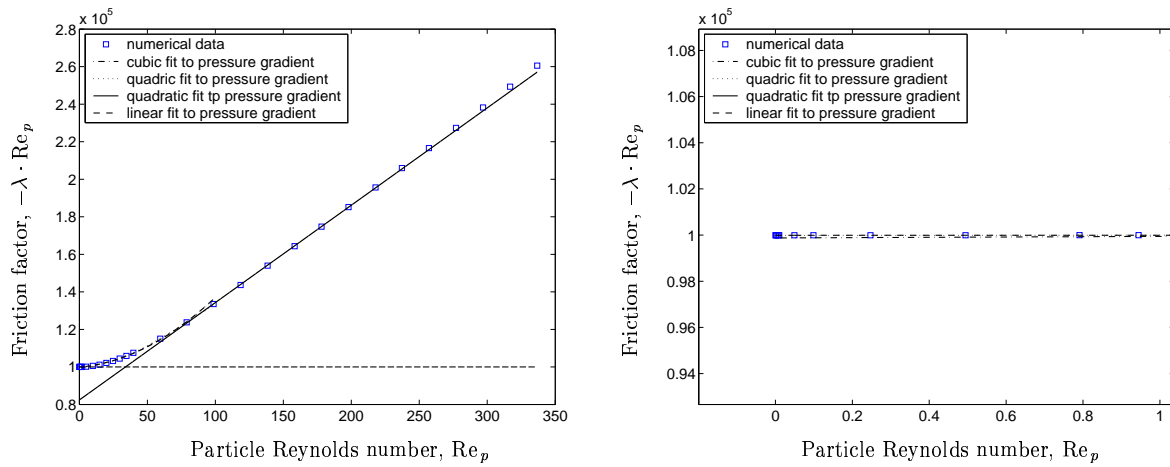
It should be noted that there is a difference between the Darcy permeability k and the Forchheimer permeability k_{fh} , and the Forchheimer equation can therefore not be used to calculate the pressure drop in both the Darcy, transitional and Forchheimer regimes. The current RRUC modelling procedure discussed in Chapter 4 only uses a Forchheimer-type equation by adding the drag forces in the darcy and Forchheimer regimes.

A turbulent flow regime may be identified beyond the laminar flow regime, which can be described by

$$-\frac{dP_f}{dx} = \mu k_{fh,t}^{-1} q + \alpha_t \rho q^2, \quad (5.25)$$

where $k_{fh,t} \neq k_{fh}$ and $\alpha_t \neq \alpha$. Whether or not the turbulent Forchheimer regime is entered through a transition to turbulent flow regime is a matter of the complexity of the porous material geometry (Skjetne and Auriault, 1999b). The focus of this work falls on the laminar flow regime and no further reference will be made to the turbulent flow regime.

CHAPTER 5. NUMERICAL INVESTIGATIONS



(a) Entire laminar particle Reynolds number range.

(b) The weak inertia (or Darcy regime) Reynolds number range.

Figure 5.5: Graphs of Reynolds number versus the defined friction factor times the Reynolds number for a staggered configuration with porosity 0.4224.

Figure 5.5 shows the different flow regimes that may be observed from numerical simulations on a fibre bed with a staggered configuration and a porosity of 0.4224. Figure 5.5 (a) shows the relation for the entire range of Reynolds numbers in the laminar flow regime. It may be observed that the numerical data fits the straight line very well for Reynolds numbers varying approximately between 80 and 240. This indicates that the pressure drop is in a quadratic relation to the Darcy velocity and it may be assumed that we find ourselves in the strong inertia or Forchheimer regime. Beyond $Re_p = 240$ the numerical data points tend to deviate from the straight line. This could be an indication of the turbulent or transition to turbulent flow regime. It should be noted that during the simulation process no model was used for the computation of turbulent viscosity, because the interest of this work falls on the laminar regime only. The deviation may therefore be a result of error prone computations, thus indicating the end of the physical laminar regime.

Figure 5.5 (b) shows the Darcy regime or vanishing inertia regime. It may be observed that the numerical data points fit the straight horizontal line very well. This behaviour indicates that the numerical pressure gradient is in a linear relationship with the superficial velocity. It should be safe to say that these numerical data points form part of the Darcy flow regime.

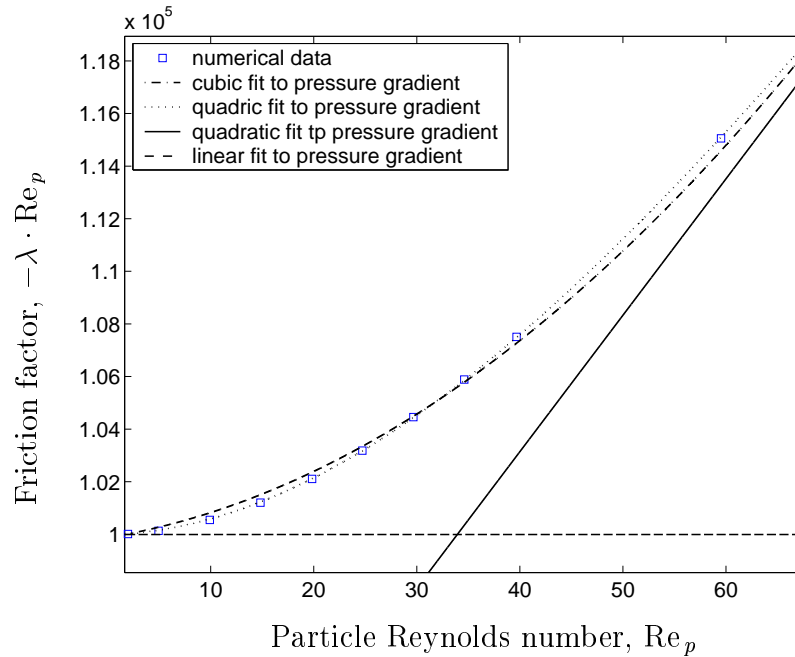


Figure 5.6: Graph of the transition zone with the Reynolds number versus the defined friction factor times the Reynolds number for a staggered configuration with porosity 0.4224.

Figure 5.6 shows the transition zone for fluid flow through a staggered configuration of porosity 0.4224. According to (5.23), if the dashed-dotted line in the figure fits the numerical data well then the cubic relation between the pressure gradient and the superficial velocity is verified. Although the data is fitted well, it seems that in this specific case, a quadric relationship between the pressure gradient and the superficial velocity is more appropriate. No physical explanation for this behaviour can be presented.

Fourar et al. (2004) conducted the same type of numerical simulations. The commercial CFD code FEMLAB was used by them to perform numerical simulations on two-dimensional cylindrical porous media as well as three-dimensional spherical porous media at a wide range of laminar Reynolds numbers. The results and conclusions of the two-dimensional simulations correspond well to the results and conclusions presented in this work. Three laminar flow regimes (Darcy, transition and Forchheimer) were identified and in the transition regime the pressure gradient was also considered to be in a cubic relation to the Darcy velocity.

A very important result was obtained by Fourar et al. (2004) concerning the transition regime in three-dimensional porous media. That is, the Reynolds number range of the

transition regime in three-dimensional porous media is considerably smaller than that of the two-dimensional porous medium. The example used by the mentioned authors consisted of a three-dimensional and two-dimensional porous medium both with a porosity of $\epsilon = 0.386$. It was found in this case that the transition regime was 17 times smaller for the three-dimensional porous medium than for the two-dimensional porous medium. This result emphasises the difficulty for experiments to be performed in the transition regime.

Figure 5.7 shows the graphs of the friction factor λ times the Reynolds number versus the Reynolds number for the numerical results obtained for different porosities of the staggered arrangement. Examination of the different graphs shows the Reynolds number range of the different flow regimes to be dependent on the porosity of the medium. The solid line in the graphs represents the quadratic fit to the pressure drops. This makes it easy to observe that the flow enters the turbulent or transition to turbulent regime earlier with respect to the Reynolds number when the porosity increases. This phenomenon could intuitively be explained by noting that as the porosity increases, the interstitial pore diameter increases and more cross-sectional fluid area becomes available for eddy's and vortex shedding.

5.5 The momentum equation and drag

In this section it will be numerically verified that the momentum equation

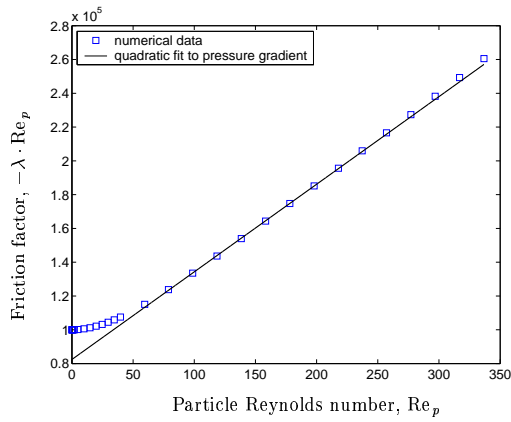
$$-\epsilon U_0 \nabla P_f = \iint_{S_{fs}} \underline{n} p dS - \iint_{S_{fs}} \underline{n} \cdot \underline{\tau} dS \quad (5.26)$$

holds for a prismatic bundle. Clarity will also be given on the magnitude of the contributions of each of the surface integrals to the total pressure drop over the entire range of Reynolds numbers in the laminar flow regime.

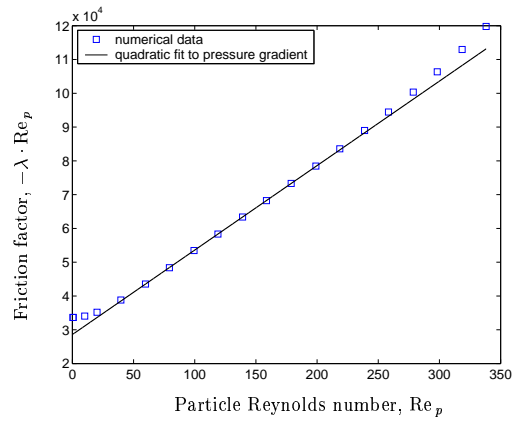
Equation (5.26) may be written in dimensionless form as follows in terms of the friction factor λ , and particle Reynolds number Re_p

$$-\lambda Re_p = \frac{1}{\mu q \epsilon} \left[\iint_{S_{fs}} \underline{n} p dS - \iint_{S_{fs}} \underline{n} \cdot \underline{\tau} dS \right]. \quad (5.27)$$

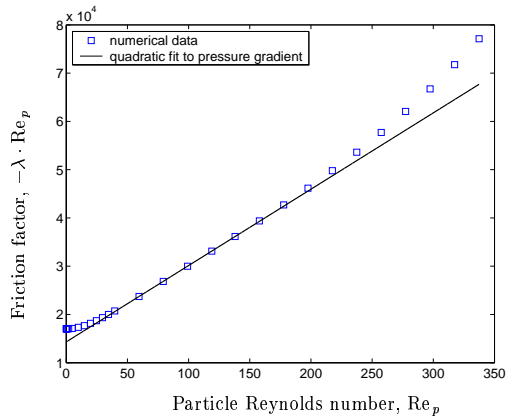
CHAPTER 5. NUMERICAL INVESTIGATIONS



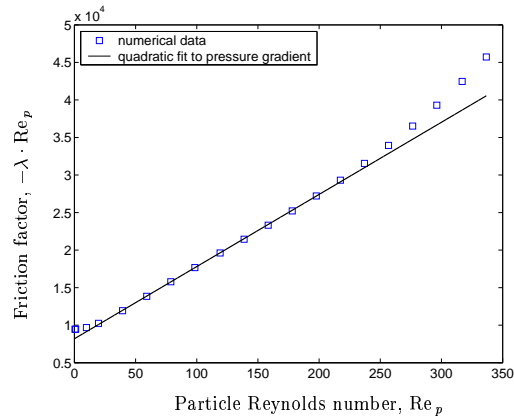
(a) Porosity, $\epsilon = 0.4224$



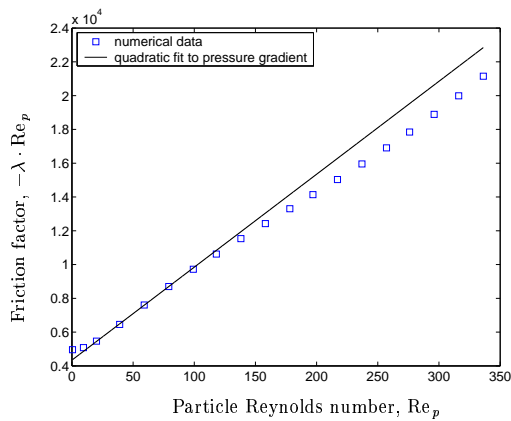
(b) Porosity, $\epsilon = 0.5644$



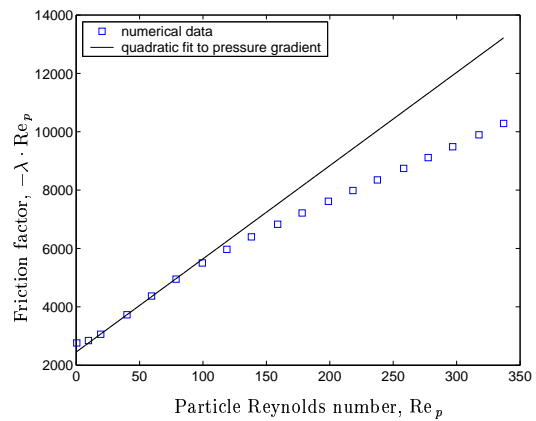
(c) Porosity, $\epsilon = 0.6636$



(d) Porosity, $\epsilon = 0.75$



(e) Porosity, $\epsilon = 0.84$



(f) Porosity, $\epsilon = 0.91$

Figure 5.7: Friction factor times the Reynolds number versus the Reynolds number for different porosities.

The first term on the right hand side of (5.27) resembles the dimensionless pressure drag, while the second term on the right hand side resembles the dimensionless friction drag. The left hand side is the total dimensionless drag on the porous medium, in analogy to the work done by Fourar et al. (2004).

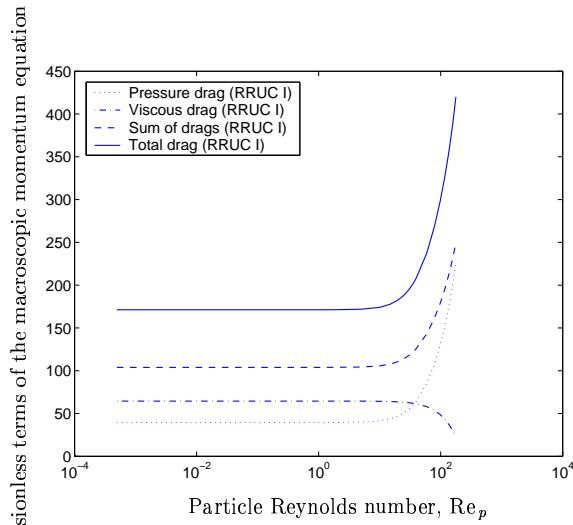
Figure 5.8 illustrates the magnitude of the contributions of the dimensionless pressure and viscous drag to the total dimensionless macroscopic drag in the stream-wise direction. The surface integral of the pressure is only performed over S_{\perp} , since the surface integral of the pressure on S_{\parallel} results in a vector quantity perpendicular to the stream-wise direction. The surface integral of the shear stress, on the other hand, is only computed over S_{\parallel} , since in this case the surface integral of the shear stress over S_{\perp} results in a vector quantity that is perpendicular to the stream-wise direction.

It may be observed from Figure 5.8 (a) that the dimensionless viscous and pressure drags do not add up to the total dimensionless macroscopic drag if the RRUC I configuration is used. In the same manner Figure 5.8 (b) illustrates that the dimensionless viscous and pressure drags do not add up to the total dimensionless macroscopic drag if the RRUC II configuration is used. This occurrence may be justified by observing that neither the RRUC I nor the RRUC II configuration is representative of the porous medium. Figure 5.8 illustrates that if the dimensionless drags of the different RRUC configurations illustrated in Figures 5.8 (a) and (b) are weighed according to their relative frequency of occurrence (Lloyd et al., 2004), they add up to the macroscopic dimensionless drag.

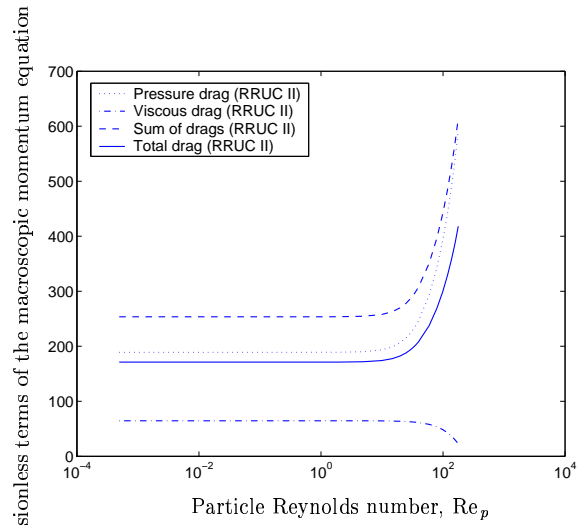
An important result that becomes apparent in Figure 5.8 is the meaningful contribution of the viscous fluid-surface integral of the momentum equation (5.26). Another observation with reference to Figure 5.8 (c) at the Darcy limit is that the pressure drag is substantially larger than the viscous drag. The difference between the viscous and pressure drags remains essentially constant throughout the Darcy regime, but increases towards the laminar Forchheimer limit. Although the viscous drag term of the momentum equation is much smaller than the pressure drag term through the whole laminar flow regime, it is never negligible compared to the pressure drag term.

The results displayed in Figure 5.8 (c) shows that the assumptions made in the Darcy limit do not seem to be applicable for the staggered configuration (see section 4.5.2). In the RRUC model the surface integrals of the wall shear stress in the transverse pore sections were included to incorporate the pressure drop in the transverse pore section in the stream-wise direction. These pressure drops were, however, already incorporated through the pressure modelling techniques discussed in section 4.4. Therefore, the wall shear stress

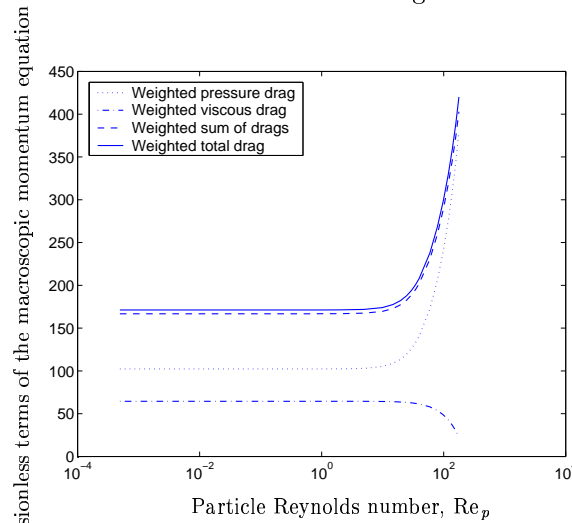
CHAPTER 5. NUMERICAL INVESTIGATIONS



(a) The dimensionless drag terms for the RRUC I configuration.



(b) The dimensionless drag terms for the RRUC II configuration.



(c) The weighted dimensionless drag terms of RRUC I and RRUC II according to their relative frequency of occurrence.

Figure 5.8: The contribution of the pressure and viscous dimensionless drags to the total dimensionless macroscopic drag for a two-dimensional prismatic bundle with a porosity of 0.6636.

should only be integrated over the stream-wise pore section. This was done to obtain the results displayed in Figure 5.8 (c). Equation (4.39) should then become

$$G_0 = \frac{12 \epsilon \sqrt{1 - \epsilon}}{d^2 (1 - \sqrt{1 - \epsilon})^3}. \quad (5.28)$$

In this chapter the numerical results obtained by FLUENT have been presented. The results are similar to those obtained by Fourar et. al. (2004). Observations regarding the microscopic flow patterns also correlates with that found by Skjetne et al. (1999). It was also shown that the wall shear stress should only be integrated over the stream-wise pore sections and not in the transverse pore sections.

Chapter 6

Verification of modelling assumptions

In this chapter the various assumptions made in the modelling procedure at intermediate Reynolds number flow (section 4.5) will be tested numerically. The aim of this exercise is to identify possible areas where the model could be improved to obtain better analytical results.

6.1 Negligible skin drag

The first assumption made in modelling the intermediate Reynolds number flow regime was that the shear stress surface integral in (4.32) is negligible compared to the pressure surface integral (refer to section 4.5.3).

Consider the dimensionless form of the macroscopic momentum transfer equation,

$$-\lambda \text{Re}_p = \frac{1}{\mu q \epsilon} \left[\iint_{S_{fs}} \underline{n} p dS - \iint_{S_{fs}} \underline{n} \cdot \underline{\underline{\tau}} dS \right]. \quad (6.1)$$

Figure 6.1 shows the percentage of the ratio of the dimensionless friction drag (second term on the right hand side of (6.1)) to the dimensionless pressure drag (first term on the right hand side of (6.1)), plotted against the Reynolds number. It is clear from the figure that in the high Reynolds number limit, the skin friction forces become negligible compared to the

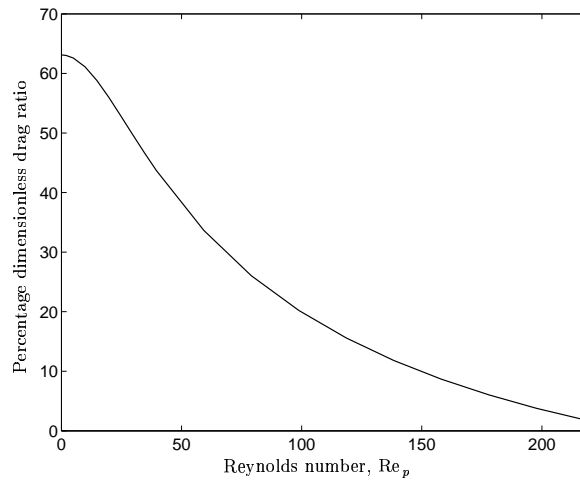


Figure 6.1: The percentage of the ratio of the dimensionless friction drag to the dimensionless pressure drag plotted against the Reynolds number for a porosity of 0.6636.

pressure drag forces. Therefore, the assumption to drop the shear stress surface integral from the macroscopic momentum equation when modelling intermediate Reynolds number flow may be considered as a good approximation.

6.2 Distributions of wall pressures

In this section the assumptions concerning the pressure distributions on the walls of the solid obstruction are investigated. To ease reference the schematic representation of the top half of the RRUC displayed in Figure 4.10 is repeated in Figure 6.2.

6.2.1 Pressures on the upstream face

In section 4.5.3 the assumption was made that the pressure is evenly distributed on the upstream face (face a in Figure 6.2) of the solid obstruction. The mean pressure on face a , \bar{p}_a was calculated and compared to the maximum pressure on face a , p_a to investigate the validity of this assumption. A relative percentage error between the two values is computed as follows

$$p_a^{error} = \frac{|p_a - \bar{p}_a|}{p_a} \times 100. \quad (6.2)$$

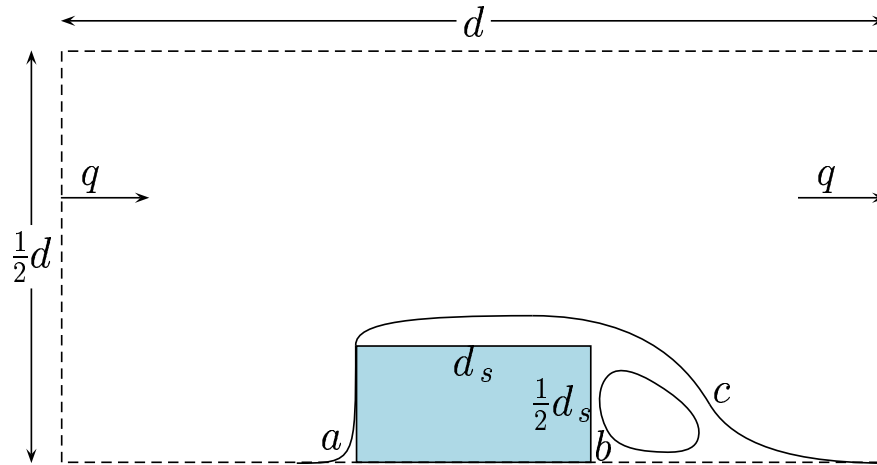
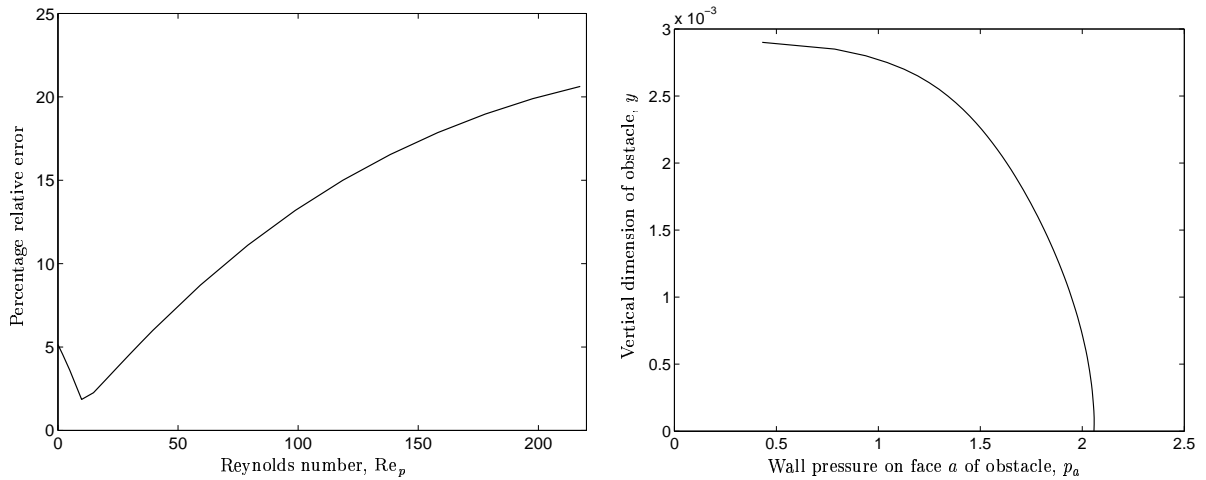


Figure 6.2: A two-dimensional schematic representation of interstitial flow recirculation in the upper half of an RRUC.

Figure 6.3 (a) displays a plot of the relative percentage error p_a^{error} against the Reynolds number. The figure indicates that in the case of the high Reynolds number limit, it is not a very good approximation to set the mean pressure on the upstream face equal to the maximum pressure on the face. In the case of low Reynolds number flow this type of approximation would be acceptable as the relative percentage error is 5%. In the intermediate Reynolds number case the value of the relative percentage error increases to almost 20%.

Figure 6.3 (b) illustrates a typical pressure profile on the upstream face in the intermediate Reynolds number limit. It should be noted that the figure only shows the top half of the obstruction's horizontal dimension. At the center of the obstruction where the flow impinges and the dividing or stagnant streamline may be found, the pressure is the largest. The pressure then decreases smoothly towards the corners of the solid obstruction. This is the type of pressure profile that one might expect, because the velocity of the fluid is the smallest at the center of the obstruction's upstream face and the largest at the corners. According to the Bernoulli equation high velocities are associated with low pressure values, whereas low velocities are associated with high pressure values.

CHAPTER 6. VERIFICATION OF MODELLING ASSUMPTIONS



(a) The relative percentage error of assuming uniform pressure distribution on the upstream face versus the Reynolds number.

(b) The pressure distribution on the upstream face of the solid at a Reynolds number of 180.

Figure 6.3: The variation of the wall pressure on the upstream face, face a , of the solid obstruction in a staggered configuration with a porosity of 0.6636 at Reynolds number $Re_p = 180$.

6.2.2 Pressures on the downstream face

Similar to the case of the pressure distribution on the upstream face of the solid, the pressure distribution on the downstream face of the solid was also assumed to be constant and equal to the maximum pressure value. The relative percentage error is computed in the same manner as in the previous subsection to verify this assumption as follows

$$p_b^{error} = \frac{|p_b - \bar{p}_b|}{p_b} \times 100, \quad (6.3)$$

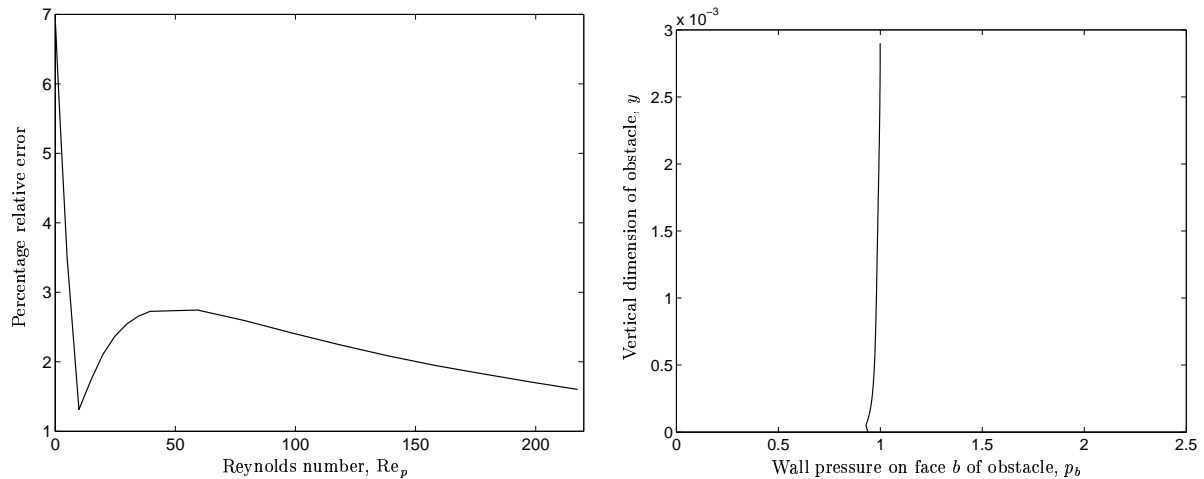
where p_b^{error} denotes the relative percentage error, p_b is the maximum pressure on the downstream face of the solid and \bar{p}_b is the mean of the pressure on face b .

Figure 6.4(a) shows the plot of the relative percentage error p_b^{error} against the Reynolds number. From the figure it is evident that it is a good approximation in the intermediate Reynolds number limit to assume a constant wall pressure distribution on the downstream

CHAPTER 6. VERIFICATION OF MODELLING ASSUMPTIONS

face of the solid obstruction, as the value of the relative percentage error is below 2 percent.

Figure 6.4 (b) displays a typical pressure profile in the intermediate Reynolds number limit, where the pressure values are plotted on the horizontal axis and the vertical dimension of the solid obstruction are plotted on the vertical axis. The profile almost forms a straight vertical line.



(a) The relative percentage error of assuming uniform pressure distribution on the downstream face versus the Reynolds number.

(b) The pressure distribution on the downstream face of the solid at a Reynolds number of 180.

Figure 6.4: The variation of the wall pressure on the upstream face, face b , of the solid obstruction in a staggered configuration with a porosity of 0.6636 at Reynolds number $Re_p = 180$.

6.2.3 Pressures on the downstream face and the inflection point pressure

In section 4.5.3 it was also assumed that the pressure inside the recirculation zone at the lee side of the solid obstruction is constant and equal to the pressure at the inflection point of the dividing streamline. To test this assumption a streamline sufficiently close to the dividing streamline should be extracted from the solution of the intra pore flow field. It is difficult to extract the dividing streamline from a numerically computed flow field, because round off errors, although small, may cause a streamline to follow an alternative path.

CHAPTER 6. VERIFICATION OF MODELLING ASSUMPTIONS

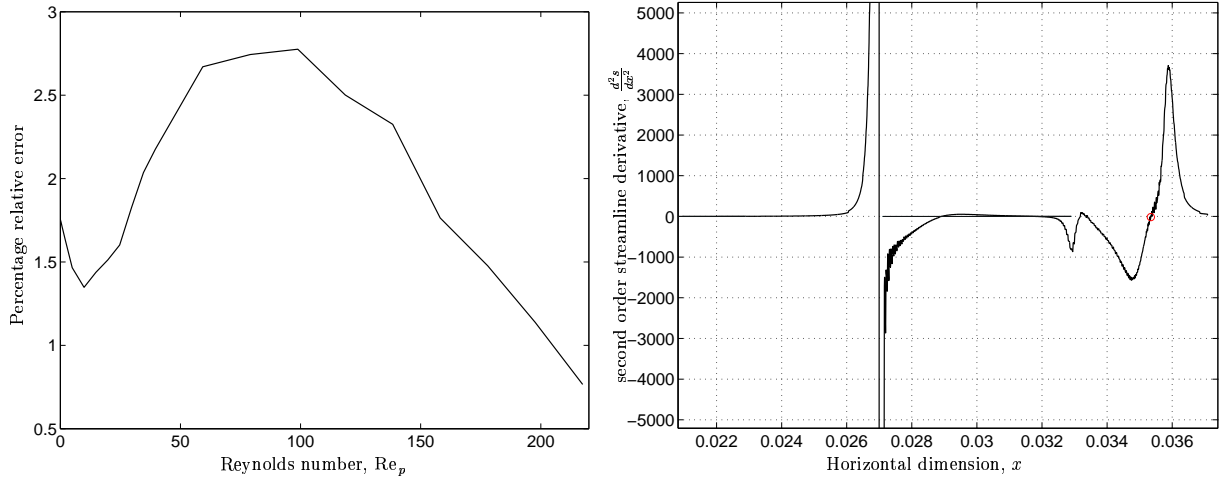
Figure 6.5 (c) shows such a streamline in the case of the staggered configuration with a porosity of 0.6636 and with a Reynolds number of $Re_p = 160$. The streamline was computed as close as numerically possible to the dividing streamline with the MATLAB *stream2* function for two-dimensional streamline computation. The inflection point on the lee side of the recirculation zone is indicated by a circle.

The computation of the position of the inflection point on the streamline was conducted by computing the second order derivatives of the streamline numerically by means of a central differencing scheme. The second order derivative of a function is a criterion for the degree of con-cavity of the function, which would result in a positive expression for a convex function and a negative expression of a concave function. The inflection point of a function is the point where the function changes from concave to convex or vice versa, in other words where the second order derivative of the function intersects the horizontal x -axis.

Figure 6.5 (b) illustrates the second order derivative of the y -coordinates of the dividing streamline shown in Figure 6.5 (c). From the graph it is visible that there are three inflection points on the streamline under consideration. The first inflection point is near the upstream face of the solid obstruction where the streamline changes from a convex function to a concave function. Observe the high values for the second order derivatives, which corresponds to the sharp bends that the impinging effect has on the streamlines. The second inflection point is on the top side of the solid, where flow separation induces small recirculation zones. The third inflection point is the last point where the second order derivative of the streamline cuts the x -axis and this is also the point of interest and is therefore indicated with a circle.

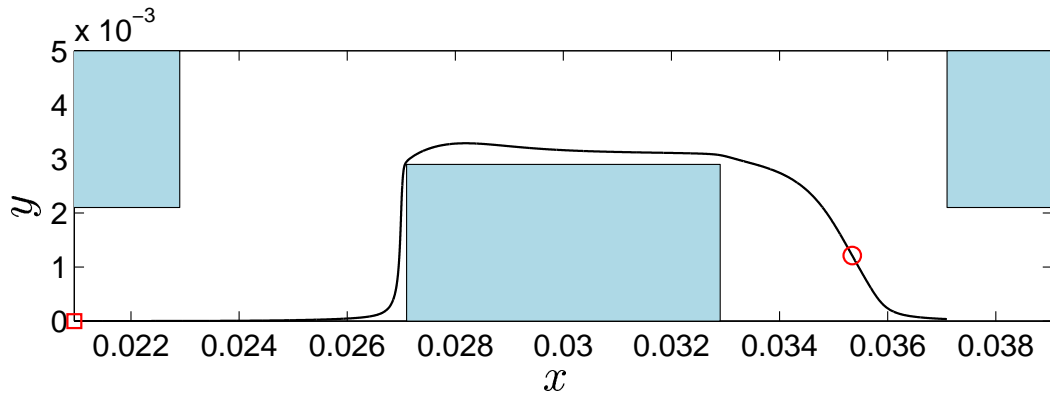
Figure 6.5 (a) shows the percentage relative error made by assuming that the mean wall pressure on face b is equal to the pressure at the inflection point. It seems that this is a good approximation to make in all flow regimes, but exceptionally good in the intermediate Reynolds number limit where the percentage relative error is below 1 percent.

CHAPTER 6. VERIFICATION OF MODELLING ASSUMPTIONS



(a) The relative percentage error of assuming equal pressures on face b and at the inflection point plotted against the Reynolds number.

(b) The second order derivative with respect to x of the dividing streamline at Reynolds number $Re_p = 160$.



(c) The dividing streamline at Reynolds number $Re_p = 160$.

Figure 6.5: Some of the properties of the inflection point of the dividing streamline on a staggered configuration with a porosity of 0.6636.

6.3 The use of the Bernoulli equation

In the first modelling approach of section 4.5.3 the Bernoulli equation was used to predict the pressure surface integral of the macroscopic momentum transport equation (4.32) in terms of the velocity at the inflection point. The velocity at the inflection point was in turn modelled as a geometrical factor β times the interstitial stream-wise velocity $w_{||}$. Investigation towards the β factor will commence in the next section. It was already shown in section 6.2.1 that the surface integral of the pressure on the upstream side is not correctly modelled as uniform and equal to the pressure at the stagnation point.

The validity of using the Bernoulli equation in the fashion of the first modelling approach of section 4.5.3 is tested numerically in this section. This is achieved by extracting the pressure and velocity magnitude on the dividing streamline where it enters Figure 6.5 (c) (indicated by a square) from the numerical solution. The pressure and velocity magnitude at this point is denoted by p_{∞} and v_{∞} respectively. The velocity magnitude at the inflection point (indicated by a circle) is then also extracted from the numerical solution and denoted as v_c . These three values are then substituted into the Bernoulli equation to obtain the computed value for the pressure at the inflection point p_{bern} as follows

$$p_{bern} = \frac{\rho}{2} (v_{\infty}^2 - v_c^2) + p_{\infty}. \quad (6.4)$$

The actual value of the pressure at the inflection point p_c , as obtained from the simulation, is compared with the value computed from the Bernoulli equation.

Figure 6.6 shows the percentage relative error between the computed and numerically obtained pressure at the inflection point. It is expected that there could be substantial errors made in the low Reynolds number flow regime, as the Bernoulli equation is not permitted for use in a viscous flow regime. The error increases towards the intermediate Reynolds number flow regime to about fifty percent. Fluid motion at high flow rates are often modelled as an ideal fluid where there is a balance of energy on a streamline and the Bernoulli equation is mostly used for these calculations.

It seems from Figure 6.6 that there is a loss of energy on the streamline used for the computation of the pressure at the inflection point by means of the Bernoulli equation. Although the fluid is moving at a sufficiently large flow rate to be modelled as in-viscid, it still has a small frictional boundary layer due to the no slip boundary condition on the fluid

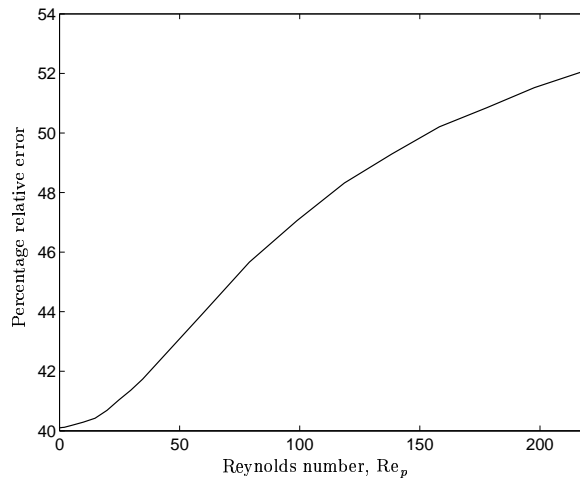


Figure 6.6: The percentage relative error between the computed pressure at the inflection point and the numerical value of the pressure at the inflection point on a staggered configuration with a porosity of 0.6636.

solid interfaces. Also from Figure 5.3 (c) and (d) it should be noted that there is a high rate of viscous dissipation on face a as well as on the corner of the solid obstruction and the streamline used for the Bernoulli equation passes through this region. Therefore it is expected that there should be an energy loss and the Bernoulli equation is not permitted to be used in this fashion. A total energy conservation law should be used instead to account for the energy losses due to the viscous dissipation.

6.4 The inflection point velocity as a ratio of the interstitial stream-wise velocity

This section is concerned with the numerical validation of the modelling of the velocity magnitude at the inflection point in terms of the interstitial stream-wise velocity. In section 4.5.3 it was assumed that the velocity magnitude at the inflection point may be written in terms of the geometrical parameter β as follows

$$v_c \approx w_{\perp} = \beta w_{\parallel}. \quad (6.5)$$

CHAPTER 6. VERIFICATION OF MODELLING ASSUMPTIONS

Figure 6.7 (a) shows the calculated value for the β coefficient, computed from the numerical solution with the use of (6.5), plotted against the Reynolds number. The geometrical modelling procedures of Chapter 4 led to a value of $\beta = 0.5$. This is due to the fact that the stream tube splits in two in the case of the staggered configuration. From the figure it is evident that the computed β values is not equal to 0.5, although in the intermediate Reynolds number limit the values seem to approach 0.5. This is not sufficiently close enough to qualify as a good modelling approximation. The low Reynolds number part of the graph has no useful meaning, because the inflection point is in the laminar boundary layer and it is expected that the velocity would not correspond adequately.

Figures 6.7 (b) and (c) show a few velocity vector plots. A longer arrow is associated with a higher velocity magnitude. The inflection point is marked with a circle. Figure 6.7 (c) is a magnification of the area around the inflection point to give some insight on the problem at hand. Figure 6.7 (c) reveals that the velocity magnitude is not entirely representative of the mean velocity magnitude in the effective pore area of the transverse flow channel. The velocity magnitude at the inflection point seems to be much smaller than the average velocity magnitude in the effective transverse pore area.

6.5 Asymptote matching

This section is devoted to the numerical investigation of the accuracy of the asymptote matching technique used in section 4.5.4 for flow through a prismatic bundle.

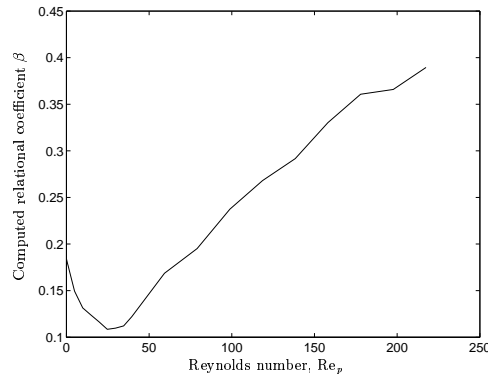
In Figure 6.8 the numerical data for a staggered configuration with a porosity of 0.6636 are indicated by squares. A linear polynomial is fitted to the data in the Darcy regime and indicated by the dashed dotted line, while a quadratic polynomial is fitted to the data in the Forchheimer regime and indicated by a dashed line.

The equation obtained through the least squares fit of a linear polynomial is given by

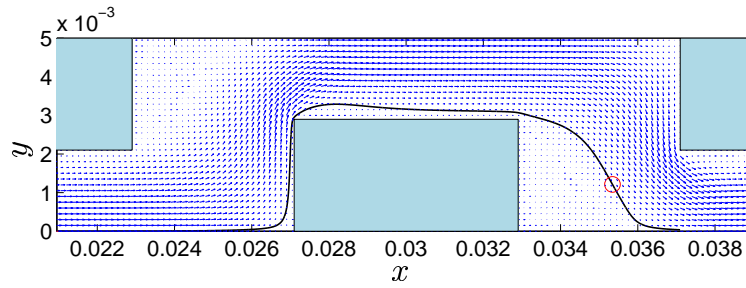
$$-\frac{dP_f}{dx} = 1.717 \times 10^3 q - 6.230 \times 10^{-10}. \quad (6.6)$$

From (6.6) it is evident that the constant term is equal to zero and that the Darcy equation holds. By dividing the viscosity by the coefficient of the linear term, the Darcy permeability $k = 5.842 \times 10^{-7}$ is obtained. The equation obtained through the least squares fit of a

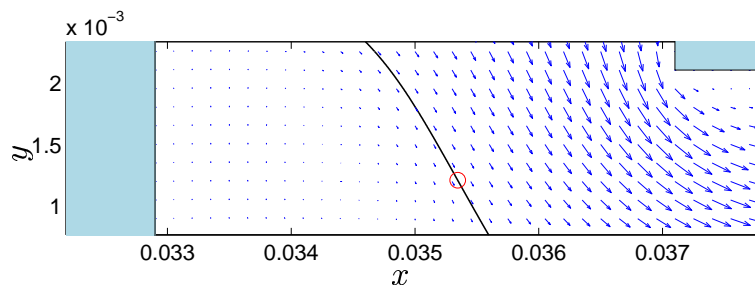
CHAPTER 6. VERIFICATION OF MODELLING ASSUMPTIONS



(a) The numerically computed β values plotted against a range of Reynolds numbers.



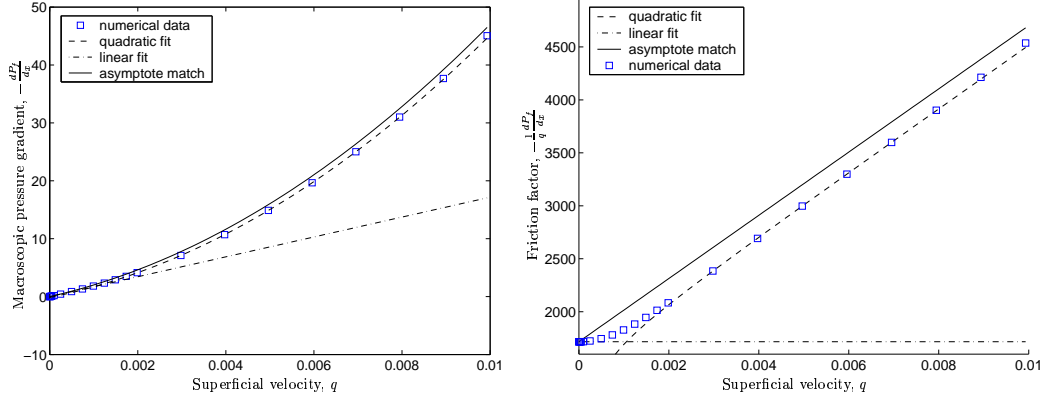
(b) A velocity vector plot with the dividing streamline at Reynolds number $Re_p = 160$.



(c) A magnification of the velocity vector plot near the inflection point at a Reynolds number of $Re_p = 160$.

Figure 6.7: The numerically computed β coefficients for different Reynolds numbers and the velocity vectors near the inflection point for a staggered configuration with a porosity of 0.6636.

CHAPTER 6. VERIFICATION OF MODELLING ASSUMPTIONS



(a) Superficial velocity versus the macroscopic pressure gradient.

(b) Superficial velocity versus a friction factor.

Figure 6.8: A graph of the numerical data and the curve obtained through asymptote matching with a shifting parameter of $s = 1$ for a porosity of 0.6636.

quadratic polynomial to the data is given by

$$-\frac{dP_f}{dx} = 2.984 \times 10^5 q^2 + 1.547 \times 10^3 q - 1.535 \times 10^{-1}. \quad (6.7)$$

From (6.7) it is clear that the constant term is not equal to zero. If the viscosity is divided by the coefficient of the linear term, the Forchheimer permeability $k_{fh} = 6.485 \times 10^{-7}$ is obtained. It is therefore numerically shown that $k \neq k_{fh}$ and that the Forchheimer equation can not, in general, be used for both the Darcy and the Forchheimer regimes. It should be noted that although $k \neq k_{fh}$, the values of k and k_{fh} are near enough to each other to consider $k = k_{fh}$ a sufficient modelling approximation.

The solid line in Figure 6.8 indicates the result of the asymptote matching technique applied to the linear term of (6.6) and the quadratic term of (6.7) with a shifting parameter of $s = 1$ in the following manner

$$-\frac{dP_f}{dx} = \left[(1.717 \times 10^3 q)^s + (2.984 \times 10^5 q^2)^s \right]^{1/s}. \quad (6.8)$$

Figure 6.8 (b) shows that the asymptote matching technique does not, in the case of

the two-dimensional prismatic bundles, approximate the transitional flow regime. The asymptote matching technique does on the other hand attempt to approximate a single equation with satisfactory results in both the Darcy and Forchheimer regimes. In this process it worsens the results in the Forchheimer regime. The reason for this behaviour is that the laminar Forchheimer regime does not exist at large enough Reynolds numbers to form a definite asymptote for the matching technique. In other words, the influence of the Darcy equation is still of a considerable magnitude at the end of the laminar Forchheimer regime.

Although the results obtained from the asymptote matching technique in this manner give satisfactory results to some extent, it is preferable to use different equations in the different flow regimes. This would give more accurate results, but the comfort of having only one equation for the whole flow regime has to be sacrificed.

6.6 A modelling recommendation

This section concludes which of the modelling assumptions discussed in this chapter serve as good approximations. A new modelling procedure for intermediate Reynolds number flow through staggered prismatic bundles is also presented.

In section 6.1 it was shown that the assumption of neglecting the friction drag on the solid material in the macroscopic momentum equation for intermediate Reynolds number flow is a good approximation. The analysis of the pressure distributions on the fluid-solid interfaces, presented in section 6.2, showed that the pressures on the downstream face may be sufficiently modelled as evenly distributed and equal to the maximum value. For the upstream side of the solid, it was shown that the assumption of evenly distributed pressure to be equal to the maximum value is a poor modelling assumption. Also in section 6.2, it was shown that the pressure at the downstream face may be adequately modelled as evenly distributed and equal to the pressure at the inflection point. Section 6.3 revealed that the Bernoulli equation could not be used on the dividing streamline, because of energy losses due to viscous dissipation. In section 6.4 it was shown that velocity magnitude at the inflection point may not be expressed as a factor β of the average interstitial stream-wise velocity, where β is the geometric transverse to stream-wise proportionality coefficient. Section 6.5 gave a discussion on the use of the asymptote matching technique. The asymptote matching technique may be used with a relatively

CHAPTER 6. VERIFICATION OF MODELLING ASSUMPTIONS

small loss of precision to obtain a unified expression that holds for the whole laminar flow regime.

The following modelling procedure attempts to improve the model for intermediate Reynolds number flow by using the Bernoulli equation in the sections of the interstitial flow channels where there are minimum viscous dissipation. Figure 6.9 shows the top halves of two adjacent RRUC's. A third RRUC may be visualised in the center as illustrated by RRUC II in the figure. The dots in Figure 6.9 represent the positions of the pressure values that will be used in the Bernoulli equation. The values of the different pressures are denoted by p_a , p_b , p_c , p_d and p_e respectively.

The Bernoulli equation may be applied to the streamline connecting b and c to yield

$$\frac{\rho}{2}w_{\parallel}^2 + p_b = p_c \quad (6.9)$$

and

$$p_c - p_b = \frac{\rho}{2}w_{\parallel}^2. \quad (6.10)$$

Applying the Bernoulli equation to the streamline that connects a and c results in

$$p_a + \frac{\rho}{2}w_{\parallel}^2 = p_c, \quad (6.11)$$

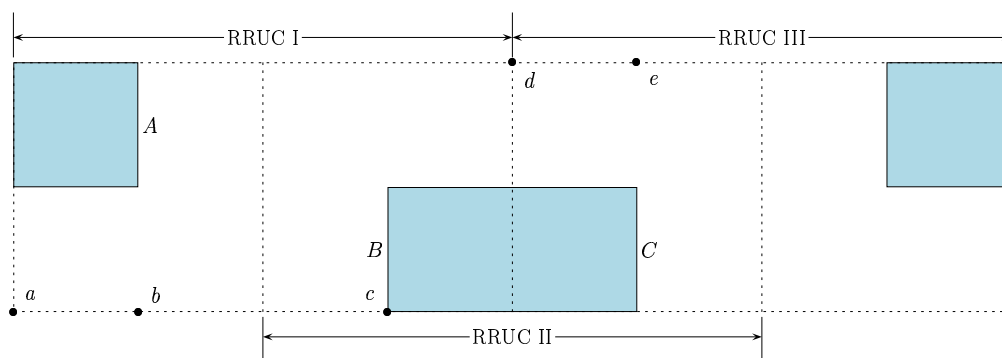


Figure 6.9: A schematic diagram of the locations of the pressures used for the modelling of intermediate Reynolds number flow in a staggered configuration.

CHAPTER 6. VERIFICATION OF MODELLING ASSUMPTIONS

and the Bernoulli equation applied to the streamline connecting d and e gives

$$p_d + \frac{\rho}{2} w_{\parallel}^2 = p_e + \frac{\rho}{2} w_{\parallel}^2 \quad (6.12)$$

so that

$$p_d = p_e. \quad (6.13)$$

Subtracting (6.13) from (6.11) results in

$$\begin{aligned} (p_a - p_d) + \frac{\rho}{2} w_{\parallel}^2 &= p_c - p_e \\ p_c - p_e &= \Delta P_f + \frac{\rho}{2} w_{\parallel}^2. \end{aligned} \quad (6.14)$$

Here ΔP_f is the macroscopic pressure drop over a unit cell. It is assumed that the pressure is constant over the cross section at point a and d and equal to the respective pressures, p_a and p_d . The macroscopic pressure drop is the same over RRUC I and RRUC II, as observed in section 5.5. If it is assumed that the skin drag is of negligible magnitude, the macroscopic momentum equation may be written as

$$-\epsilon U_0 \nabla P_f = \iint_{S_{\perp}} \underline{n} p dS. \quad (6.15)$$

If the integral on the right hand side of (6.15) is weighed according to the relative frequency of occurrence of the RRUC's of type I and II, then

$$-\epsilon U_0 \frac{\Delta P_f}{d} \hat{n} = \frac{d_s}{d} \iint_{S_{\perp}^I} \underline{n} p dS + \frac{(d - d_s)}{d} \iint_{S_{\perp}^{II}} \underline{n} p dS, \quad (6.16)$$

where S_{\perp}^I denotes the perpendicular surfaces of RRUC I and S_{\perp}^{II} denotes the perpendicular surfaces of RRUC II.

CHAPTER 6. VERIFICATION OF MODELLING ASSUMPTIONS

It may be assumed that the average pressure on the face marked as S_{\perp}^A in Figure 6.9 is equal to p_b and the average pressure on face S_{\perp}^B is equal to p_c . In the same manner the average pressure on face S_{\perp}^C is assumed to be equal to p_e . Equation (6.16) may now be written as

$$-\epsilon U_0 \frac{\Delta P_f}{d} = \frac{d_s}{d} (p_c S_{\perp}^B - p_b S_{\perp}^A) + \frac{(d - d_s)}{d} (p_c S_{\perp}^B - p_e S_{\perp}^C) \quad (6.17)$$

in the stream-wise direction. Substitution of (6.10) and (6.14) into (6.17) and noting that $S_{\perp}^A = S_{\perp}^B = S_{\perp}^C = d_s$, from the homogeneity requirement, yields

$$\begin{aligned} -\epsilon U_0 \frac{\Delta P_f}{d} &= \frac{d_s}{d} \frac{\rho}{2} w_{\parallel}^2 d_s + \frac{(d - d_s)}{d} \left(\Delta P_f + \frac{\rho}{2} w_{\parallel}^2 \right) d_s \\ &= \frac{(d - d_s)}{d} \Delta P_f d_s + \frac{\rho}{2} w_{\parallel}^2 d_s. \end{aligned} \quad (6.18)$$

Re-arrangement of the terms in (6.18) and setting $\frac{\Delta P_f}{d} = \frac{dP_f}{dx}$ yields

$$-\frac{dP_f}{dx} = \frac{\rho w_{\parallel}^2 d_s}{\epsilon U_0 + (d - d_s) d_s}. \quad (6.19)$$

Equation (6.19) may be incorporated into the general momentum transport equation to yield

$$-\epsilon \nabla P_f = G \mu q, \quad (6.20)$$

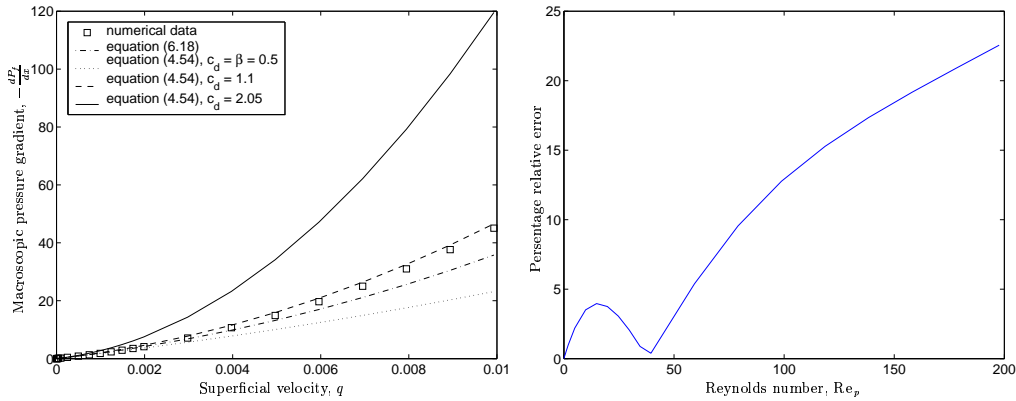
with

$$G = G_0 + G_{\infty}, \quad (6.21)$$

where

$$G_0 = \frac{12(1 + \frac{\beta}{2})\epsilon\sqrt{1 - \epsilon}}{d^2(1 - \sqrt{1 - \epsilon})^3} \quad (6.22)$$

CHAPTER 6. VERIFICATION OF MODELLING ASSUMPTIONS



(a) Superficial velocity versus the macroscopic pressure gradient of different models.

(b) The percentage error between the proposed model and the numerical solution plotted against the Reynolds number for a porosity of 0.6636.

Figure 6.10: A comparison between the proposed model and the models discussed in section 4.5.

and

$$G_\infty = \frac{\rho(1 + \sqrt{1 - \epsilon})q}{d\mu\sqrt{1 - \epsilon}(1 + 2\sqrt{1 - \epsilon})}. \quad (6.23)$$

An advantage of (6.20) is that there are no parameters that need to be determined experimentally. The equation is only dependent on the geometrical parameters of the porous medium.

Figure 6.10 (a) shows a plot of the superficial velocity against the macroscopic pressure gradient for different models, as well as the numerical data for a staggered configuration of a porosity of 0.6636. The model where a drag coefficient of $c_d = 2.05$ was used differs substantially from the numerical data. This could be expected since this value for the drag coefficient is for a rectangular prism without taking into account that it is part of a porous environment. The model where a drag coefficient of $c_d = 1.1$ was used, on the other hand, performs well against the numerical data. Here the drag coefficient were obtained by considering that it is part of a porous environment. The discussions in section 6.4 justifies the deviation from the numerical data where a velocity ratio, $\beta = 0.5$ was used in the modelling assumptions. The proposed model correlates relatively well with the other

CHAPTER 6. VERIFICATION OF MODELLING ASSUMPTIONS

models and the numerical data.

Figure 6.10 (b) shows a plot of the absolute percentage error made by this modelling attempt versus the Reynolds number for a staggered configuration with a porosity of 0.6636. The graph is obtained by calculating the absolute percentage error as follows

$$M^{error} = \left| \frac{\left(\frac{dP_f}{dx}\right)_{num} - \left(\frac{dP_f}{dx}\right)_{model}}{\left(\frac{dP_f}{dx}\right)_{num}} \right| \times 100, \quad (6.24)$$

where M^{error} is the absolute relative percentage error made, $\left(\frac{dP_f}{dx}\right)_{num}$ is the pressure drop obtained from the numerical simulation and $\left(\frac{dP_f}{dx}\right)_{model}$ is the pressure drop obtained from the model. The model pressure drop used for the purpose of computing the error was obtained by asymptotically matching the equation for the Forchheimer regime (6.19) with the numerically obtained Darcy regime equation. This procedure made it possible to test the assumptions on the Forchheimer model alone.

The error made at higher Reynolds numbers is still relatively large. This is due to the fact that only the use of the Bernoulli equation was improved. The poor modelling assumption that the pressure is evenly distributed and equal to the maximum value on the upstream face of the solid was again used in this approach. This reason for using this assumption is to be able to split the surface integrals in the manner used in (6.17). This is the only poor modelling assumption made in this modelling procedure and therefore it is the main reason for the relatively large errors at higher Reynolds numbers. This may be verified by observing that Figure 6.10 (b) correlates with Figure 6.4.

Chapter 7

Conclusions

One of the objectives of this study was to conduct a literature study concerning the theory of porous media modelling in general. An overview of some porous media modelling parameters for the modelling of various porous materials was presented. The volume averaging theory was presented and applied to the transport equations to obtain macroscopic balance equations. The macroscopic mechanical energy equation was also derived. A pore-scale model, based on a representative unit cell, was researched and applied to close the open macroscopic equations for a porous medium that consists of prismatic bundles.

A literature study was performed on the various flow regimes in porous media. Specific interest was paid to the onset of the laminar Forchheimer flow regime. Numerical simulations were performed on unit cells with a commercial numerical computational fluid dynamics (CFD) code, FLUENT. Observations and conclusions were made from the solutions of these simulations for different Reynolds numbers and porous media of different porosities. The results obtained were verified against recent published work in the field of intermediate Reynolds number flow through porous media. By analysing the two-dimensional flow patterns, it was found that there are three laminar flow regimes in fluid flow through porous media: the Darcy regime; a transitional flow regime; and the Forchheimer regime. It was also found that the inertial effects lead to impinging and the formation of eddies with sizes that depend on the Reynolds number. The presence of these eddies reduces the flow-section and increases the total viscous dissipation.

The results from the numerical simulations were also used to verify assumptions made in the RRUC pore-scale modelling procedure, with specific attention to the intermediate Reynolds number regime. It was found that assuming a constant pressure distribution

equal to the maximum pressure produces poor results, due to the impinging nature of the flow at intermediate Reynolds numbers. The use of the Bernoulli equation on a dividing streamline was also found to produce poor results. This was due to the high rate of viscous dissipation on the upstream side and corner of the solid. It was also shown that the velocity at the inflection point were not computed correctly with the use of a geometrical coefficient, β . The rest of the modelling assumptions were shown to be good approximations.

An attempt to improve the model for high Reynolds number flow was presented. The new model also uses the Bernoulli equation, but only in regions with little or vanishing viscous dissipation. The geometrical coefficient, β , is also not used in the modelling procedure. Thus, two of the three poor modelling assumptions were avoided. Unfortunately the use of the assumption of the upstream solid face was unavoidable, and this caused the new modelling procedure to be more or less as accurate as that assumption. A positive property of the proposed model is that it is entirely dependent on the geometrical features of the porous medium.

Appendix A

Derivation of the averaging identities

By applying the phase average definition (3.3) to the left hand side of (3.5), the derivation follows naturally

$$\begin{aligned}
 \langle \psi + \lambda \rangle &= \frac{1}{\mathcal{U}_0} \iiint_{\mathcal{U}_f} (\psi + \lambda) d\mathcal{U} \\
 &= \frac{1}{\mathcal{U}_0} \iiint_{\mathcal{U}_f} \psi d\mathcal{U} + \frac{1}{\mathcal{U}_s} \iiint_{\mathcal{U}_f} \lambda d\mathcal{U} \\
 &= \langle \psi \rangle + \langle \lambda \rangle.
 \end{aligned} \tag{A.1}$$

■

A similar trivial argument may be applied to (3.6) in the following manner

$$\begin{aligned}
 \langle \alpha \psi \rangle &= \frac{1}{\mathcal{U}_0} \iiint_{\mathcal{U}_f} \alpha \psi d\mathcal{U} \\
 &= \frac{\alpha}{\mathcal{U}_0} \iiint_{\mathcal{U}_f} \psi d\mathcal{U} \\
 &= \alpha \langle \psi \rangle.
 \end{aligned} \tag{A.2}$$

■

 APPENDIX A. DERIVATION OF THE AVERAGING IDENTITIES

The first part of (3.7) may be shown to be

$$\begin{aligned}
 \langle \{\psi\} \rangle &= \frac{1}{\mathcal{U}_0} \iiint_{\mathcal{U}_f} (\psi - \langle \psi \rangle_f) d\mathcal{U} \\
 &= \frac{1}{\mathcal{U}_0} \iiint_{\mathcal{U}_f} \psi d\mathcal{U} - \frac{\langle \psi \rangle_f}{\mathcal{U}_0} \iiint_{\mathcal{U}_f} d\mathcal{U} \\
 &= \langle \psi \rangle - \epsilon \langle \psi \rangle_f = 0,
 \end{aligned}$$

keeping in mind that $\langle \psi \rangle_f$ is an average over the fluid phase in an REV, and thus can be extracted from the integral. In a similar manner the second part of (3.7) follows to be

$$\begin{aligned}
 \{\langle \psi \rangle\} &= \langle \psi \rangle - \langle \langle \psi \rangle \rangle_f \\
 &= \langle \psi \rangle - \frac{\langle \psi \rangle}{\mathcal{U}_f} \iiint_{\mathcal{U}_f} d\mathcal{U} \\
 &= \langle \psi \rangle - \langle \psi \rangle = 0.
 \end{aligned} \tag{A.3}$$

■

Averaging identity (3.8) may easily be shown by using (3.7) in the following way

$$\begin{aligned}
 \{\{\psi\}\} &= \{\psi\} - \langle \{\psi\} \rangle_f \\
 &= \{\psi\} - \langle \{\psi\} \rangle / \epsilon \\
 &= \{\psi\}.
 \end{aligned} \tag{A.4}$$

■

It is easy to show (3.9) to be

$$\begin{aligned}
 \langle \langle \psi \rangle \rangle &= \langle \psi \rangle \langle 1 \rangle \\
 &= \epsilon \langle \psi \rangle.
 \end{aligned} \tag{A.5}$$

■

Making use of (3.7), averaging identity (3.10) yields

$$\begin{aligned}\langle\{\psi\}\langle\lambda\rangle\rangle &= \langle\lambda\rangle\langle\{\psi\}\rangle \\ &= 0\end{aligned}$$

and

$$\begin{aligned}\langle\langle\psi\rangle\{\lambda\}\rangle &= \langle\psi\rangle\langle\{\lambda\}\rangle \\ &= 0.\end{aligned}\tag{A.6}$$

The definition of the deviation as well as (3.5) and (3.7) may be used to justify (3.11) in the following manner

$$\begin{aligned}\langle\{\psi\}\{\lambda\}\rangle &= \langle\psi\{\lambda\} - \langle\psi\rangle_f\{\lambda\}\rangle \\ &= \langle\psi\{\lambda\}\rangle - \langle\psi\rangle_f\langle\{\lambda\}\rangle \\ &= \langle\psi\{\lambda\}\rangle\end{aligned}$$

and likewise

$$\langle\{\psi\}\{\lambda\}\rangle = \langle\{\psi\}\lambda\rangle.\tag{A.7}$$

■

Again, by using the definition of deviation along with (3.5) and (3.7), we may show (3.12) to be

$$\begin{aligned}\langle\psi\lambda\rangle &= \langle(\{\psi\} + \langle\psi\rangle_f)(\{\lambda\} + \langle\lambda\rangle_f)\rangle \\ &= \langle\langle\psi\rangle_f\langle\lambda\rangle_f\rangle + \langle\langle\psi\rangle_f\{\lambda\}\rangle + \langle\{\psi\}\langle\lambda\rangle_f\rangle + \langle\{\psi\}\{\lambda\}\rangle \\ &= \frac{\langle\psi\rangle\langle\lambda\rangle}{\epsilon\epsilon}\langle 1\rangle + \langle\psi\rangle_f\langle\{\lambda\}\rangle + \langle\lambda\rangle_f\langle\{\psi\}\rangle + \langle\{\psi\}\{\lambda\}\rangle \\ &= \langle\psi\rangle\langle\lambda\rangle/\epsilon + \langle\{\psi\}\{\lambda\}\rangle.\end{aligned}\tag{A.8}$$

■

By applying the definition of the deviation to the argument of the deviation on the left hand side of (3.13) we obtain

$$\begin{aligned}\{\psi\lambda\} &= \left\{ \left(\{\psi\} + \langle\psi\rangle_f \right) \left(\{\lambda\} + \langle\lambda\rangle_f \right) \right\} \\ &= \left\{ \{\psi\} \{\lambda\} \right\} + \left\{ \langle\psi\rangle_f \{\lambda\} \right\} + \left\{ \{\psi\} \langle\lambda\rangle_f \right\} + \left\{ \langle\psi\rangle_f \langle\lambda\rangle_f \right\}\end{aligned}$$

Each term on the right hand side of the equation above may be expanded by means of the definition of the deviation to yield

$$\begin{aligned}\{\psi\lambda\} &= \{\psi\} \{\lambda\} - \langle\{\psi\} \{\lambda\}\rangle_f + \langle\psi\rangle_f \{\lambda\} - \langle\langle\psi\rangle_f \{\lambda\}\rangle_f + \\ &\quad \{\psi\} \langle\lambda\rangle_f - \langle\langle\lambda\rangle_f \{\psi\}\rangle_f + \langle\psi\rangle_f \langle\lambda\rangle_f - \langle\langle\psi\rangle_f \langle\lambda\rangle_f\rangle_f.\end{aligned}$$

According to (3.7), the fourth and sixth terms on the right hand side of the above equation reduce to zero, while the last two terms cancel to yield

$$\{\psi\lambda\} = \{\psi\} \langle\lambda\rangle_f + \langle\psi\rangle_f \{\lambda\} + \{\psi\} \{\lambda\} - \langle\{\psi\} \{\lambda\}\rangle_f. \tag{A.9}$$

■

Appendix B

Slattery's averaging theorem

The spatial averaging theorem allows one to express the average of the gradient of any tensorial quantity in terms of the gradient of the average of the quantity under consideration. The spatial averaging theorem was presented independently in 1967 by Anderson and Jackson (1967), Slattery (1967) and Whitaker (1967). This resulted in three different proofs of the averaging theorem. As time progressed, other methods of proof for the averaging theorem were developed. The derivation presented here is a brief outline of the geometrical derivation presented by Whitaker (1985).

Consider two REV's of the same size, shape and orientation, as illustrated in Figure B.1. The second REV ($\mathcal{U}_0(\underline{x}_0 + \underline{dx}_0, t)$), with centroid at $\underline{x}_0 + \underline{dx}_0$, is translated a distance Δs from the first REV ($\mathcal{U}_0(\underline{x}_0, t)$), with centroid at \underline{x}_0 , along an arbitrary curve s , where they are investigated on the same instance of time. The displacement vector \underline{dx}_0 is tangent to the curve s , so that

$$\underline{dx}_0 = \underline{\lambda} ds,$$

with $\underline{\lambda}$ a unit vector tangent to s and in the direction of the translation.

Rather than to deal directly with the gradient of the arbitrary tensorial function $\psi = \psi(\underline{x}, t)$, integrated over the REV, it is more convenient to first use the directional derivative

in the following manner

$$\mathcal{I} = \underline{\lambda} \cdot \nabla \iiint_{\mathcal{U}_f(s,t)} \psi \, d\mathcal{U} \quad (\text{B.1})$$

$$= \frac{d}{ds} \iiint_{\mathcal{U}_f(s,t)} \psi \, d\mathcal{U}$$

$$= \lim_{\Delta s \rightarrow 0} \frac{1}{\Delta s} \left(\iiint_{\mathcal{U}_f(s+\Delta s,t)} \psi \, d\mathcal{U} - \iiint_{\mathcal{U}_f(s,t)} \psi \, d\mathcal{U} \right). \quad (\text{B.2})$$

The integrals over the overlapping fluid volumes, denoted by \mathcal{U}_{III} in Figure B.1, cancel to leave (B.2) as

$$\mathcal{I} = \lim_{\Delta s \rightarrow 0} \frac{1}{\Delta s} \left(\iiint_{\mathcal{U}_{\text{II}}(s+\Delta s,t)} \psi \, d\mathcal{U}_{\text{II}} - \iiint_{\mathcal{U}_{\text{I}}(s,t)} \psi \, d\mathcal{U}_{\text{I}} \right). \quad (\text{B.3})$$

The volume integrals may be expressed in terms of surface integrals, by making the following geometrical substitution of the volume increments, in terms of surface elements on \mathcal{S}_{ff} of the REV with centroid at \underline{r}_0

$$\begin{aligned} d\mathcal{U}_{\text{I}} &= -\underline{\lambda} \cdot \underline{n} \Delta s \, d\mathcal{S}_{\text{I}} \\ d\mathcal{U}_{\text{II}} &= \underline{\lambda} \cdot \underline{n} \Delta s \, d\mathcal{S}_{\text{II}}, \end{aligned}$$

With \underline{n} the outward normal of the fluid phase in the REV.

Extra volumes need to be considered due to the presence of solid material, causing the surface \mathcal{S}_{fs} not necessarily to be parallel to $\underline{\lambda}$. The magnitudes of these extra volumes are of $O(\psi l (\Delta s)^2)$, where l is the length of the contact line between the surface of the

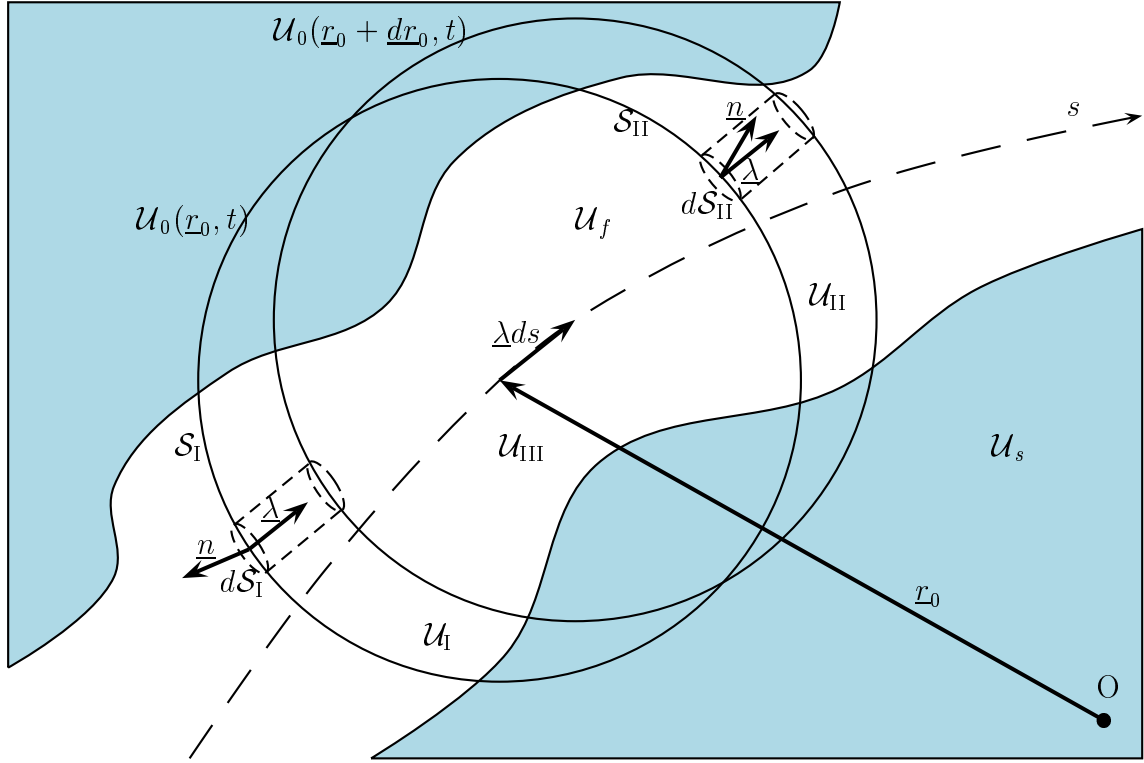


Figure B.1: Uniform translation of an REV along an arbitrary curve s .

averaging volume and \mathcal{S}_{fs} . This allows us to write (B.3) as

$$\mathcal{I} = \lim_{\Delta s \rightarrow 0} \frac{1}{\Delta s} \left(\iint_{\mathcal{S}_{II}} \underline{\lambda} \cdot \underline{n} \psi \Delta s \, d\mathcal{S}_{II} + \iint_{\mathcal{S}_I} \underline{\lambda} \cdot \underline{n} \psi \Delta s \, d\mathcal{S}_I + O(\psi l (\Delta s)^2) \right).$$

Since both Δs and $\underline{\lambda}$ are independent of position, they can be withdrawn from the integrals to yield

$$\mathcal{I} = \lim_{\Delta s \rightarrow 0} \left(\underline{\lambda} \cdot \iint_{\mathcal{S}_{II}} \underline{n} \psi \, d\mathcal{S}_{II} + \underline{\lambda} \cdot \iint_{\mathcal{S}_I} \underline{n} \psi \, d\mathcal{S}_I + \Delta s O(\psi l) \right).$$

The order of the error made by not considering the extra volumes vanish as $\Delta s \rightarrow 0$,

leaving

$$\mathcal{I} = \underline{\lambda} \cdot \iint_{\mathcal{S}_{ff}} \underline{n}\psi \, d\mathcal{S}. \quad (\text{B.4})$$

Keeping in mind that $\underline{\lambda}$ was chosen completely arbitrary and then comparing (B.4) with (B.1), the result of Slattery's averaging theorem is obtained

$$\nabla \iiint_{\mathcal{U}_f} \psi \, d\mathcal{U} = \iint_{\mathcal{S}_{ff}} \underline{n}\psi \, d\mathcal{S}. \quad (\text{B.5})$$

■

Appendix C

Derivation of the averaging theorem identities

Application of the divergence theorem to ψ in \mathcal{U}_f yields

$$\iiint_{\mathcal{U}_f} \nabla \psi \, d\mathcal{U} = \iint_{\partial \mathcal{U}_f} \underline{n} \psi \, d\mathcal{S} = \iint_{\mathcal{S}_{fs}} \underline{n} \psi \, d\mathcal{S} + \iint_{\mathcal{S}_{ff}} \underline{n} \psi \, d\mathcal{S}, \quad (\text{C.1})$$

where $\partial \mathcal{U}_f$ is the complete surface of \mathcal{U}_f . Substitution of (3.14) in (C.1) and division by the REV volume \mathcal{U}_0 , yields

$$\frac{1}{\mathcal{U}_0} \iiint_{\mathcal{U}_f} \nabla \psi \, d\mathcal{U} = \nabla \left(\frac{1}{\mathcal{U}_0} \iiint_{\mathcal{U}_f} \psi \, d\mathcal{U} \right) + \frac{1}{\mathcal{U}_0} \iint_{\mathcal{S}_{fs}} \underline{n} \psi \, d\mathcal{U}.$$

The equation above may be written in volume averaged form of an arbitrary tensor to obtain the desired result

$$\langle \nabla \psi \rangle = \nabla \langle \psi \rangle + \frac{1}{\mathcal{U}_0} \iint_{\mathcal{S}_{fs}} \underline{n} \psi \, d\mathcal{S}. \quad (\text{C.2})$$

■

Since (3.16) is valid for any tensorial quantity, contraction of the tensor yields the result of (3.17)

$$\langle \nabla \cdot \psi \rangle = \nabla \cdot \langle \psi \rangle + \frac{1}{\mathcal{U}_0} \iint_{\mathcal{S}_{fs}} \underline{n} \cdot \psi \, d\mathcal{S}. \quad (\text{C.3})$$

■

Substituting $\psi = 1$ into equation (3.16) we obtain

$$0 = \nabla \langle 1 \rangle + \frac{1}{\mathcal{U}_0} \iint_{\mathcal{S}_{fs}} \underline{n} \, d\mathcal{S}$$

and thereby identity (3.21)

$$\nabla \epsilon = -\frac{1}{\mathcal{U}_0} \iint_{\mathcal{S}_{fs}} \underline{n} \, d\mathcal{S}. \quad (\text{C.4})$$

■

The substitution of $\psi = 1$ into (C.1) delivers

$$0 = \iint_{\mathcal{S}_{fs}} \underline{n} \, d\mathcal{S} + \iint_{\mathcal{S}_{ff}} \underline{n} \, d\mathcal{S}. \quad (\text{C.5})$$

Equation (C.5) may now be used to conclude identity (3.22) as follows

$$\nabla \epsilon = \frac{1}{\mathcal{U}_0} \iint_{\mathcal{S}_{ff}} \underline{n} \, d\mathcal{S}. \quad (\text{C.6})$$

■

The substitution $\langle \psi \rangle = \epsilon \langle \psi \rangle_f$ on the right hand side of (3.16) leads to

$$\langle \nabla \psi \rangle = \nabla (\epsilon \langle \psi \rangle_f) + \frac{1}{\mathcal{U}_0} \iint_{\mathcal{S}_{fs}} \underline{n} \psi \, d\mathcal{S}. \quad (\text{C.7})$$

The product rule for differentiation shows the above equation to be

$$\langle \nabla \psi \rangle = \langle \psi \rangle_f \nabla \epsilon + \epsilon \nabla \langle \psi \rangle_f + \frac{1}{\mathcal{U}_0} \iint_{\mathcal{S}_{fs}} \underline{n} \psi \, d\mathcal{S}. \quad (\text{C.8})$$

The substitution of (3.21) into the above equation and the combination of the two surface integrals, along with the definition of the deviation yields

$$\begin{aligned} \langle \nabla \psi \rangle &= \epsilon \nabla \langle \psi \rangle_f + \frac{1}{\mathcal{U}_0} \iint_{\mathcal{S}_{fs}} \underline{n} (\psi - \langle \psi \rangle_f) \, d\mathcal{S} \\ &= \epsilon \nabla \langle \psi \rangle_f + \frac{1}{\mathcal{U}_0} \iint_{\mathcal{S}_{fs}} \underline{n} \{ \psi \} \, d\mathcal{S}. \end{aligned} \quad (\text{C.9})$$

■

Contraction of the arbitrary tensor ψ , may be used to justify identity (3.19)

$$\langle \nabla \cdot \psi \rangle = \epsilon \nabla \cdot \langle \psi \rangle_f + \frac{1}{\mathcal{U}_0} \iint_{\mathcal{S}_{fs}} \underline{n} \cdot \{ \psi \} \, d\mathcal{S}. \quad (\text{C.10})$$

■

Recall the averaging theorem of Slattery to be

$$\nabla \iiint_{\mathcal{U}_f} \psi \, d\mathcal{U} = \iint_{\mathcal{S}_{ff}} \underline{n} \psi \, d\mathcal{S}. \quad (\text{C.11})$$

The substitution of $\nabla\psi$ for ψ in (C.11), along with contraction thereof yields

$$\nabla \cdot \iiint_{\mathcal{U}_f} \nabla\psi \, d\mathcal{U} = \iint_{\mathcal{S}_{ff}} \underline{n} \cdot \nabla\psi \, d\mathcal{S}. \quad (\text{C.12})$$

Consider the following form of the divergence theorem

$$\begin{aligned} \iiint_{\mathcal{U}_f} \nabla\psi \, d\mathcal{U} &= \iint_{\partial\mathcal{U}_f} \underline{n} \psi \, d\mathcal{S} \\ &= \iint_{\mathcal{S}_{fs}} \underline{n} \psi \, d\mathcal{S} + \iint_{\mathcal{S}_{ff}} \underline{n} \psi \, d\mathcal{S}. \end{aligned} \quad (\text{C.13})$$

The substitution of $\nabla\psi$ for ψ in (C.13), along with contraction thereof will show to be handy

$$\begin{aligned} \iiint_{\mathcal{U}_f} \nabla \cdot \nabla\psi \, d\mathcal{U} &= \iint_{\partial\mathcal{U}_f} \underline{n} \cdot \nabla\psi \, d\mathcal{S} \\ &= \iint_{\mathcal{S}_{fs}} \underline{n} \cdot \nabla\psi \, d\mathcal{S} + \iint_{\mathcal{S}_{ff}} \underline{n} \cdot \nabla\psi \, d\mathcal{S}. \end{aligned} \quad (\text{C.14})$$

The substitution of (C.12) into (C.14) gives

$$\iiint_{\mathcal{U}_f} \nabla^2\psi \, d\mathcal{U} = \iint_{\mathcal{S}_{fs}} \underline{n} \cdot \nabla\psi \, d\mathcal{S} + \nabla \cdot \iiint_{\mathcal{U}_f} \nabla\psi \, d\mathcal{U}. \quad (\text{C.15})$$

By substituting (C.13) into (C.15) we obtain

$$\iiint_{\mathcal{U}_f} \nabla^2\psi \, d\mathcal{U} = \iint_{\mathcal{S}_{fs}} \underline{n} \cdot \nabla\psi \, d\mathcal{S} + \nabla \cdot \left(\iint_{\mathcal{S}_{fs}} \underline{n} \psi \, d\mathcal{S} + \iint_{\mathcal{S}_{ff}} \underline{n} \psi \, d\mathcal{S} \right). \quad (\text{C.16})$$

Now (C.11) may be used to write (C.16) as

$$\iiint_{\mathcal{U}_f} \nabla^2 \psi \, d\mathcal{U} = \iint_{\mathcal{S}_{fs}} \underline{n} \cdot \nabla \psi \, d\mathcal{S} + \nabla \cdot \left(\iint_{\mathcal{S}_{fs}} \underline{n} \psi \, d\mathcal{S} \right) + \nabla^2 \iiint_{\mathcal{U}_f} \psi \, d\mathcal{U}.$$

Division by the REV volume, which is constant in magnitude and form, leads to

$$\langle \nabla^2 \psi \rangle = \nabla^2 \langle \psi \rangle + \frac{1}{\mathcal{U}_0} \iint_{\mathcal{S}_{fs}} \underline{n} \cdot \nabla \psi \, d\mathcal{S} + \frac{1}{\mathcal{U}_0} \nabla \cdot \left(\iint_{\mathcal{S}_{fs}} \underline{n} \psi \, d\mathcal{S} \right). \quad (\text{C.17})$$

■

Identity (3.23) follows directly from Slattery's averaging theorem. Contraction of (3.14) and deviation by the REV volume yields

$$\nabla \cdot \left(\frac{1}{\mathcal{U}_0} \iiint_{\mathcal{U}_f} \psi \, d\mathcal{U} \right) = \frac{1}{\mathcal{U}_0} \iint_{\mathcal{S}_{ff}} \underline{n} \cdot \psi \, d\mathcal{S},$$

and thus

$$\nabla \cdot \langle \psi \rangle = \frac{1}{\mathcal{U}_0} \iint_{\mathcal{S}_{ff}} \underline{n} \cdot \psi \, d\mathcal{S}. \quad (\text{C.18})$$

■

Bibliography

- [1] ANDERSON, T.B. AND JACKSON, R., 1967, A fluid mechanical description of fluidized beds, *Ind. Engng. Chem. Fundamental*, **6**, pp. 527-538.
- [2] BARAK, A.Z., 1987, Comments on high 'High velocity flow in porous media' by Hassanizadeh and Gray, *Transport in porous media*, **2**, pp. 533-535.
- [3] BARRÈRE, J., 1990, *Modélisation des écoulements de Stokes at Navier-Stokes an milieu poreux*, Phd Thesis, Université de Bordeaux I.
- [4] BEAR, J., 1972, *Dynamics of fluids in porous media*, American Elsevier Publishing Company, Inc.
- [5] BEAR, J. AND BACHMAT, Y., 1991, *Introduction to modelling of transport phenomena in porous media*, Kluwer Academic Publishers, Dordrecht.
- [6] BEAR, J. AND BUCHLIN, J-M., 1991, *Modelling and applications of transport phenomena in porous media*, Kluwer Academic Publishers, Dordrecht.
- [7] BIRD, R.B., STEWART, W.E. AND LIGHTFOOT, E.N., 1960, *Transport Phenomena*, John Wiley, New York.
- [8] CARMAN, P.C., 1937, Fluid flow through granular beds, *Transactions of the Institution of Chemical Engineers*, **15**, pp. 150-166.
- [9] CHURCHILL, S.W. AND USAGI, R., 1972, A general expression for the correlation of rates of transfer and other phenomena, *American Institute of Chemical Engineering Journal*, **18**(6), pp. 1121-1128.
- [10] CLENNEL, M.B., 1997, *Tortuosity: A Guide through the maze*, Developments in petrophysics, eds. Lovell, M.A. and Harvey, P.K., Geological Society Special Publication No. **122**, pp. 299-344.

- [11] COMITI, J. AND RENAUD, M., 1989, A new model for determining mean structure parameters of fixed beds from pressure drop measurements: Application to beds packed with parallelepipedal particles, *Chemical Engineering Science*, **44**(7), pp. 1539-1545.
- [12] COMITI, J., SABIRI, N. E. AND MONTILLET, A., 2000, Experimental characterization of flow regimes in various porous media-III: Limit of Darcy's or creeping flow regime for Newtonian and purely viscous non-Newtonian fluids, *Chemical Engineering Science* **55**(15), pp. 3057-3061.
- [13] DIEDERICKS, G.P.J., 1992, *Tracer dispersion in porous media*, MSc Thesis, University of Stellenbosch, South Africa.
- [14] DIEDERICKS, G.P.J., 1999, *Pore scale modelling of transport phenomena in homogeneous porous media*, Phd Thesis, University of Stellenbosch, South Africa.
- [15] DULLIEN, F.A.L., 1979, *Porous media fluid transport and pore structures*, Academic Press, London
- [16] DU PLESSIS, J.P. AND MASLIYAH, J.H., 1988, Mathematical modelling of flow through consolidated isotropic porous media, *Transport in porous media*, **3**, pp. 145-161.
- [17] DU PLESSIS, J.P., 1991a, Saturated crossflow through a two-dimensional porous medium, *Advances in water resources*, **14** (3), pp. 131-137.
- [18] DU PLESSIS, J.P. AND MASLIYAH, J.H., 1991b, Flow through isotropic granular porous media, *Transport in Porous Media*, **6**, pp. 207-221.
- [19] DU PLESSIS, J.P. AND VAN DER WESTHUIZEN, J., 1993, Laminar crossflow through prismatic porous domains, *R&D Journal of the South African Institute of Mechanical Engineers*, **9**(2), pp. 18-24.
- [20] DU PLESSIS, J.P., 1994, Analytical quantification of coefficients in the Ergun equation for fluid friction in a packed bed, *Transport in Porous Media*, **16**, pp. 189-207.
- [21] DU PLESSIS, J.P. AND DIEDERICKS, G.P.J., 1997, *Pore-scale modelling of interstitial transport phenomena*, Chapter 2 of Fluid transport in porous media, editor J.P. du Plessis, vol 13, *Advances in Fluid Mechanics*, Series editor M. Rahman, Computational Mechanics Publications, Southampton, pp. 61-104.

- [22] FIRDAOUSS, M., GUERMOND, J.-L. AND LE QUÉRÉ, P., 1997, Nonlinear corrections to Darcy's law at low Reynolds numbers, *Journal of Fluid Mechanics*, **343**, pp. 331-350.
- [23] FIRDAOUSS, M. AND DU PLESSIS, J.P., 2004, On the prediction of Darcy permeability in nonisotropic periodic two-dimensional porous media, *Journal of Porous Media*, **2** (2), pp. 119-131.
- [24] FORCHHEIMER, P., 1901, Wasserbewegung durch boden, *Zeitung Ver. Deutsch. Ing.*, **45**, pp. 1782-1788.
- [25] FOURAR, M., , RADILLA, G., LENORMAND, R. AND MOYNE, C., 2004, On the non-linear behaviour of a laminar single phase flow through two and three-dimensional porous media, *Advances in Water Resources*, **27**, pp. 669-677.
- [26] HASSANIZADEH, S.M. AND GRAY, W.G., High velocity flow in porous media, *Transport in Porous Media*, **2**, pp. 521-531.
- [27] LLOYD, C.A., 2003, *Hydrodynamic permeability of staggered and non-staggered regular arrays of squares*, MSc Thesis, University of Stellenbosch, South Africa.
- [28] LLOYD, C.A., DU PLESSIS, J.P. AND HALVORSEN, B.M., 2004, On closure modelling of volume averaged equations for flow through two-dimensional arrays of squares, *Advances in fluid mechanics*, **40**, pp. 85-93.
- [29] MA, H., AND RUTH, D.W., 1993, The microscopic analysis of High Forchheimer number flow in porous media, *Transport in Porous Media*, **13**, pp. 139-160.
- [30] MEI, C.C. AND AURIAULT, J.-L., 1991, The effect of weak inertia on flow through a porous medium, *Journal of Fluid Mechanics*, **222**, pp. 647-663.
- [31] MUNSON, B.R., YOUNG, D.F. AND OKIISHI, T.H., *Fundamentals of Fluid Mechanics*, John Wiley & Sons, inc., New York, 1999.
- [32] PATANKAR S.V., *Numerical Heat Transfer and Fluid Flow*, Hemisphere Publishing Corp., Washington D.C., 1980.
- [33] ROJAS, S. AND KOPLIK, J., 1998, Nonlinear flow in porous media, *Physical Review E*, **58**(4), pp. 4776-4782.

- [34] RUTH, D. AND MA, H., 1992, On the derivation of the Forchheimer equation by means of the averaging theorem, *Transport in Porous Media* **7**(3), pp. 103-125.
- [35] SEGUIN, D., MONTILLET, A. AND COMITI, J., 1998a, Experimental characterization of flow regimes in various porous media-I: Limit of laminar flow regime, *Chemical Engineering Science* **53**(21), pp. 3751-3761.
- [36] SEGUIN, D., MONTILLET, A., COMITI, J. AND HUET, F., 1998b, Experimental characterization of flow regimes in various porous media-II: Transition to turbulent regime, *Chemical Engineering Science* **53**(22), pp. 3897-3909.
- [37] SKJETNE, E., HANSEN, A. AND GUDMUNDSSON, J.S., 1999a, High-velocity flow in a rough fracture, *Journal of Fluid Mechanics*, **383**, pp. 1-28.
- [38] SKJETNE, E. AND AURIAULT, J.L., 1999b, New insights on steady, non-linear flow in porous media, *European Journal of Mechanics-B/Fluids*, **18**(1), pp. 131-145.
- [39] SKJETNE, E. AND AURIAULT, J.L., 1999c, High-velocity laminar and turbulent flow in porous media, *Transport in porous media*, **36**, pp. 131-147.
- [40] SLATTERY, J.C., 1967, Flow of viscoelastic fluids through porous media, *AIChE Journal*, **13**(6), pp. 1066-1071.
- [41] SMITH, F., 1979, Laminar flow of an incompressible fluid past a bluff body: the separation, reattachment, eddy properties and drag, *Journal of Fluid Mechanics*, **92**, pp. 171-205.
- [42] TENG, H. AND ZHAO, T.S., 2000, An extension of Darcy's law to non-Stokes flow in porous media, *Chemical Engineering Science*, **55**, pp. 2727-2735.
- [43] TOKATY, G.A., 1971, *A History and philosophy of fluid mechanics*, G.T. Foulis and Company Ltd., Henley-on-Thames, Oxfordshire.
- [44] WHITAKER, S., 1967, Diffusion and dispersion in porous media, *AIChE Journal*, **13**(3), pp. 420-427.
- [45] WHITAKER, S., 1968, *Introduction to fluid mechanics*, Prentice-Hall, Inc., Englewood Cliffs, N.J.
- [46] WHITAKER, S., 1985, A simple geometrical derivation of the spatial averaging theorem, *Chemical Engineering Education*, **19**, pp. 18-21 and pp. 50-52.

- [47] WHITAKER, S., 1986, Flow in porous media I: a theoretical derivation of Darcy's law, *Transport in Porous Media*, **1**, pp. 3-25.
- [48] WODIE, J.-C. AND LEVY, T., 1991, Correction non linéaire de la loi de Darcy, *C.R. Acad. Sci. Paris Série II*, **312**, pp. 157-161.